EDGE STATE CHARACTERIZATION OF EPITAXIAL GRAPHENE NANORIBBONS AND MODIFICATIONS OF THE ELECTRICAL STRUCTURE OF BUFFER GRAPHENE AFTER ALUMINUM OXIDE DEPOSITION

A Dissertation
Presented to
The Academic Faculty

By

Anna Miettinen

In Partial Fulfillment
of the Requirements for the Degree
Doctor of Philosophy in the
School of Physics

Georgia Institute of Technology

May 2020

EDGE STATE CHARACTERIZATION OF EPITAXIAL GRAPHENE NANORIBBONS AND MODIFICATIONS OF THE ELECTRICAL STRUCTURE OF BUFFER GRAPHENE AFTER ALUMINUM OXIDE DEPOSITION

Approved by:

Dr. Edward Conrad, Advisor
College of Sciences
Georgia Institute of Technology

Dr. Phillip N. First
College of Sciences
Georgia Institute of Technology

Dr. Zhigang Jiang
College of Sciences
Georgia Institute of Technology

Dr. Markus Kindermann
College of Sciences
Georgia Institute of Technology

Dr. Antonio Tejeda
Laboratory of Solid State Physics
University of Paris-Sud

Date Approved: January 28, 2020

ACKNOWLEDGEMENTS

This work could not have been completed without the support from the community around me. Thank you to my cohort who walked beside me these long years. My friends in the Physics community have given my graduate experience meaning beyond the literature. I greatly benefited from discussions with Dr. Shane Jacobeen, Jeremy Yang, Lee Griffin and many others. My family have been understanding and provided endless encouragement to me through the difficult times I faced in research. In addition, they have kept me grounded and focused on the future.

When I began my research in the field of graphene, Dr. Meredith Nevius and Dr. Matthew Conrad patiently instructed me in foundational graphene research. I appreciate the time and dedication required to maintain and train users in the IEN facilities. I particularly owe my thanks to Chris Yang and Devin Brown for their extensive knowledge in MEMS processing and hours in the clean room. I've had the opportunity to be involved in several collaborations. Wonhee Ko and Dr. An-Ping Li were both essential resources for this research. At the Soleil Synchrotron, Dr. Antonio Tejeda dedicated many evenings to teaching me to take measurements and interpret ARPES signals. I'd like to extend my thanks to him for his effort and patience during my trips to France.

I'd like to thank my Thesis Committee, Dr. Zhigang Jiang, Dr. Phillip First, Dr. Antonio Tejeda and Dr. Markus Kindermann. Their guidance and discussion was essential to the completion of my thesis.

Finally, thank you to my advisor, Dr. Edward Conrad, for his patience and mentorship over the years. His vast knowledge has been a constant source of guidance forward during the time I spent in this lab.

TABLE OF CONTENTS

LIST OF TABLES

LIST OF FIGURES

SUMMARY

Graphene attracted a great deal of public interest because of its novel electrical characteristics, structural integrity, high electron mobility, and most important for my work, it was shown to be a room temperature ballistic transport material when it is grown on steps in SiC. There have, however, been inconsistencies between graphene research groups studying the electronic properties of zig-zag (ZZ) edge graphene ribbons. While ballistic transport measurements have been recorded at room temperature along ZZ-edge graphene nanoribbons using 4-probe scanning tunneling microscopy (STM) measurements,[1] direct band structure measurements, using angle resolved photoemission spectroscopy (ARPES) for ZZ-ribbons grown under the same conditions, find that conducting graphene does not grow on the sidewalls of SiC steps. In this thesis, I will show that these different results are not due to growth protocols but instead are due to the starting SiC polytype used as the graphene growth substrate. It has been typically assumed that the substrate SiC polytype is not a relevant factor in graphene growth on SiC. However, the stability of SiC steps, from which ZZ-edge ribbons grow, is very different as experimental and theoretical polar surface free-energy plots of different SiC polytypes show [2].

In this work, I have shown that the SiC polytype determines whether or not ZZ-edge graphene ribbons are strongly or weakly bonded to the SiC trench face. ZZ ribbons grown on 4H SiC are so strongly bonded to the substrate that there is no evidence of a linear Dirac cone unless the graphene-substrate bonds are broken using H-intercalation. In contrast, ZZ-edge graphene ribbons grown on 6H SiC reliably show a modified Dirac cone with a pair of edge states. 2-point transport measurements show that only the 6H sidewall ribbons are ballistic conductors.

In addition to my ribbon studies, I have also looked at the effects of a gate oxide grown on the semiconducting buffer graphene layer on SiC(0001). It is generally understood that gate oxides do not strongly interact with the metallic graphene layer that grows above

the buffer graphene layer on SiC [3]. While this is true for few-layer graphene isolated from the buffer and substrate, the buffer graphene layer is highly reactive. The complex carbon-substrate bonding structure of this layer opens a band gap. I will demonstrate, using core-level and valence-level ARPES, that the buffer graphenes electronic structure changes after a thin aluminum oxide is deposited. I show that parts of the buffer layer delaminates from the SIC making it metallic rather than semiconducting.

CHAPTER 1

GRAPHENE STRUCTURE AND THEORETICAL ELECTRICAL PROPERTIES

Graphene ribbons grown on the sidewall of steps on silicon carbide have been studied as a means of potentially producing a new graphene electronic platform. There are two primary orientations of graphene nanoribbons (GNR), the zigzag (ZZ)-edge and the arm-chair (AC)-edge. The electronic properties of GNR are significantly different depending on edge choice [4, 5, 6, 7]. In 2014, ballistic transport measurements have been recorded at room temperature for ZZ-oriented graphene nanoribbons on 6H-SiC using 4-probe STM measurements [1]. However, attempts to measure the band structure of similarly grown graphene ribbons on 4H-SiC using angle resolved photoemission (ARPES), have not had any success[8].

In this thesis, I will show that these discrepancies are due to the polytype choice of the SiC substrate used to grow these ribbons. The work presented in this thesis will show that only ZZ-edge GNR grown on 6H-SiC sidewalls produce observable band structures in ARPES. ZZ-edge ribbons grown on 6H-SiC have a gapped band structure with two localized surface states near the Fermi level. In contrast, ribbons grown on 4H-SiC have severely distorted π-bands because of strong interactions with the 4H-SiC facet wall. While 2-point transport measurements of 6H-ZZ samples demonstrate ballistic conduction, 4H-ZZ ribbons are diffusive conductors. The polytype of SiC dramatically changes the bonding structure of graphene to the SiC sidewall facet. In this chapter I briefly review the physical and electronic structure of graphene and the theoretical electronic properties of ZZ-edge and AC-edge GNR.

1.1 Physical Structure

Graphene is a carbon sheet that is only a single atom thick. The atoms are arranged in a honeycomb lattice with a basic cell of 2 carbon atoms, shown in a orange diamond in Fig. 1.1. The two atoms form identical sublattices. The carbon atoms are strongly bonded laterally with hybridized sp^2 orbitals to its three nearest neighbors called σ bonds. These bonds are responsible for the stability of the 2 dimensional crystal structure of freestanding graphene. The remaining electron is associated with a out-of-plane p_z orbital. This free electron is responsible for the high electronic mobility and does not strongly interact with adjacent carbon sheets [6]. The strong bonding between adjacent carbon atoms and relatively weak interaction between layered sheets means that a graphene sheet is essentially a two-dimensional material.

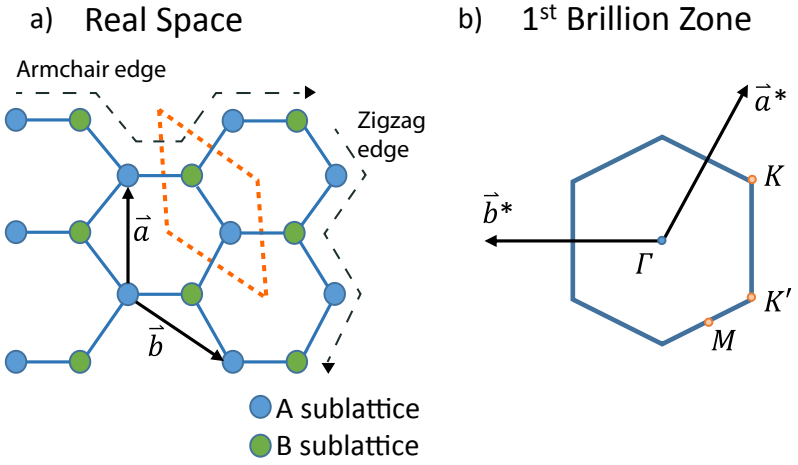

Figure 1.1: a) Real space hexagonal lattice of carbon atoms, comprised of A and B sublattices. Lattice vectors $\vec{a}$ and $\vec{b}$ have magnitude 2.46 Å and are 120° apart. The base periodic cell is outlined in the orange dotted diamond. The two common edge configurations, the armchair and zigzag edges, are labeled and further discussed in section 1.3. b) 1^{st} Brillioun zone in reciprocal space, Γ, K, K' and M points are labeled as well as the reciprocal lattice vectors, $\vec{a^*}$ and $\vec{b^*}$.

The basic honeycomb graphene structure and its first Brillouin zone (BZ) are shown in Fig. 1.1. The real-space cell and first BZ are the minimum-volume periodic cells in real and reciprocal space, respectively. The 6 points of the BZ are the 3 pairs of K and K'

points, in the center of the BZ is the Γ point. Graphene lattice vectors, $\vec{a}$ and $\vec{b}$, are 120° apart with length $|a_g|$. To two significant figures, the lattice constant of graphene grown epitaxially on SiC is 2.46 Å. The reciprocal lattice vectors, $\vec{a^*}$ and $\vec{b^*}$, are have a magnitude $|a^*|$=$|b^*|$= 2.96 Å^{-1}. The distance between Γ and K is then 2.96 $\cos(30°)\frac{2}{3}$ = 1.71 Å^{-1} (see Fig. 1.1).

1.2 Electronic Structure and Transport

One reason for the popularity of graphene in materials science is the linear dispersion of the valence and conduction bands about the K and K' points. The conduction and valence bands make contact at these points, so graphene sheets are theoretically conductive. The graphene electronic structure calculated from a tight-binding (TB) approximation is shown in Fig. 1.2 (a). Due to the 2-dimensional character of graphene, the momentum vector, $\vec{k}$, is decomposed into two components, k_x and k_y, parallel to the graphene surface. The linear bands are produced by the p_z electron orbital and are called the graphene π-bands. The cone-shaped band structure is called a Dirac cone and is shown in Fig. 1.2(b). The π^-- and π^+- bands refer to the left and right sides of the cone, respectively. The point where the π-bands cross is called the Dirac point, located in binding energy at E_D. For neutrally doped graphene, the Dirac point occurs at the Fermi level, E_D = E_F.

Close to the Fermi level, the band structure is well described using a Dirac-like Hamiltonian, $H\Psi = -i\hbar v_F \sigma \nabla \Psi$, where σ are the Pauli spin matrices and v_F is called the Fermi velocity, the effective speed of massless charge carriers. This band structure was originally calculated using a nearest-neighbors formalism by Wallace in 1947 [9]. The linear dispersion has a slope of $\hbar v_F$, about $\hbar$c/300, or $\sim \hbar 10^6$ m/s^2 [9, 6]. Fig. 1.2 (b) shows the shape of the π-bands about the K-point, notice they are approximately linear at low binding energy.

Graphene attracted significant attention for its novel electrical properties, including exceptionally high mobility [10, 11, 6, 1, 12]. Measured mobilities have been recorded as

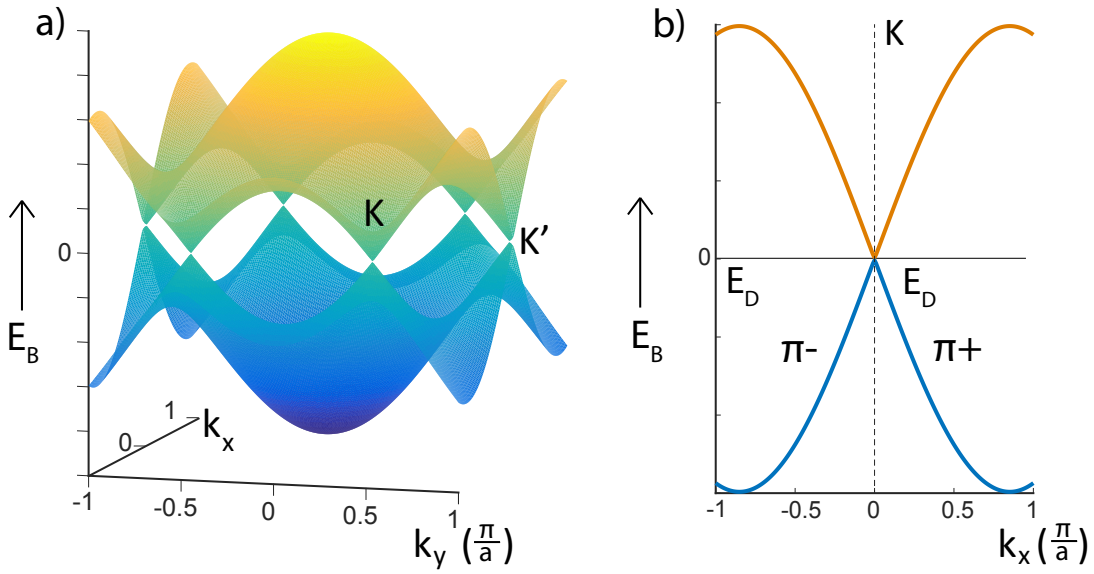

Figure 1.2: a) TB calculation of first BZ as described in [9]. One K and K' pair are labeled. b) Cross section taken across a K point for constant k_y. The Dirac point, E_D, and $\pi^{\pm}$-bands are labeled.

high as 200,000 cm^2/Vs on graphene flakes. The mobility is often reduced by limitations based on fabrication method and bonding defects [6, 11]. Even so, high mobilities at ambient temperatures motivate the experimental studies of graphene for high speed devices. It was also shown that single-layer graphene exhibits a half-integer quantum hall effect (QHE) [13, 14, 15, 16], demonstrating that mobile charge carriers act as a 2-dimensional electron gas (2DEG). Most significant to this thesis are the studies of ballistic transport from finite size effects in graphene ribbons (see section 1.3.3).

1.3 Graphene Nanoribbon Electronic Structure

Exploiting the distinct edge configurations in selected orientations of narrow GNR can open a band gap or cause unique energy states in the electronic structure of GNR. The two primary graphene edge configurations as shown in Fig. 1.1 (a) are called the zig-zag (ZZ) and armchair (AC) edges. The theoretical motivation for studying GNR is outlined below. The methods used to fabricate these ribbons is described in section 2.4.

1.3.1 Zig Zag Ribbons

ZZ-edge Ribbons: Tight Binding Approach

The most straightforward way to calculate the band structure for ZZ-edge GNR is to use a simple Dirac-Hamiltonian TB approximation with periodic boundary conditions. This eliminates all electron-electron and electron-phonon interactions, greatly simplifying the calculation. All dangling bonds are assumed to be hydrogen-terminated and are non-interacting. Given these constraints, the ZZ-edge band structure is shown in Fig. 1.3 (a) for a ribbon with thirty zigzag chains (N = 30). As the ribbon is narrowed further, the shape of the π-bands becomes asymmetric about the K point [4]. An example of a narrow ribbon (N = 5) is shown in Fig. 1.3 (b). The slope of the π^+-bands is greater than that of the π^--band.

What differentiates ZZ-edge ribbons from AC-edge ribbons is the existence of an edge state. When calculated from a TB model, ZZ-edge ribbons have a doubly degenerate energy state where the first conduction and valence bands meet at the graphene K-point [4]. These states are referred to as 'edge states' because their charge density is localized at the ZZ-edge of the ribbon, indicated with dark circles in Fig. 1.3 (c). These flat, degenerate bands run from the graphene K point to the M point, corresponding to a very sharp peak in the density of states. Beyond the edge states, the subsequent bands are called extended states because they are not localized in real space [17].

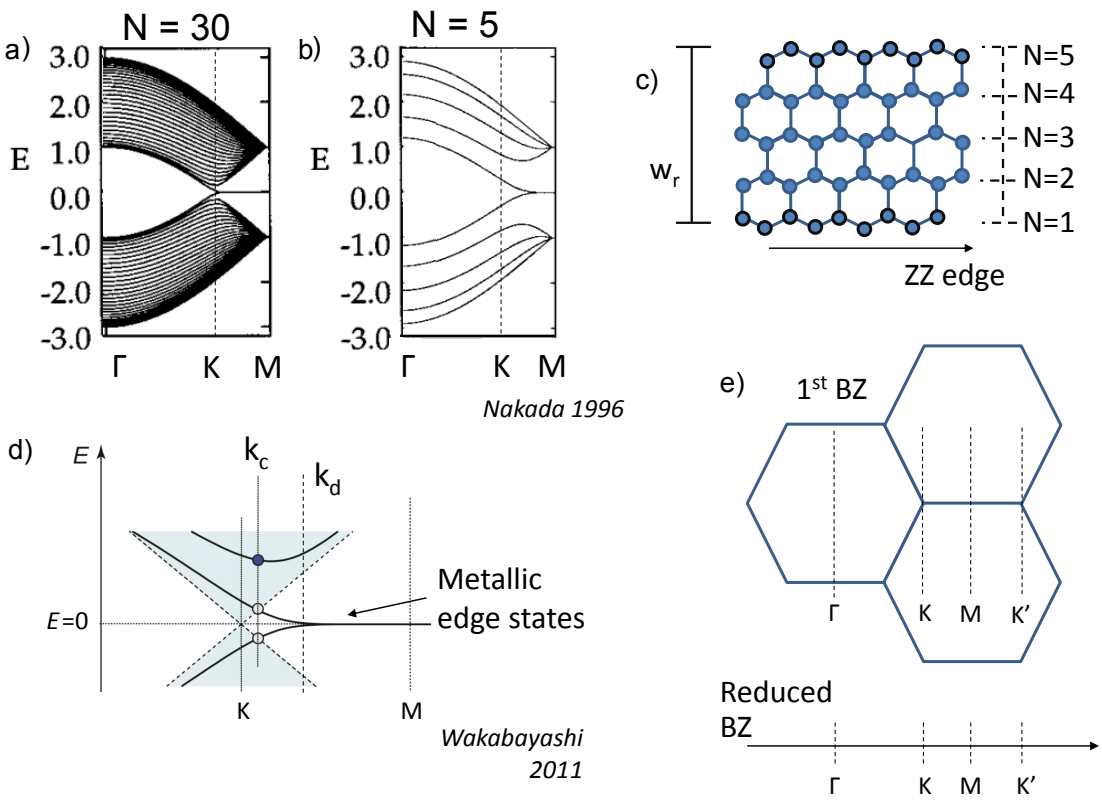

Figure 1.3: a) and b) TB calculations for Z ribbons with N=30 and N=5, respectively. K point shown at $2\pi/3$ with dashed line. Adapted from [4]. c) Real space horizontal graphene ribbon, ZZ edge indicated. Dark circles indicate the localized real-space origin of the ZZ edge states, w_R is the ribbon width, N indicates the number of ZZ chains across the ribbon. d) GW approximation effects from confinement geometry push point where the edge states make contact toward M from K. A dark blue circle marks the approximate location of the shifted conduction band minimum at k_c. The point where the edge states meet is marked k_d. Adapted from [7]. e) Brillioun zone, Γ, K and M points labeled. When geometrically constrained, the 1st Brillioun zone is reduced into one dimension as shown.

For narrow ribbons, the location where the edge states meet is shifted towards M from K, as shown in Fig. 1.3 (d). This is dependent on the width of the ribbon. The edge state

band shape can be calculated using the following equations:

$$\begin{aligned} E &= \pm\sqrt{1 + g_k^2 + 2g_k\cos(p)} \\ g_k &= 2\cos(k/2) \\ 0 &= \sin(Np) + g_k\sin((N+1)p) \end{aligned} \tag{1.1}$$

The edge state is determined by the first solution of p the last equation. The energy bands for the extended states are found from the solutions of p [17]. Solving equation 1.1 for E = 0 produces the location of the critical momentum where the edge states begin to become localized, k_c, defined as follows:

$$k_c = 2\arccos\big(\pm\frac{0.5}{1+1/N}\big) \tag{1.2}$$

where k_c is in units of π/a and N is the width of the ribbon in ZZ pairs (see Fig. 1.3) [17]. Note that k_c occurs at the graphene K point for wide ribbons (N>>1), but is pushed toward higher k if N is small. The maximum and minimum of the first conduction and valence bands respectively after the edge states occur roughly at k_c, indicated by a blue dot in Fig. 1.3 (d).

The energy spectrum has N extended state solutions from $0<k<k_c$ and no localized edge state solutions. From $k_c<k<$M, there are only N-1 extended state solutions plus one edge state [7]. This band structure is shown in Fig. 1.3 (d). The flat extended state exists in the BZ from k_d to M (as opposed to the traditional TB model, where it exists from K to M [4]). In these TB models the edge states meet at the Fermi level, suggesting that ZZ ribbons will always be metallic. A more complex model must be used to produce a bandgap as a result of finite size effects.

ZZ-edge Ribbons: Interactions and Asymmetric Boundaries

A TB approach alone does not result in the formation of a ZZ-edge bandgap in the graphene energy spectrum. Ab initio calculations for geometries that break the ZZ-edge chiral symmetry result in lifting the edge state degeneracy and form a bandgap. This can be modeled using defects in the ribbon structure or incorporating different boundary conditions [18, 19, 20].

For example, ZZ-edges have a magnetic moment in the ground state [21]. By accounting for spin polarization, it has been shown that a bandgap may exist through the entire BZ. ZZ-edges energetically prefer oppositely-oriented magnetic moments (antiferromagnetic) on the edges [22, 18]. The energy difference between antiferromagnetic edges lifts the edge state degeneracy, resulting in a bandgap in between the edge states (see Fig. 1.4) [18]. Using a local spin density approximation (LSDA), the bandgap is inversely related to ribbon width, W_r. The size of the gap is approximated by $\Delta^0_{LSDA} = 9.33/(W_r + 15)$ eV [23]. While the size of this bandgap is notably small, <0.4 eV, it shows that the edge states unique to ZZ-edge ribbons are not necessarily degenerate.

Building from this model, the many-body electron (GW) approximation accounts for electron-electron interactions within the ribbon as well as the polarized ZZ-edges. Similarly to the LSDA model, the energy gap is inversely related to ribbon width. Because the GW approximation does not have hard-wall boundary conditions, the effective width of the ribbon is a little larger than W_r. Instead, the gap is proportional to $1/(W_r + \xi_0)$. In the GW approximation, ξ_0 is approximately 16Å. The gap is described with

$$\begin{aligned} \Delta^0 &\propto \frac{1}{W_r + \xi_0} \\ \Delta^0_{GW} &\approx \frac{38}{W_r + 16} \end{aligned} \tag{1.3}$$

where ξ_0 is the added effective width to the ribbon in angstroms and 38 is a scalable variable in units of eVÅ^{-1}, fit to the calculated band structure in reference [5]. These edge states

never make contact in the Brillioun zone and the energy gap at the M point, Δ^1 in insensitive to ribbon width. The ab initio calculated band structure and size of the bandgap,Δ^0_{GW}, is shown in Fig. 1.4 (a) and (b).

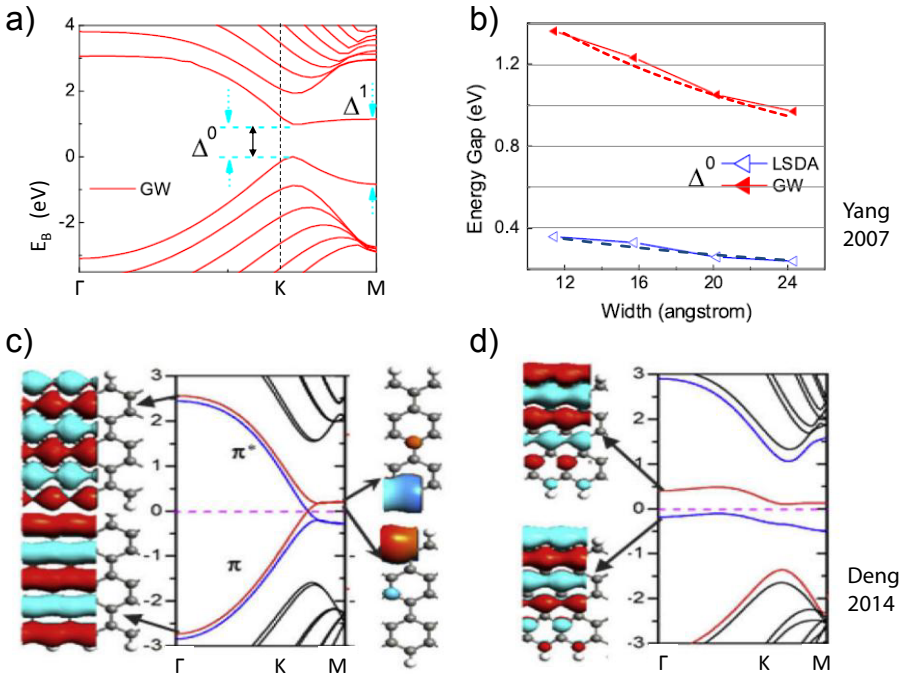

Figure 1.4: a) GW Approximation band structure for ZZ-edge GNR, N=12. Δ^0 indicates the width-dependent bandgap, Δ^1 indicates the nearly-constant gap at the edge of the BZ. b) Comparison of the size of Δ^0 using the GW approximation and the LSDA approximation. Dotted lines show fits with values used in this thesis and in [24]. Adapted from [5]. c) Band structure and wave function for symmetrically terminated, spin polarized ZZ GNR, N = 5. The extended state wavefunction is shown on the left, the edge state wavefunction is shown on the right. d) Asymmetrically terminated ZZ GNR, N=5. Ferromagnetic edges produce quasi-localized edge states spanning the entire BZ. Adapted from [20].

In the case of symmetric hydrogen-terminated edges (as in the LSDA and GW calculations) the localized edge states are only present from k_c to M. On the other hand, asymmetric edge terminations significantly alter the nature of the edge states. If one edge is H-terminated while the opposite edge is H_2-terminated, the edge state exists across the

entire BZ from Γ to K. The edge state is a nearly flat band across the entire BZ near the Fermi level [20]. A comparison between symmetrically terminated and asymmetrically terminated ZZ-edge calculations is shown in Fig. 1.4 (c) and (d). While calculations suggest the existence of edge states and estimate the characteristics of the ribbon energy spectrum, most techniques of ribbon production do not produce ideal ribbon edges. Localized deformations or bonding structures may significantly impact the characteristics of the GNR energy bands. Direct measurements of the band structure with angle-resolved photoemission spectroscopy (discussed in section 2.6.1) are the only way to absolutely determine the existence of an edge state.

1.3.2 Armchair Ribbons

TB calculations demonstrate that graphene AC edges have a width dependent band gap opening for sufficiently narrow ribbons. AC ribbons are capable of both metallic and gapped electronic character and are extremely sensitive to ribbon width. They have metallic characteristics if there are 3M-1 unit cells across the ribbon, where M = 1,2,3 ... (see Fig. 1.5) [4]. Furthermore, ab initio calculations show an energy band gap opens with the addition of an edge deformation for any narrow-width AC ribbon due to the ribbon's sensitivity to the extra dangling carbon bond along the edge [25]. Similarly, TB models predict the existence of an ZZ-like edge state for any AC edge with a ZZ-edge defect [26]. Direct measurement of AC-edge nanoribbons in ARPES have not yet demonstrated the predicted edge states, possibly due to edge bonding structures or because the TB approximation is too simple a model to accurately depict the many-body interaction of an AC-edge ribbon.

1.3.3 Ballistic Transport

Epitaxial GNR grown on 6H-SiC have been shown to be room temperature ballistic conductors on a micron-scale [1]. Ballistic transport is where the carrier's mean free path (MFP) is longer than the length of the transport channel. This causes resistance (R) to be

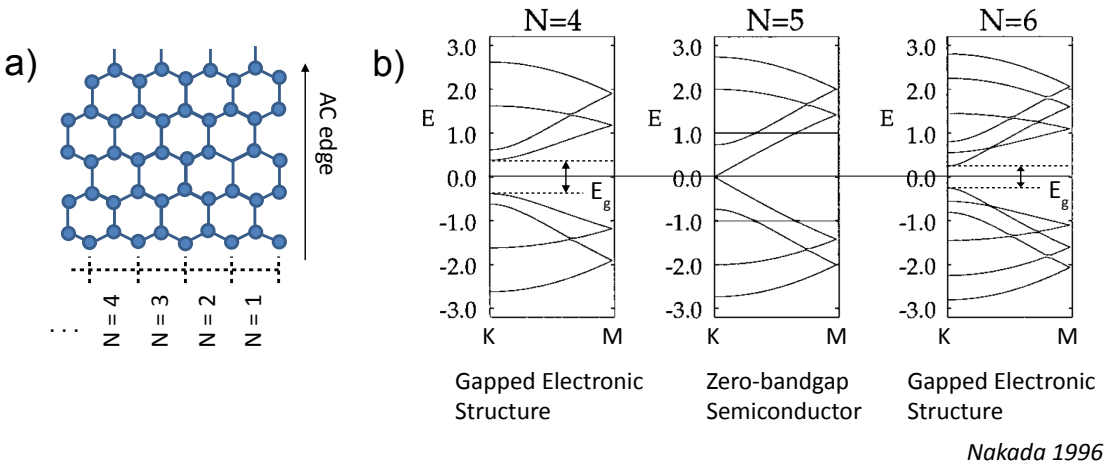

Figure 1.5: a) Real space graphene lattice, AC edge indicated and dimer lines indexed along the bottom. AC ribbons are shown to have energy gaps if they have length N $\neq$ 3M-1, where m = 1,2,3... Adapted from [4].

independent of channel length, contrary to standard ohmic transport where R $\propto l$. The conductance of such channels is quantized. The Landauer-Buttiker formalism to derive the quantized conductance, G_0, is shown below [27].

If the voltage source and drain are kept at a voltage of μ_1 and μ_2 respectively, then the current between them (I_{SD}) is given by:

$$\begin{aligned} I_{SD} &= \frac{g_s e}{h} \int_{\mu_1}^{\mu_2} M(E) f'(E) T(E) dE \\ I_{SD} &= \frac{g_s e^2}{\hbar} MT \end{aligned} \tag{1.4}$$

where g_s is the degeneracy of the mode, M is the number of modes above the cutoff at energy E, f(E) is the charge distribution function and T is the transmission function (set to unity for ballistic conducting channels). The quantum conductance, G_0, is calculated

according to the Landauer-Buttiker formalism:

$$\begin{aligned} V =& \frac{\mu_1 - \mu_2}{e} \\ G =& I/V = G_0 MT \\ G_0 =& \frac{g_s e^2}{\hbar} \end{aligned} \tag{1.5}$$

The conductance along GNR measured by 2- and 4-probe STM is e^2/h, the quantum conductance G_0 [1]. This indicates that the ballistic channel in these samples is only a single channel, or g_s = 1. It then follows that the theoretical lower limit of the resistance is equal to the inverse of G_0, $R_0 = h/e^2$. When a passive probe is introduced along a ballistic channel, it acts as a scattering center to the mobile charge carriers and doubles the resistance. This effect was confirmed using a probe along the ribbon, shown in Fig. 1.6(b). The ballistic transport was shown to persist up to at least 5 microns and be temperature independent up to at least 300 K [1].

The mechanism for this ballistic transport was attributed to metallic edge states near the Fermi level in narrow ZZ-edge ribbons [1]. This is consistent with the fact that edge states are not predicted for AC-edge ribbons and that ballistic transport has not been measured from AC-edge epitaxial GNR on either 4H- or 6H-SiC. This demonstrates that the edge type on these epitaxial ribbons is instrumental to observing ballistic transport on this type of ribbons (growth methods for GNR are discussed in section 2.4).

However, until now these edge states have not been directly observed using angle-resolved photoemission spectroscopy (ARPES) on ZZ-edge ribbons grown on 4H-SiC. It has been the assumption that the SiC polytype does not impact the epitaxial ribbon structure, but I have shown that these ZZ-edge states are observed in ARPES using a 6H-SiC substrate. Chapter 3 details the existing work in characterizing epitaxially grown GNR in both primary orientations on 4H-SiC. Chapter 4 describes the conditions under which sidewall ribbons produce localized edge states observable in ARPES and reproduce ballistic

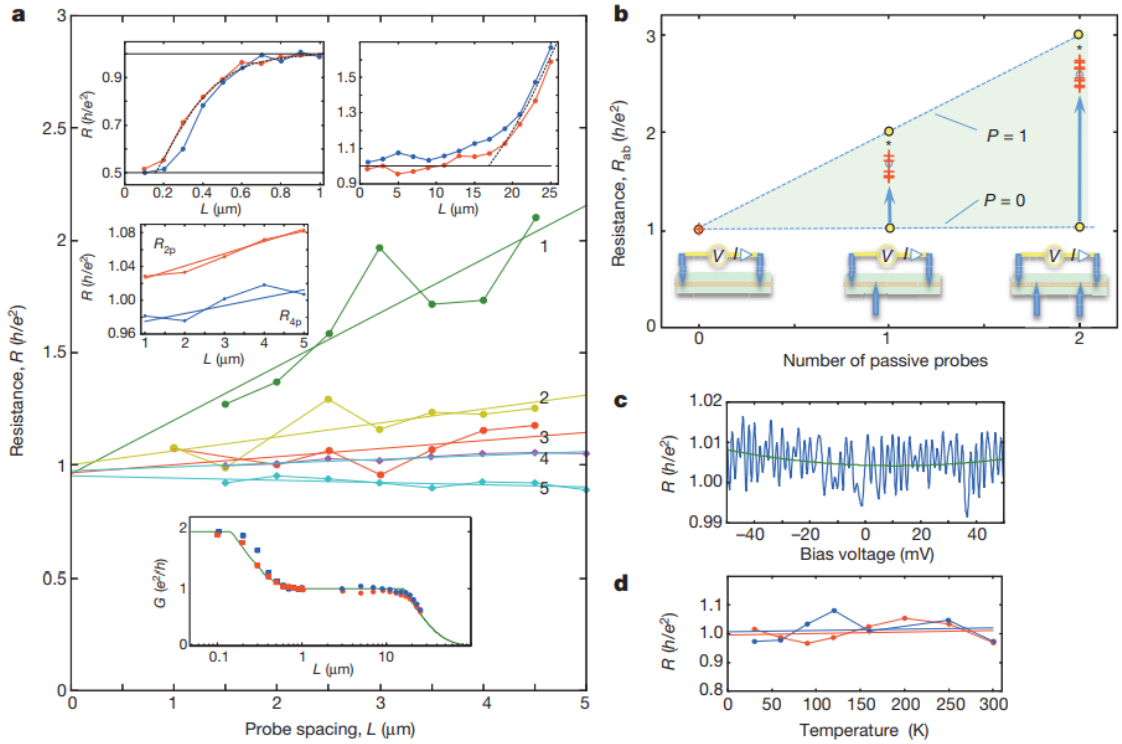

Figure 1.6: a) Resistance versus probe spacing L. Linear fits extrapolate to $R_0 = h/e^2$. Slopes labeled 3-5 demonstrate resistances insensitive to channel length up to 5 μm, characteristic of ballistic conductance. Middle inset, comparison of two-probe (2p) and four-probe (4p) measurements. Upper insets, nonlinear resistance increases observed at L = 160 nm and at L = 16 mm in two different ribbons measured at room temperature, presented as G(L) in the lower inset. b) Effect of passive probes contacting sidewall ribbons. The resistance essentially doubles with one passive probe and triples with two passive probes. Ideal invasive probe (P = 1) and non-invasive probe (P = 0) limits are indicated. c) Resistance of a typical ribbon for L = 5 mm versus bias voltage. d, Resistance versus temperature for the same ribbon, showing less than 10% variation from 30 K to 300 K. From reference [1].

transport measurements using 2-probe STM. My results show that epitaxial ribbons must be epitaxially grown on 6H-SiC along the ZZ-orientation to measure both electronic edge states and length-independent resistance.

CHAPTER 2
METHODS OF GRAPHENE FABRICATION AND CHARACTERIZATION

This chapter describes fabrication methods used to grow and functionalize graphene and the spectroscopy methods I used to characterize my samples. I will briefly review the variety of ways to fabricate graphene sheets. Many of these techniques suffer from lithographic constraints or chemically implanted defects. In my research, I focus on epitaxially grown graphene on SiC in two geometric configurations; nanoribbons on SiC facets walls and the flat interfacial buffer layer (discussed in sections 2.4.2 and 2.3.3 respectively).

2.1 Mechanical Exfoliation and Deposition Methods

In 2004, the technique of exfoliating single graphene sheets from graphite followed by transferring them to an insulating substrate (quasi-free standing exfoliated graphene) led to a new interest in graphene's electronic properties. Repeatedly cleaving graphite using an adhesive results in high mobility single-layer graphene flakes [10]. Experiments on exfoliated graphene led to the confirmation of superior tensile strength due to the strong in-plane σ-bonding. The measured in-plane Young's modulus is close to 1 terapascal, one of the largest to date [28]. This form of graphene is electrically similar to the ideal planar material in that it demonstrates linear dispersion at the K-point [10].

However, mechanical exfoliation lacks the scalability required for practical application and the physical transfer to a device substrate degrades the quality of the graphene flake. In addition, using mechanically exfoliated flakes to study the properties of selectively oriented graphene ribbons is extremely complicated. Atomic-scale STM characterization and lithography on randomly deposited graphene flakes is required to investigate or exploit edge states associated with the ZZ-edge orientation [29, 30].

Many graphene fabrication methods have been studied for the purpose of realizing

an easily assembled, commercially applicable nanodevice. The first large-scale graphene sheets were developed using reduction methods of graphene oxide (GO) [31]. This method remains popular today as an inexpensive way of forming large, uniform sheets of graphene that are electronically isolated from the reduced graphene-like sheets above and the insulating substrate below [32, 33]. However, the oxygen functional groups introduces large numbers of defects. The resulting material gives poor mobilities to existing commercial semiconductors and suffers from the same lithographic constraints as exfoliated graphene [34].

Chemical vapor deposition (CVD) has been used to develop uniform, scalable few-layer graphene (FLG) and monolayer graphene (ML) sheets. Carbon-gas mixtures react with heated metallic films, commonly copper, to produce atomically flat graphene aligned with the crystal domains of the metallic substrate. Some transition metals (ie. Cu, Ru) produce controllable layer growth from a self-limiting growth process and achieve mm-scale single sheet graphene with mobilities up to 16,000 cm^2/Vs (Cu substrate) [35, 36, 37]. The mobility of CVD graphene is superior to that of GO reduction methods, but the graphene must be physically transferred to an insulating substrate to perform transport measurements that degrades the film quality and scalability [38, 39].

For edge-state characterization, it is necessary to lithographically etch narrow GNR from sheets of graphene as fabricated above. However, even at the constrained limits of STM lithography on graphene flakes, edge disorder produces location-dependent superstructures from scattered electrons off of edge defects, a significant confounding variable in GNR engineering [29]. The last graphene method I describe already produces graphene at a known orientation and allows for nanometer-scale width selection without the necessity for direct ribbon lithography.

2.2 Epitaxial Graphene

For my research, I used the epitaxial graphene (EG) growth method. EG growth has been characterized on SiC substrates since the first work by Van Bommel in 1975 [40]. When SiC is heated to temperatures above 1200 C in ultra-high vacuum (UHV), silicon atoms evaporate from the surface. The carbon left behind reorders to form graphene sheets on both the $(000\bar{1})$ carbon (C-face) and (0001) silicon faces (Si-face). The underlying hexagonal crystal structure of the SiC substrate couples with the graphene honeycomb to force crystalline homogeneity across the epitaxial graphene layers. Using higher growth temperatures in UHV anneals defects and natural SiC step edges for larger epitaxial graphene terraces, but also increases the layer growth rate [41]. Early spectroscopy measurements demonstrate that many layer growth results in a characteristic graphite electronic structure and lattice constants [42, 43]. Later, layer growth restrictions determined that the electrical and structural properties of graphene on the two faces develop differently [44, 45, 46, 47].

2.2.1 C-Face EG growth

On the SiC $(000\bar{1})$ C-face, graphene sheets grow rapidly and have many orientations with respect to the $(000\bar{1})$ surface normal of the SiC sample [48]. These rotations still demonstrate some preferred orientational structure. X-ray diffraction (XRD) measurements show that graphene layers rotate with respect to one another at a preferred angle of acos(11/13), or about 32.2 degrees. Graphene on the $(000\bar{1})$ face demonstrates much larger grain sizes, or distance between crystalline boundaries, than the graphene grown on the (0001) silicon face in UHV [49, 50]. However, it is difficult to control the rapid graphitic layer growth on the C-face, making it difficult to investigate the properties of single layer graphene.

2.2.2 Si-Face EG growth

Epitaxial graphene grows at a much slower rate on the Si-face and demonstrates a known 30° rotation to the underlying substrate[51, 49]. The graphene lattice vectors approximate a $6\sqrt{3}$R30° periodic cell with the underlying SiC [40, 49]. This is shown in Fig. 2.1. Points of high symmetry shown in the smaller black diamond produce the 6x6$_{SiC}$ 'quasi-cell' periodicity. This surface interaction can be observed in STM imaging. It should be noted that while it has been assumed that the first graphene layer and the substrate are commensurate, recent work shows that this is not the case (see section 2.3.3). In this thesis I focus on Si-face graphene because of its rotational order, slow growth rate and thickness uniformity.

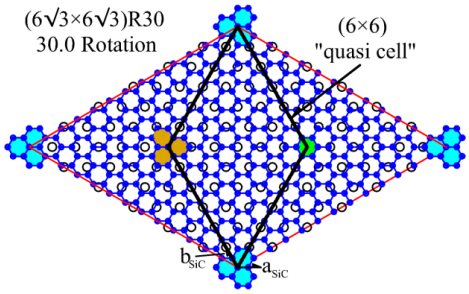

Figure 2.1: The new base cell formed by the top layer of SiC (0001) atoms and the first carbon graphene layer, assuming a commensurate graphene lattice. This is the $6\sqrt{3}$R30° reconstruction outlined in red. The inner diamond in black indicates the (6x6) quasi-cell, the orange and green highlighted cells indicate points of high-symmetry. From reference [48].

2.3 Epitaxial Graphene from Confinement Controlled Sublimation

Investigating single-layer graphene systems requires an even slower growth method than annealing in UHV. In order to approach an equilibrium growth condition, the surface Si

vapor pressure must be equal to the equilibrium vapor pressure at the graphene growth temperature. Emstev et. al. demonstrated that the epitaxial graphene grain size is increased by growing in an inert Ar partial gas pressure. This increases the surface vapor pressure, resulting in micron-order grain sizes as opposed to tens of nanometer-scale grain sizes achieved in UHV growth [52]. An improvement of the Ar-growth method uses a carbon growth furnace. This process is termed confinement controlled sublimation (CCS) and it is the growth method I use for all my graphene samples.

Annealing samples in a capped carbon tube, or crucible, increases the Si vapor partial pressure at the surface, further slowing the growth rate of graphene layers on the SiC faces. Prior to growth, samples are cleaned by a simple organic solvent process and sonication and placed inside a horizontally-oriented carbon crucible. The carbon crucible is placed inside a quartz tube and put into low vaccuum, P_0<9E-6 mbar. The crucible is inductively heated by an external water-cooled copper coil with an RF current (see figure 2.2).

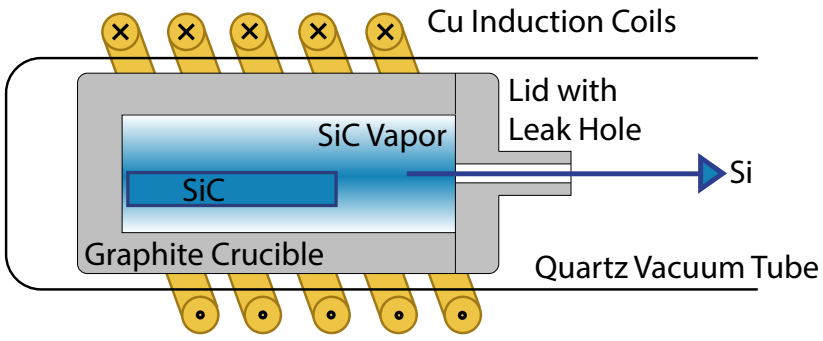

Figure 2.2: Cross section of graphite crucible, the copper coils wrap around and inductively heat it (current direction shown at a point in time), the silicon partial pressure inside the crucible allows for controlled growth at higher temperature, permitting a stable interface configuration between the SiC substrate and EG [41, 53].

During growth, silicon evaporates from the surface, creating a partial pressure inside the crucible. A small hole is drilled into the crucible cap to allow limited vapor leakage

during the growth process [41]. It is not correct to assume that the pressure inside the crucible is the same as the pressure measured in the quartz tube. Silicon adsorbing back onto the substrate increases the growth temperature, slowing the growth rate and increasing graphene order.

2.3.1 Consistent Growth using CCS

Crucible conditions will vary between experimental setups. The temperature and pressure for which layer growth is optimized will vary depending on several factors, i.e. the crucible size, the leak rate through the hole in the cap and the amount of silicon adsorbed onto the crucible walls. A crucible is conditioned by bringing it to the graphene growth temperature (T_{Bake} $\sim$1300 C) for 15 minutes, called a 'bake out'. Then, a piece of SiC substrate is grown with the intended sample recipe after a bake out. This will reestablish a small amount of silicon on the crucible wall and the crucible can be used approximately 10 times before another conditioning bake out is performed.

Consistent sample growth will rely on controlling many experimental parameters, including sample size and number of subsequent growth cycles between bake outs. Details regarding the size and recipes for my graphite crucible are in appendix C. Extensive work has been done in characterizing and optimizing the film growth during the heating process and it is possible to control growth on the (0001) Si-face to just a single graphene layer [54, 8].

2.3.2 SiC (0001) Epitaxial Growth

The first EG layers on the SiC(0001) face have distinct electrical and physical properties. The first graphene layer, the buffer layer (BL), is strongly bonded to the SiC substrate and is semiconductive (see section 2.3.3) [55, 53]. In contrast, the second graphene layer and subsequent layers demonstrate the expected high mobility and the characteristic graphene Dirac dispersion near the Dirac point [56, 6, 55]. The second graphene layer is called the

monolayer (ML).

CCS allows growth on the Si-face to occur layer-by-layer, the first three layers are labeled BL, ML and bilayer (BiL). These layers form in reverse order. As the silicon evaporates from the surface, the first buffer layer (BL_0) forms across the top. The layer closest to the substrate is always called the buffer layer, or interfacial layer. As silicon continues to leave the surface a new graphene BL is formed *under* the existing layer, so what used to be BL_0 becomes the new ML and the underlying layer is notated BL_{ML} (the subscript indicates whether or not a ML has formed above it) [57, 47, 53]. Further sublimation of silicon from the surface forms another BL, and the third graphene layer is the BiL. Figure 2.3 (a) shows the layer order through the growth process and the 4H- and 6H-SiC stacking order. The BL has only been characterized on 4H-SiC at this time, but it is generally assumed that the electrical properties on other polytypes will be the same [34, 47]. Besides exhibiting distinct electrical properties, subsequent epilayers have slightly different lattice constants determined using surface x-ray diffraction (XRD) from reference [47] (shown in table 2.3.2).

Table 2.1: Comparison of epitaxial graphene lattice constants with references.

Carbon Form	Lattice Spacing ($Å^{-1}$)
Graphite	2.460 [58, 59, 60]
Theoretical ML	2.453 [61, 62, 63]
BL_0	2.469 [64, 65]
BL_{ML}	2.462 [64, 65]
ML	2.455 [64, 65]
C-face Multilayer	2.452 [48]

2.3.3 Properties of the SiC (0001) BL_0

The BL holds particular significance for potential graphitic device development because it is a semiconductive layer rather than a conductor. Direct band measurements using ARPES

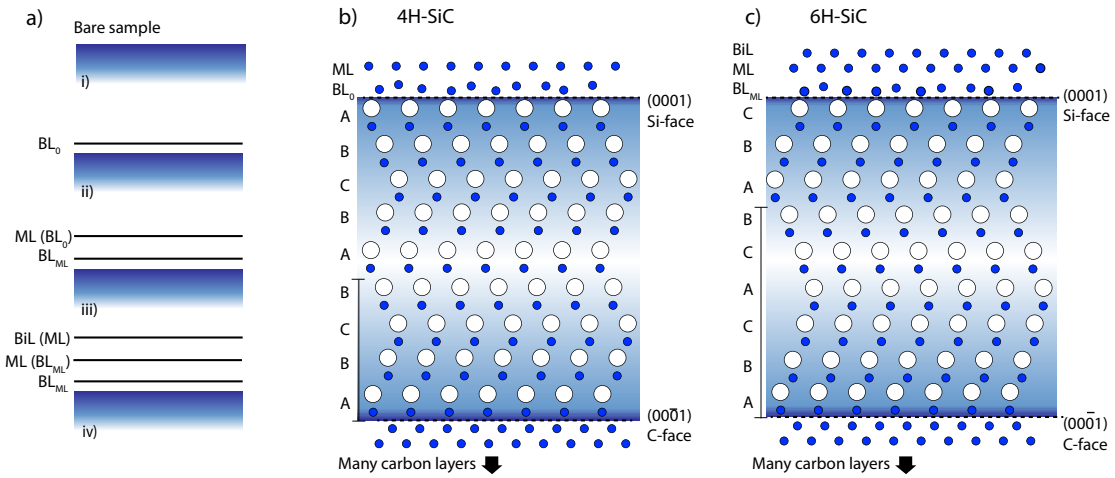

Figure 2.3: a) Layer growth on Si-face, described in text. As silicon leaves the substrate, new graphene layers form underneath the existing layers. Labels in parentheses show layer title from the previous growth step. b) Cross section diagram of 4H-SiC sample with bilayer graphene epitaxially grown on the SiC (0001) Si-face. Many graphene layers grow on the SiC (000$\bar{1}$) C-face. The stacking configuration is marked on the left side, dotted lines indicate the SiC-graphene boundaries labeled with the SiC normal direction. The BL, ML and BiL are labeled. c) Epitaxial growth layers on 6H-SiC, stacking order marked on left side.

show that the top of the BL valence band is 0.5 eV below the Fermi level [55]. The two bands attributed to the BL are labeled ϵ_1 and ϵ_2. ϵ_2 disperses in 3 lobes about the K-point, ϵ_1 lies outside the ML cone as shown in Fig. 2.4. The ML Dirac cone appears after even a slight amount of ML overgrowth (see 2.3.5). The BL bands quickly decrease in intensity as a ML is grown.

ARPES only measures the occupied states of a material, so finding the size of the bandgap requires moving the Fermi energy to show more states in the conduction bands. Cesium deposition has been used to *n*-dope the BL to show that the direct bandgap is at least 0.8 eV wide. After this value, the sample surface is saturated with Cs and further *n*-doping is not possible [66]. Still, this gap is large enough to make the BL an area of interest for those interested in topological devices.

Conrad et. al. was the first to propose that this bandgap was the result of an incommensurate modulation between this first EG layer and the underlying SiC substrate. While ab

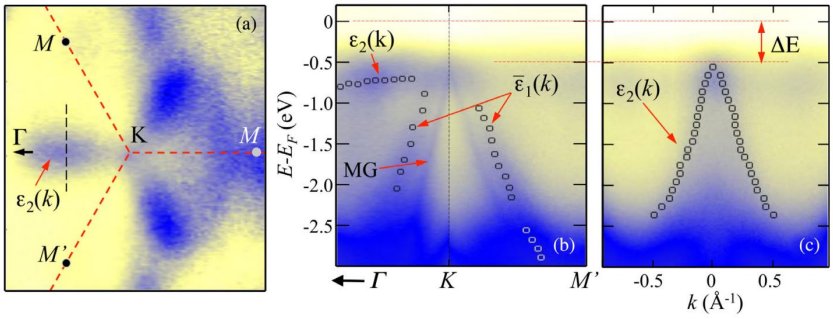

Figure 2.4: ARPES images of a well-ordered buffer layer, a) constant energy cut, E-E_F = .41 eV, showing the lobes of ϵ_2, b) cut parallel to Γ-K-M' showing the locations of the two characteristic buffer bands ϵ_2 and ϵ_1, circles marking the peak intensities in the band, c) cut perpendicular to Γ-K through ϵ_2, as shown by the black line in a) (figure from [55]).

initio TB calculations show that the BL should be metallic, theoretical models based on this modulation produce partially hybridized π-bands surrounding relaxed graphene islands. The semiconductive character is a result of this unique binding structure to the substrate. XRD measurements determine that the lattice constant for the buffer layer is 3.5% larger than that predicted for the commensurate $6\sqrt{3}$ lattice. Figure 2.5 (a) shows the expected locations of the diffraction rods in the commensurate case and the measured locations are shown with circles a distance q away from the (0,1) SiC diffraction rod. Because the length of q is slightly shorter than the commensurate case, the real space lattice constant, a_{BL_0}, is longer than the assumed commensurate length (constants in table 2.3.2) [64].

The other notable result from standing XRD measurements is that the buffer layer interacts so strongly with the SiC that the topmost layers of SiC are no longer equivalent to the SiC bulk [53]. This demonstrates that as the substrate strains the BL_0 and produces a new ordered interface, the BL_0 mutually interacts and deforms the underlying SiC. This is described as a 'mutual modulation'. After a ML is grown on the sample, the underlying buffer, BL_{ML}, has a smaller lattice constant than BL_0 and is now neutral-doped [53]. It is concluded that only the first buffer layer, BL_0, has the desired bonding structure for semiconductive device application.

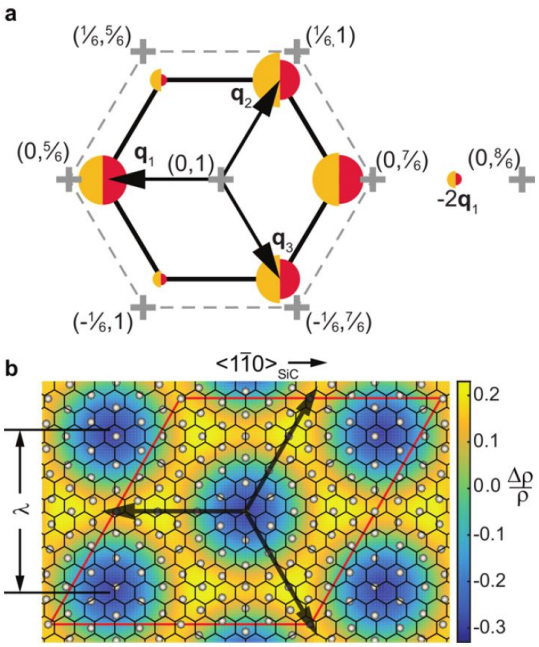

Figure 2.5: Incommensurate modulation leading to BL semiconductive character. a) Crosses mark the expected locations of diffraction rods from a commensurate buffer structure. Circles are proportional to the intensity of the satellite rods around the (0,1) diffraction rod, gold is the measured value and red is the ab initio predicted value. b) Calculated density map of the incommensurate SiC interface. The gray circles and hexagonal mesh overlay represents interface Si and graphene, respectively. The commensurate $6\sqrt{3}$ cell is outlined in red, and not commensurate with the underlying density map. Taken from reference [64].

2.3.4 BL Growth

Since samples are grown using the CCS process, the growth recipe is unique to the carbon crucible design. To ensure sample consistency, the samples are first out-gassed at a low temperature for a half hour, T<500 C, to remove adsorbates. The sample is then heated to $T_S \approx 1190$ C for thirty minutes, initiating silicon carbide step flow, in order to increase (0001) terrace size. The sample is then heated to $T_g \approx 1420 \pm 10$ C where significant silicon evaporation occurs. A complete BL forms in approximately $t_g = 30$ minutes at this temperature. The sample returns to room temperature in vacuum, P ≈ 9e-6 mbar. XPS or

Raman can confirm that only a single layer has grown, see section 2.6.5 and section 2.6.6.

Characterizing graphene sheets often involves using a stable gating mechanism, such as an Al_2O_3 layer. However, there has been no research determining whether the oxide modifies the semiconductive BL_0. There is particular interest in incorporating metal-semiconductor transitions with a ML-BL_0-ML device architecture. I have shown using core level analysis and valence level ARPES measurements that atomic layer deposition (ALD) aluminum oxide film significantly alters the bonding structure of the BL_0 to the substrate. The process involved in fabricating such devices is briefly discussed in chapter 5, the introduction to my research on the effect of aluminum oxide depositions on BL_0 graphene.

2.3.5 Properties of the SiC (0001) ML

The next epitaxially grown layer above the BL is the ML. It forms at a slightly higher growth temperature than the BL_0, T_g = 1550 $\pm$ 10 C for thirty minutes. The ML has linear dispersion consistent with TB calculations of free-standing two-dimensional graphene. Even though the BL_{ML} forms a barrier between the ML and SiC, substrate interactions still cause the ML π-bands to be *n*-doped by $\sim$ -0.44 eV [45]. If a BiL is grown, the substrate interaction with the uppermost layer is much weaker and is *n*-doped $\sim$ -0.2 eV. Figure 2.6 shows a comparison between the measured band structures of a ML sample and a BiL sample. As more layers are grown, the band structure converges to that of neutrally-doped bulk graphite, as would be expected [67].

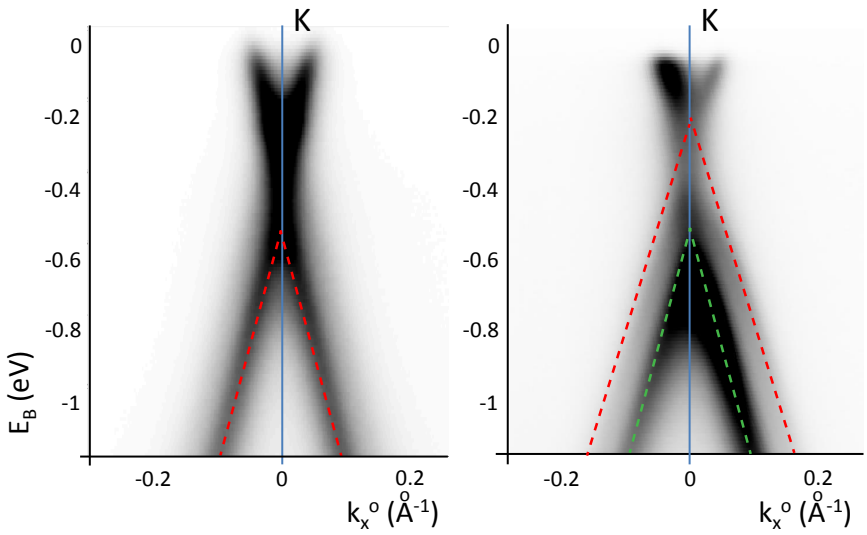

Figure 2.6: a) ARPES image of flat graphene ML Dirac cone. Red lines mark the partially *n*-doped π-bands. b) ARPES image of flat graphene BiL. Red and green lines show the locations of the bilayer bands. hν=36 eV.

2.4 Ribbons Production

2.4.1 GNR Fabrication methods

As discussed in section 1.3, size limiting effects in graphene nanoribbons (GNR) can produce an energy gap inversely proportional to ribbon width and the unique ZZ edge states. This motivates attempts to shrink ribbon widths while maintaining edge order. The ribbons can be produced in a variety of ways; lithographic, chemical and chemical growth from precursor molecules. The lithographic constraint on producing GNR from flat graphene was discussed in section 2.1, I will briefly review some alternative notable methods of fabricating GNR.

'Unzipping' carbon nanotubes with acid and a chemical catalyst was an inventive fabrication method to produce long, highly-ordered and width-controlled GNR. However, this method produces an aqueous solution introducing problems with physical transfer and subsequent treatment of the GNR to restore conductivity [68]. In a different chemical ap-

proach, GNR may be 'cut' out of highly-oriented pyrolytic graphite (HOPG) using a nickel catalyst to hydrogenate bonds along a chosen AC- or ZZ-edge. This process is extremely delicate and the cutting track is deflected from natural defects or free edges. The resulting released shapes are deformed or random [69, 70]. A better control mechanism for edge order must be implemented for this method in order for it to be useful for application.

When grown epitaxially on SiC, graphene nucleates at natural step edges forming ribbons [71]. Growth on these natural SiC steps limits the length scale and placement of the GNR to randomly positioned and oriented steps. It is impossible to isolate these ribbons from curvature effects due to the inherent step topography or control the width of ribbon formation on the natural step [72]. Instead, the ideal solution to the fabrication problems of placement and edge order is found in epitaxial ribbon growth from lithographically patterned trenches.

2.4.2 Epitaxial Graphene Nanoribbons

Epitaxial GNR grown from patterned steps on SiC(0001) are a promising method for designing large scale or in-situ graphene ribbon nanodevices. Metallic ribbons provide conductive channels with high carrier mobilities, and there is an added benefit in that the underlying SiC substrate is already insulating. As with ribbons grown on the natural step, graphene preferably nucleates on these patterned sidewalls before growth on the (0001) flat [54, 72]. Because EG grows at a know 30° rotation to the substrate, pre-patterned trenches in SiC can control both position and orientation of the EG ribbons. AC-edge GNR can be grown along trenches etched along the SiC $(11\bar{2}0)$ direction while ZZ GNR are grown along the SiC $(1\bar{1}00)$ direction (see Fig. 2.7). It is already known that ribbon orientation defines the GNR's electronic character. In this thesis I will show that the ribbon properties are also defined by the choice of SiC polytype. These differences are the subjects of chapter 3 and chapter 4.

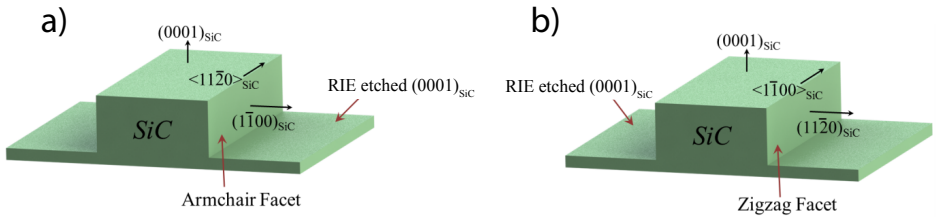

Figure 2.7: a) Trench diagram for armchair ribbon after patterning, sidewalls will facet into (1$\bar{1}$0n) facets after growth. b) Trench diagram for ZZ ribbon, sidewalls facet into (11$\bar{2}$n) facets after growth. Figure from ref. [8].

2.4.3 Epitaxial Sidewall GNR Fabrication from MEMS

The fabrication process begins with a silicon carbide wafer diced to 4x6 mm chips and cleaned using sonication in acetone and isopropanol solvent baths. A photoresist like ZEP or PMMA is applied the silicon-face and patterned using electron beam lithography (EBL). I use ZEP because it is more sensitive to EBL and durable during the etching process [73]. This is imperative to reducing feature sizes in the fabrication process. The EBL pattern draws out the trenches on the resist. The e-beam exposed sample is then developed using amyl-acetate for 2 minutes. Because the ZEP is a negative-type photoresist, the exposed portions of resist are removed leaving the silicon face bare. This is shown schematically in Fig. 2.8 (a).

Reactive-ion etching (RIE) with SF_6 etches the undeveloped ZEP approximately 4.5x faster than the SiC. This means that the thickness of the photoresist should be at least 4.5 times higher than the desired trench depth to avoid etching the tops of the trenches (the undeveloped parts of the resist pattern, see Fig. 2.8 (a)). If the trench tops become etched, the graphene ribbons will randomly nucleate on the trench top instead of along the trench edge. The etch rate of SiC SF_6 is approximately 0.4 nm/s. Therefore to create 20-30 nm deep trenches, the etch time would be 55 seconds and the resist height should be at least

80 nm tall. Shallower trenches require proportionally thinner resist thicknesses and shorter RIE times.

2.4.4 CCS Ribbon Recipe

During the annealing process, the vertical trench walls facet outward and well-ordered graphene grows on the sloped sidewall faces [74, 54, 1]. Some of these trenches are shown in Fig. 2.8. Different facets and substrate types require independent characterization. For instance, previous work by Nevius, et. al. has determined the ideal recipe for growing ordered AC-edge sidewall graphene on 4H SiC, T_g=1560$\pm$5 C for 90 ± 5 seconds [8]. However, I have found that ZZ-edge samples on a 6H substrate require much lower growth temperatures and times (see section 4.1).

Similarly to flat growth recipes, the crucible is first out-gassed at a low temperature for a half hour, T<500 C, to remove surface adsorbents. The sample is then heated to $T_S \approx$ 1190 C for thirty minutes. This step is initiates SiC step flow and helps to stabilize the SiC facets, reducing sidewall wandering after growth. After outgassing and facet-stabilization, the crucible is heated to a ML growth temperature from 70 to 90 seconds. During this time, graphene forms on the sidewalls. For this reason, it is convenient to characterize flat ML graphene growth in a crucible before attempting EG ribbon growth. In my crucible, the ML growth temperature is 1550 $\pm$ 10 C. Higher growth temperatures (+30°C) result in additional graphene layers overgrown on the $(0001)_{SiC}$ flat (determined by XPS and Raman, discussed in sections 2.6.5 and 2.6.6 respectively) [8]. The sample is allowed to return to room temperature slowly in vacuum.

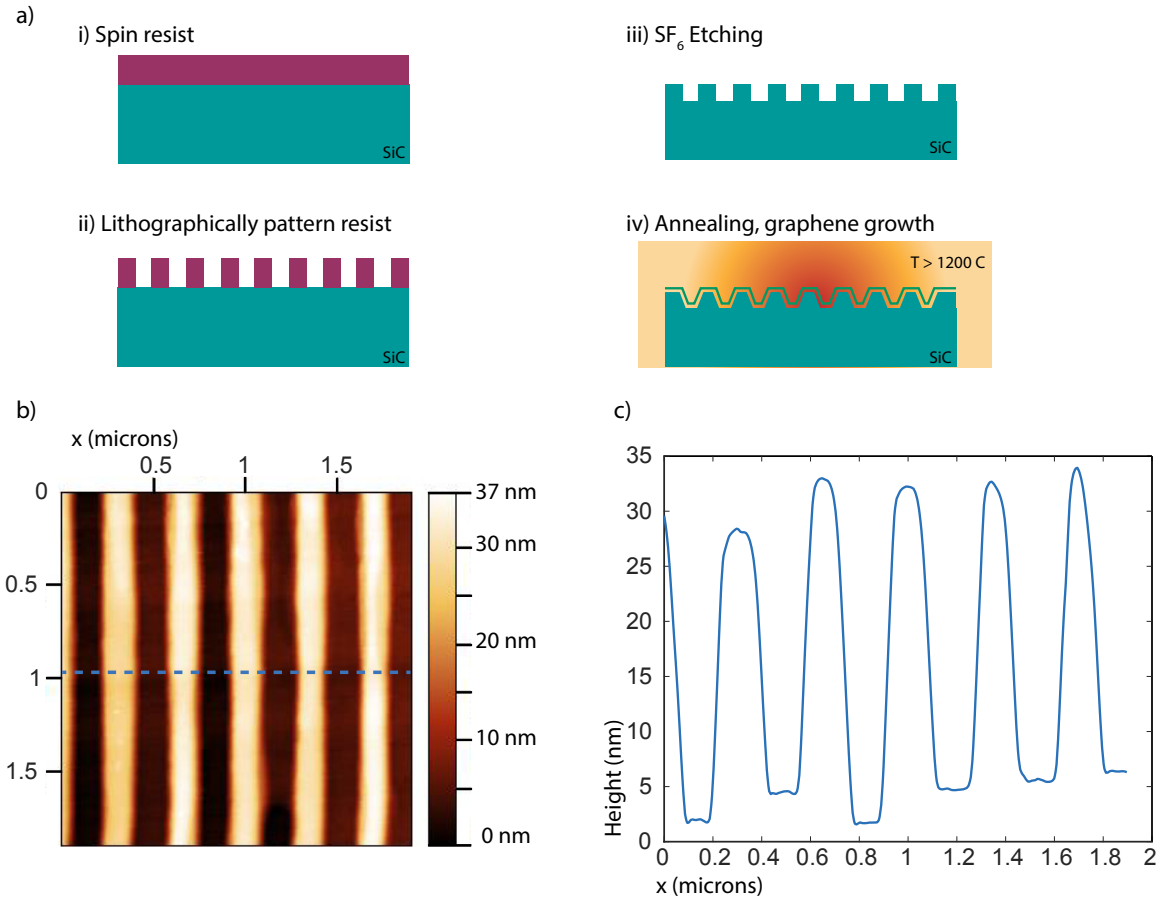

Figure 2.8: a) Schematic of etched ribbon fabrication process. i) Organic polymer is spun to uniformly cover the surface. ii) E-beam lithography is used to pattern trenches in the polymer of 400 nm pitch. iii) Reactive ion etching with SF_6 etches the SiC to a predetermined depth and the remaining polymer is removed with solvents. iv) Annealing using CCS or partial-pressure growth processes form facets of the trench sidewalls and silicon evaporates from the surface, forming a graphene lattice along the sidewall and (0001) surfaces. b) nc-AFM topography of 30 nm etched trenches with 400 nm pitch, post-growth. c) Line profile along dotted line in b), standard 400 nm pitch, 25 nm deep trenches shown.

2.5 SiC Polytype Choice

The SiC polytype plays a crucial role in the growth of sidewall GNR. The free energy $F(\theta)^{SiC}$ plots for two polytypes are shown in Fig. 2.9. Minima in the $F(\theta)$ usually correspond to stable facets. The left side of Fig. 2.9 represents mesas grown in the graphene AC-edge direction. Since well-defined minima are measured for AC $(1\bar{1}0n)$ planes on both 4H- and 6H-SiC, we expect stable AC-edge facets on both polytypes. In contrast, the $F(\theta)^{SiC}$ for ZZ facets (on the right in the figure) only predicts a stable facet for 6H-SiC: the $(11\bar{2}9)_{6H}$ facet at θ_F = 47.5° [2]. Clearly the SiC polytype matters in the facet stability of 4H- and 6H-SiC epitaxial samples for both orientations.

The experimental points on the polar plots were produced with vapor-phase epitaxy of SiC (a growth process involving metallic precursors) on a SiC substrate under near-atmospheric hydrogen pressure (800 mbar), but growth conditions in CCS growth are very different. The resulting stable facets could be very different as well. As I will show, the SiC vapor pressure at the surface and epitaxial graphene growth on the SiC surfaces can and do impact the free energy minimum surfaces. As a result, it is not correct to assume that all stable facets grown under CCS conditions can be predicted by the $F(\theta)^{SiC}$ plots. For example, the free energy minimum from the $F(\theta)^{SiC}$ plot indicates that the $(1\bar{1}05)_{4H}$ should be the preferred facet in AC sidewall samples. TEM studies show that the $(1\bar{1}07)_{4H}$ facet dominates most of the facet wall surface and that there are only short $(1\bar{1}05)_{4H}$ nanofacets (see section 3.1) [72]. So while the $F(\theta)^{SiC}$ plots indicate that the SiC polytype is significant to facet stability, the reported free energy minimums are not necessarily the same as those expected during epitaxial graphene growth, i.e. $F(\theta)^{SiC} \neq F(\theta)^{SiC+EG}$.

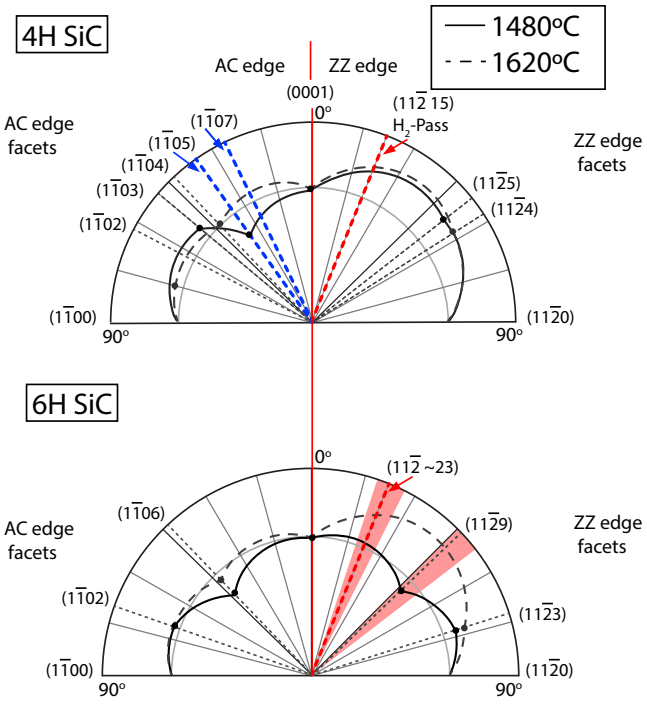

Figure 2.9: Polar free energy plots based on calculated (lines) and experimental (dots) growth rates for two temperatures (adapted from Ref. [2]). Blue dashed lines on the 4H image indicate stable 4H-AC facets were observed under CCS growth conditions [74, 54]. Red dashed lines indicates the angle at which 4H-ZZ facets are formed [8]. Red dashed line on the 6H-ZZ plot indicates experimentally measured facets produced by CCS growth, discussed in Chap 4 [24]. Red shading indicates stable facet observed using TEM on some samples [12].

Typically, the SiC polytype is not considered a variable in EG growth. However, differences in facet structures measured by μ-ARPES [54] and recent measurements in chapter 4 taken with conventional ARPES paint a different picture. For ZZ ribbons, the existence of a Dirac cone originating from sidewall GNR in ARPES is entirely dependent on the selected polytype. The facet cone is only observed from 6H-SiC ZZ-edge sidewalls. It is then likely that electrical characteristics of ZZ-edge ribbons would be very different grown on 4H-SiC versus 6H-SiC.

2.6 Characterization Techniques

2.6.1 ARPES

I used angle resolved photoemission spectroscopy (ARPES) to directly measure the band structure of epitaxial GNR and graphene grown on the (0001) flat. The ARPES measurements were performed in France at the Soleil Synchrotron, a high-intensity variable energy photon source. In ARPES, a monochromatic light source supplied from a synchrotron beamline is incident on the sample. Photoelectrons from the filled states of the sample are produced as a result of the photoelectric effect. The emitted photoelectrons are collected by a hemispherical energy analyzer, as shown in Fig. 2.10(a). Using the measured kinetic energy, E_K, and outgoing angle of the photoelectron, it is possible to determine the photoelectron momentum wavevector magnitude and direction, $\vec{k}$ [75].

$$\begin{aligned} |k| &= \frac{\sqrt{2mE_K}}{\hbar} \approx .512\sqrt{E_K} \\ E_K &= h\nu - E_B - e\Phi_D - E_\Delta \end{aligned} \tag{2.1}$$

where E_K is the measured kinetic energy, E_B is the electron binding energy, $h\nu$ is the incident photon energy, Φ_D is the work function of the detector and E_Δ is the pass energy of the detector (see energy diagram in Fig. 2.10(b)).

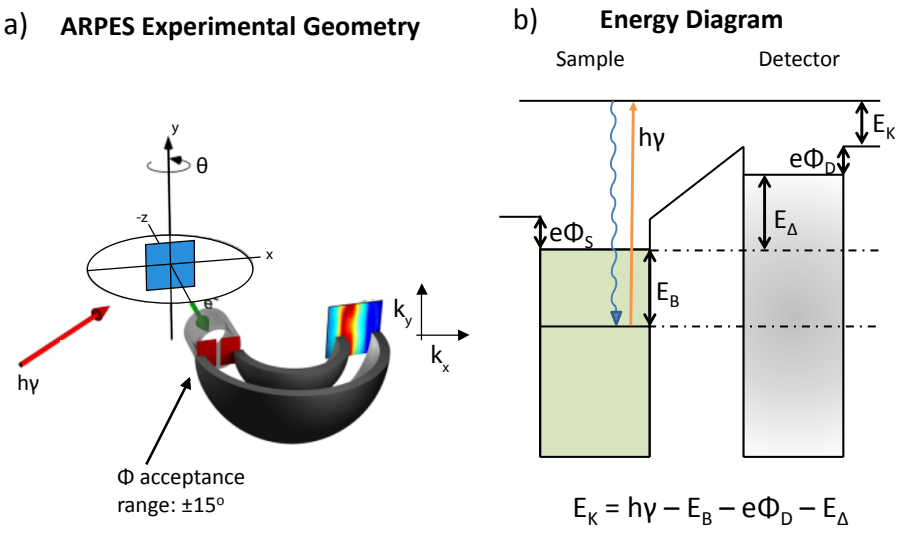

Figure 2.10: a) Simple schema of ARPES experimental geometry, where θ measures the polar angle with respect to the incoming photon beam, ϕ is determined by the acceptance range of the slit. (From physics.bu.edu) b) Energy diagram from substrate to detector for ARPES experimental setup. hν is the photon energy, E_B is the binding energy, Φ is the work function, E_Δ is the pass energy of the detector, and E_K is the measured kinetic energy.

The equations used to determine the direction of $\vec{k}$ from the detector geometry are derived from eulerian coordinate geometry. $|k|$ can be broken into its component vectors, the perpendicular component k_z out of the plane of the surface and parallel components, composed of k_x and k_y. Only $k_{||}$ is conserved in the photoemission process. Because epitaxial GNR samples have several facets, it is necessary to differentiate between the reference frame of the stage normal and the reference frame of the sidewall surface. k_x^o and k_y^o are in the plane of the sample holder while k_x^F and k_y^F are in the plane of the sidewall facet. The sample mounting is shown in figure 2.11 (a).

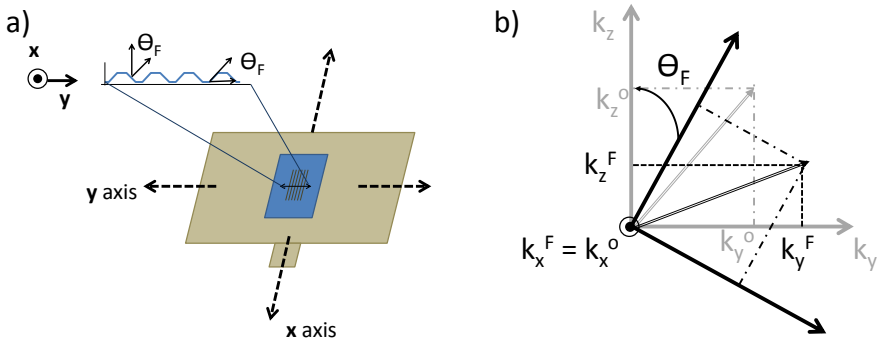

Figure 2.11: a) Schematic of mounting for a ZZ-edge trench sample, trenches aligned with k_x^o. b) A rotation about k_x^o puts the data in the frame of the facet normal (k_n^F, $n = x, y, z$), derivation of coordinates shown in eqn. 2.3.

Data sets are taken in the (0001) reference plane and analyzed in the reference plane of the facet normal (schematically shown in Fig. 2.11 (b)). The coordinate transformation for a sample with trenches aligned with the $\hat{x}$ direction is given as a matrix rotation about $\hat{k_x^o}$:

$$\begin{aligned} k_x^o &= |k| \sin(\theta) \cos(\phi) \\ k_y^o &= |k| \sin(\phi) \\ k_z^o &= |k| cos(\theta) cos(\phi) \end{aligned} \tag{2.2}$$

$$\begin{bmatrix} k_y^F \\ k_z^F \end{bmatrix} = \begin{bmatrix} \cos(\theta_F) & \sin(\theta_F) \\ -\sin(\theta_F) & \cos(\theta_F) \end{bmatrix} \begin{bmatrix} k_y^o \\ k_z^o \end{bmatrix} \tag{2.3}$$

$$\begin{aligned} k_x^F &= |k| \sin\theta \cos\phi \\ k_y^F &= |k| \Big(\sin\phi \cos\theta_F + \cos\phi \cos\theta \sin\theta_F \Big) \\ k_z^F &= |k| \Big(-\sin\phi \sin\theta_F + \cos\phi \cos\theta \cos\theta_F \Big) \end{aligned} \tag{2.4}$$

where θ measures the polar angle with respect to the z-axis, ϕ is determined by the entrance

aperture slit, θ_F is the angle of the facet normal relative to the (0001) normal (shown in Fig. 2.11 (a)), and ξ is a correction related to the entrance aperture optics. My research involved several different sample geometries, they are included in Appendix A, section A.1.

Our samples are brought to the Soleil Synchrotron high-energy photon source for ARPES measurements. The hemispherical Scienta detector has an angular acceptance range of $\phi = \pm 15°$. The ARPES spot size is about 40μm. In order to characterize epitaxial graphene sidewall ribbons, I pattern many rows of trenches. Measuring an ARPES signal with sufficient intensity from a single 30 nm ribbon is not possible. Instead, I use a parallel array of thousands of patterned ribbons. For trenches patterned with 400 nm pitch and a typical ARPES spot size is ~ 40 μm, more than 100 ribbons are simultaneously measured. If the trenches are uniform height and sufficiently parallel, the area-averaged ARPES will be a good representation of the ARPES signal from a single ribbon.

2.6.2 Diffraction Effects in ARPES

While every BZ should be completely identical, it is evident in ARPES that the intensity of the graphene π-bands gets weaker farther from the Γ point. This effect can be observed from a constant-energy scan in k_x and k_y, or a Fermi surface (FS), shown in Fig. 2.12(a). Shirley et. al. demonstrate that this effect is due to a diffraction effect from the graphene unit cell. Intensity of the π-bands varies smoothly around the cone as a result of photoelectron interference from the 2-atom base lattice geometry [76]. This effect is useful in determining the origin of Dirac cones in ARPES measurements, see section 2.6.4.

Well-ordered graphene samples demonstrate additional cones around each Dirac point commonly called replica cones. Their shape has the same symmetry as the K-point Dirac cones. They are the result of the additional periodicity in the BL-SiC interface discussed in section 2.3.3 [64]. They reflect an Umklapp shift of the K-point Dirac cone by a combination of the graphene reciprocal lattice vectors and the incommensurate modulation vector, q. Each replica cone is indexed relative to a local graphene K-point with the vectors from

figure 2.5: G_K(m,n) = m ($\vec{q_1}$) + n ($-\vec{q_2}$). In Fig. 2.12 (b), the indicated replica cones are then indexed (left to right), $G_{(\bar{1}0)}(01)$, $G_{(\bar{1}0)}(10)$, and $G_{(\bar{1}0)}(1\bar{1})$.

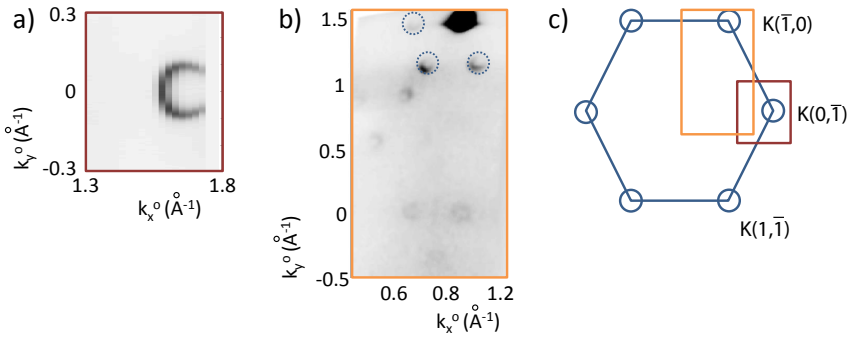

Figure 2.12: a) An ARPES FS taken about a Dirac cone at the monolayer K point, $\theta_K = 36°$. The scan is asymmetrical due to diffraction effects. b) FS showing the location of some first- and second- order replica cones from the incommensurate lattice. The first order replica cones are indicated with dashed circles. E_B = 0.09 eV. hν=36 eV. c) Boxes indicate where the scans in a) and b) are in the first BZ.

2.6.3 Index Determination from ARPES

The facet Miller indices of the stable SiC+EG facets are derived from analyzing the angles at which the signal from ARPES appears in reciprocal space. The known orientation of the SiC wafer is used to set two of the indices, h and k. l is determined after the measurements are taken from equation 2.5.

$$\theta_F = \arctan\left(\frac{2c}{\sqrt{3}a}\frac{\sqrt{h^2+hk+k^2}}{l}\right) \tag{2.5}$$

where θ_F is the facet angle relative to the SiC (0001) normal, h, k, and l are the Miller indices of the facet and a and c are the unit cell magnitudes of a real-space hexagonal crystal lattice, that are unique to the silicon carbide polytype in question. For example, a 23° facet has different l values depending on the SiC polytype. If (h,k)=(1,1), then l is either 23 on 6H-SiC or 15 on 4H-SiC.

2.6.4 Reciprocal-Real Space Geometry Relations

Figure 2.13 illustrates an important challenge of analyzing the ARPES signal from tilted facet sidewalls. The facet cones appear in *pairs*, one from the left side of the trench and one from the right side of the trench. Figure 2.13 (a) shows the real-space trench geometry. The local normal of the (0001) surface is $\hat{n}_o$ and the local normal of the two facets are $\hat{n}_F^+$ and $\hat{n}_F^-$. The angle needed to rotate the sample from the local normal to measure the K-point of the graphene on that facet is $\pm\theta_K$. After the growth process, the trenches facet at angle θ_F. The relationship between the measured angle of the facet cone, θ_{meas}, the measured angle of the K-point, θ_K, and the physical angle of the facet, θ_F is simply:

$$\theta_{meas} = \theta_K \pm \theta_F \tag{2.6}$$

As a result of equation 2.6, measured signals from trenches in ARPES may originate from two possible facet angles. The most straightforward way to determine which angle is correct is to use corroborating spectroscopy, such as AFM, STM, or TEM topographies. If that data does not exist, the facet cone intensity may be distorted by matrix element effects if the sidewall graphene is well ordered. In that case, distinguishing between the two possible θ_Fs is possible by comparing the shape of the facet cones to the symmetry of the (0001) Dirac cones. The asymmetry due to diffraction effects are shown in Fig. 2.13 (b) and (c). While these facet cone locations could be produced from two different facet angles, the asymmetry identifies the correct angle from the facet sidewall. This technique is demonstrated in Chapter 4.

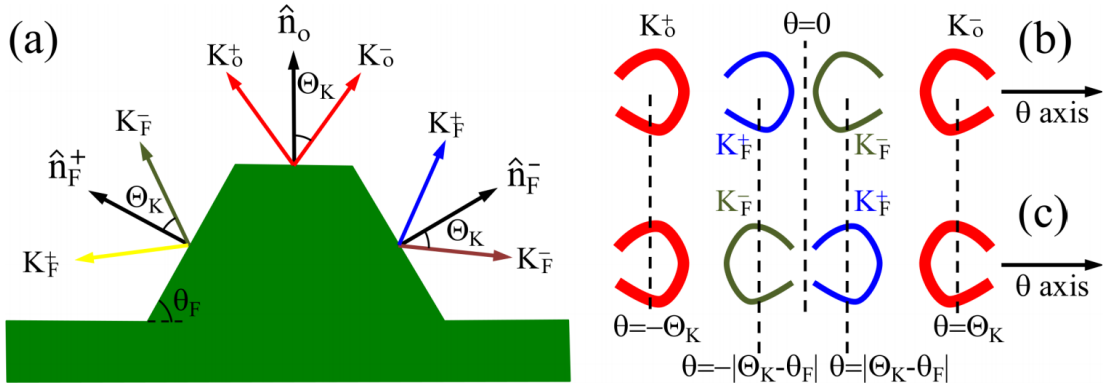

Figure 2.13: a) Schematic of opposing sidewall facets formed after graphitization on an etched trench. The facet angle is θ_F. The local normal is indicated as $\hat{n}_o$ and the facet normal are $\hat{n}_F^+$ and $\hat{n}_F^-$. b) and c) depict a constant E cut through the graphene BZ with the detector axes θ shown. The K_o^+ and K_o^- Dirac cones (red) from the trench tops are indicated. The facet Dirac cones K_F^+ and K_F^- are found at two possible positions, $\theta_K \pm \theta_F$, depending on the magnitude of θ_F as shown.

2.6.5 Conventional XPS

Before samples are transported to a synchrotron, traditional X-ray photoemission spectroscopy (XPS) measurements are taken to pre-characterize layer growth. XPS can determine the surface concentration of carbon and silicon atoms from the core levels of the carbon 1s peak. The Georgia Tech in-house XPS uses aluminum K-alpha radiation to excite core level electrons in ultra-high vacuum as a result of the photoelectric effect. The photoemitted electrons are attenuated by the epitaxial graphene layers as a function of the carbon atomic cross section, σ_g. The decay is exponential, e^{-t/σ_g} where t is the total thickness of the epitaxial layers. By integrating over the relative areas of the composite peaks in a C1s spectra, it is possible to estimate the graphene thickness (and therefore, layer number) on either the C-face or Si-face of an epitaxial graphene sample. The number of layers, L, on the flat, is

derived as follows:

$$
\begin{aligned}
I_{tot} &= I_{SiC} e^{-t/\sigma_g} = I_{SiC} + I_g \\
L &= \frac{\sigma_g}{c_g} \log\left(1 + \frac{I_g}{S_g}\frac{S_{SiC}}{I_{SiC}}\right)
\end{aligned}
\tag{2.7}
$$

where c_g is the carbon layer thickness, I_g is the integrated peak intensity from the graphene carbon-carbon bonds and I_{SiC} is the integrated peak intensity of SiC carbon-silicon bonds. S_g and S_{SiC} are the respective relative atomic sensitivity factors of the selected bonds at a specific incident photon energy.

The C1s peak locations in an BL and ML XPS spectrum are very different. Characteristic spectra from both types of samples are shown in Fig. 2.14 from an Al k-Alpha photon source, hν = 2514 eV. Both spectra have a bulk peak in the C1s spectra at E_{C_B}= 283.7 eV. The integrated are of this peak corresponds to I_{SiC} in eqn. 2.7. The BL has a primary core level peak at E_{S_1}= 285.2 eV, whereas the ML has a narrower primary peak at $E_{S_{ML}}$ = 284.5 eV [53]. The ML C1s peak is shifted toward the bulk peak and produces a higher intensity yield than any individual component of the BL spectrum, so even small amounts of ML overgrowth can be observed as a narrow peak at the S_{ML} location shown in Fig. 2.14 (b). The area of the S peaks in the XPS spectra correspond to I_g in eqn. 2.7 and are related to different bonding structures for the BL and ML, discussed in section 5.3.2.

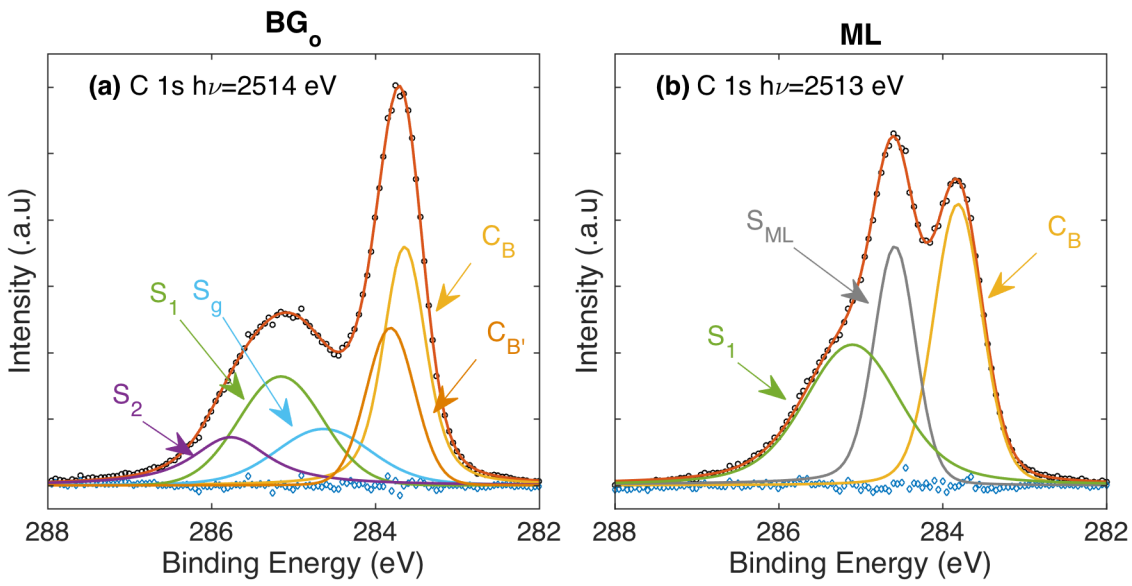

Figure 2.14: Characteristic XPS spectrum for a) BL graphene and b) ML graphene. Used from reference [53]. hν = 2514 eV, taken far from the Bragg angle.

2.6.6 Raman Spectroscopy

Raman spectroscopy can provide chemical bond and structural information from a sample. A high-intensity laser is incident on the sample and some photons are back-scattered. Through inelastic scattering processes, or Raman scattering, these photons have different wavelengths compared to the incident beam. Measuring the difference in wavelength, or the Stokes Shift, provides information about the crystal structure and vibrational modes.

The Raman spectrum of epitaxial graphene has been well characterized at this point. Because it has a unit cell of size two, single layer graphene has six normal scattering modes, three optical modes and three acoustic modes. BL, ML and few-layer graphene produce distinct spectra in Raman because each type of sample is sensitive to different phonon-dispersion modes [77]. The G-peak is caused by an in-plane optical phonon. The G-peak for epitaxially grown graphene is shifted towards lower wavenumbers for thicker samples, making this peak useful for determining layer coverage [78]. The D-peak is due

to forbidden hexagonal lattice breathing modes, but it is allowed due to lattice defects. The breathing modes are also the source of the 2D-peak with twice the Stokes shift as the D-peak. Similar interactions attributed to intravalley processes result in the D'-peak. While the D'-peak can be difficult to isolate due to the broadening of the adjacent G-peak, it is easy to see the D+D'-peak and the D'-Z' -peak resulting from multiple phonon interactions, indicated with black dotted lines in Fig. 2.15 [77, 79]. The graphene D-peak is particularly sensitive to layer growth and is a robust metric in estimating the number of layers grown between 0 and 1 on the Si-face [80]. Peak locations are listed in Fig. 2.15.

Peak	Wavenumber (cm^{-1})
D	1310
G	1590
D′	1620
D+D″	2490
2D	2700
D+D′	2900
2D′	3200

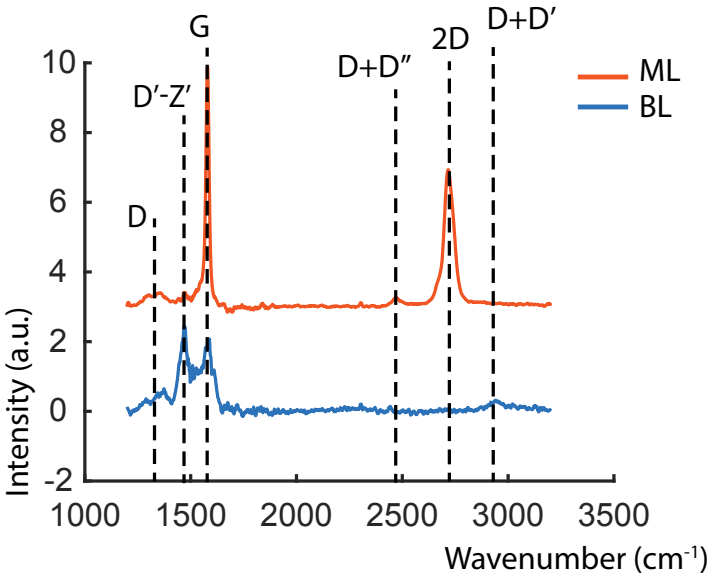

Figure 2.15: A characteristic Raman scan of monolayer (red) and buffer layer (blue) graphene. The identified peaks are labeled with the standard convention. Approximate measured wavenumbers for each peak are given in the table on the left.

Characteristic graphene Raman spectra for both the ML and the BL are shown in Fig. 2.15. The BL is shown in blue. It is identified by the G, D+D', and 2D' peaks. The D+D' peak is useful for identifying a pristine BL sample because it is quickly destroyed with the growth of a ML. The lack of a D+D" peak places a maximum coverage of ML overgrowth to just 3% [55]. The ML Raman spectrum is shown in orange. It has a much more pronounced

G-peak from in-plane optical phonons and the breathing mode 2D phonon becomes evident.

2.6.7 AFM, LFM

Atomic force microscopy (AFM) has been used to characterize the quality of etching, the uniformity of the growth and the regions of overgrowth. Measurements can be taken either through direct contact (C-) AFM or by the deflection of a non-contact (NC-) AFM probe. NC-AFM operates by the repulsion of the probe tip from the sample due to the close-range Van der Waals force. NC-AFM cannot determine the presence of graphene grown from a SiC substrate but provides the root-mean-square roughness of the (0001) surfaces. On the other hand, C-AFM can produce more information about the surface of a grown trench sample. Lateral force microscopy (LFM) with a contact AFM tip is used to perform a lateral scan of a target area on the sample. The lateral deflection of the tip determines topography, similar to NC-AFM. LFM can also determine varying coefficients of friction, μ_k, across a sample by comparing the contrast on the left- and right-moving scans (L- and R-scans). Smaller coefficients of friction produce greater contrast between the L- and R-moving scans, shown schematically in Fig. 2.16 (a).

For a BL sample, ML graphene can grow along the natural steps or imperfections on the sample surface. Similarly, for trenched ribbon samples, small amounts of ML will grow over the edge of the (0001) trench tops. The ML growth along surface defects is referred to as overgrowth. ML graphene has a lower coefficient of friction compared to the BL and therefore demonstrates higher contrast between the L- and R- scans in LFM. For instance, the D+D" peak in the Raman scan in Fig. 2.16 (b) indicates that the sample has a substantial amount of ML overgrowth on the (0001) surface ($>$3%, as discussed in Sec. 2.6.6). Fig. 2.16 (c) shows the R- and L- moving scans across the sample surface. Areas of low friction appear light in the R-scan and dark in the L-scan. Fig. 2.16 (d) shows the difference between the two scans. The dark areas correspond to a lower μ_k, where ML has overgrown along natural steps on the surface (7.6% of the surface). LFM produces an

estimate of the ML overgrowth, but variations in topography such as step edges or trench tops introduce errors in the deviation of the C-AFM tip. A better estimate of layer coverage is determined using XPS.

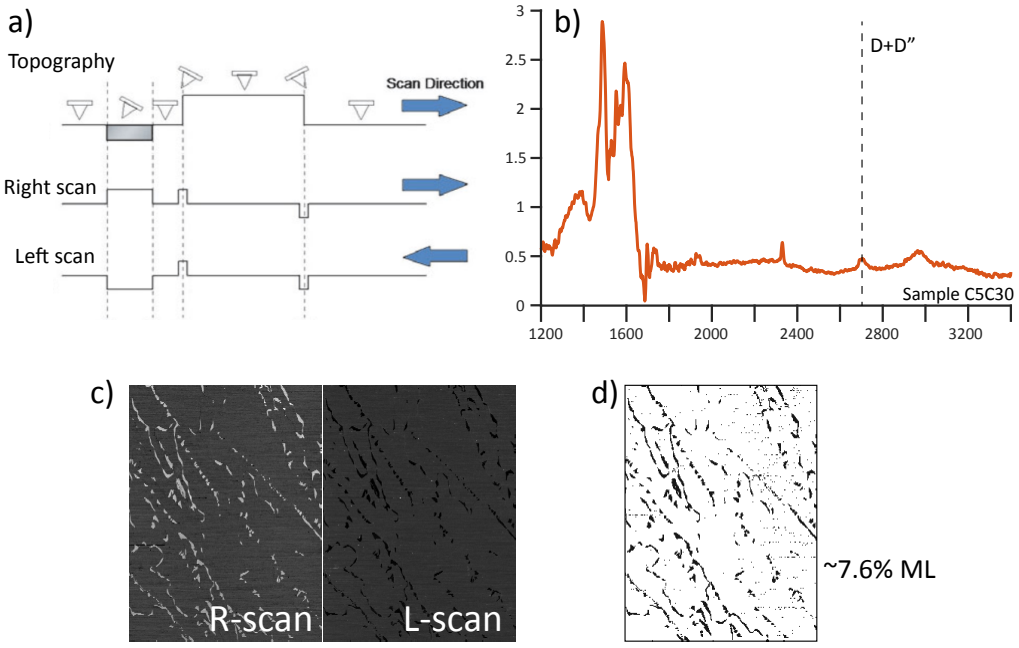

Figure 2.16: a) Schematic of an LFM scan, contrast between the right and left scans indicate areas of high μ_k. From the Instruction Manual produced by Park Systems. b) Raman spectrum of a BL sample indicating ML overgrowth from the appearance of the D+D" peak. c) R- and L- moving scans on the sample corresponding to the Raman signature in a). d) Black and white image of the contrast between the scans in c). High contrast areas correspond to 7.6% of the overall image.

CHAPTER 3

EPITAXIAL GRAPHENE NANORIBBON ON 4H-SIC EXPERIMENT

This chapter reviews the work done in characterizing the electronic and physical structure of 4H-SiC sidewall GNR. ARPES studies were conducted at the Soleil Synchrotron and STM measurements were taken at Oak Ridge National Labs. The results prove that ribbon orientation fundamentally determines the resulting electronic structure of the epitaxial sidewall GNR. Dirac cones originating from graphene on the AC facets are observed in ARPES, but the graphene grown along the ZZ-direction is too strongly bonded to the substrate to produce Dirac cones [74, 54]. Subsequent intercalation of these ribbons with hydrogen on ZZ-edge samples breaks the substrate bonds and the sidewall graphene is released from the substrate, allowing the Dirac cones to be seen using ARPES [8]. I analyze sidewall Dirac cones from hydrogen processed, ZZ-oriented trenches on 4H-SiC and show that they indicate wide ribbons along the sidewalls. Transport measurements taken on 4H ZZ-edge samples with and without H_2-processing demonstrates that they are diffusive conductors.

Through this chapter, I refer to ribbons epitaxially grown on 4H SiC in the AC- or ZZ-orientation as 4H-AC or 4H-ZZ samples, respectively. Samples were grown with recipe described in section 2.4.4. After the 4H-ZZ samples are intercalated with hydrogen (described in section 3.3), they are referred to as 4H-ZZ-H_2.

3.1 4H-AC Epitaxial Sidewall Ribbons

3.1.1 STM on 4H-AC Sidewall Ribbons

STM measurements on 4H-AC sidewall ribbons reveal the specific stable SiC+EG facet. The facet forms at 28.4° and the overlying ribbon nearly spans the entire facet width. Trench height is controlled by RIE etch time, described in section 2.4.3. This determi-

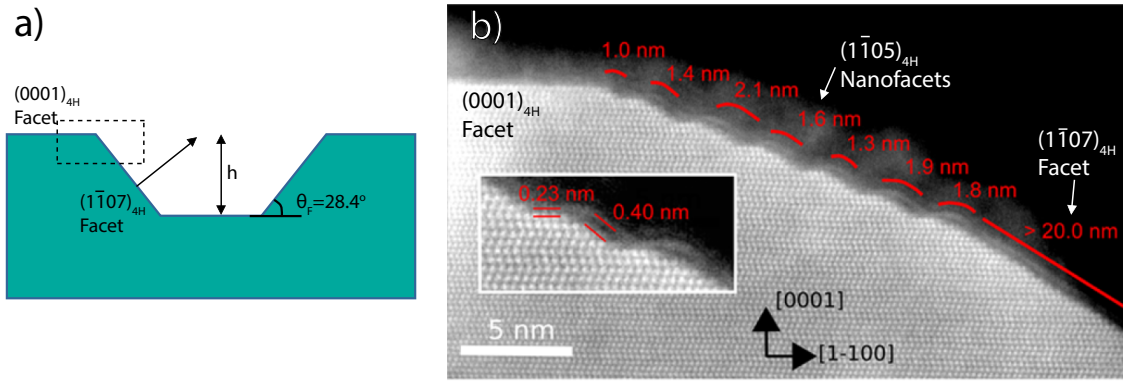

Figure 3.1: a) Faceted AC trench schematic. Trench height and facet angle are indicated. b) STEM image of AC graphene nanoribbon over a region corresponding to the dashed box in a). Inset shows substrate-graphene distance increases over facets as opposed to the small (0001) surfaces. Figure adapted from reference [72]

nes the ribbon width, W_r, to within a few lattice constants. W_r is easily calculated with the height (h) of the etched trench and the known facet angle as follows:

$$W_r = \mathrm{h}/\cos(\theta_F) \tag{3.1}$$

The long (>20 nm) facet is indicated in Fig. 3.1, the angle identifies the facet as the $(1\bar{1}07)_{4H}$ plane.

There are small regions of 'nanoterraces' at the top and bottom of the facet with a different bonding structure than the graphene on the primary $(0001)_{4H}$ flat (see Fig. 3.1). These nanoterraces are short $(0001)_{4H}$ surfaces less than 3 nm long [72]. The substrate-graphene distance along these nano-terraces is 2.3 Å, similar to the out-of-plane lattice constant for the bonded graphene BL. The substrate-graphene distance is much larger on the sidewalls, about 4 Å. This implies that 4H-AC sidewall graphene is more weakly bonded to the substrate than the graphene on the (0001) nanoterraces, implying that they may have distinct electrical structures.

Modeling the density of states (DoS) along the different features of the $(1\bar{1}05)_{4H}$-(0001)

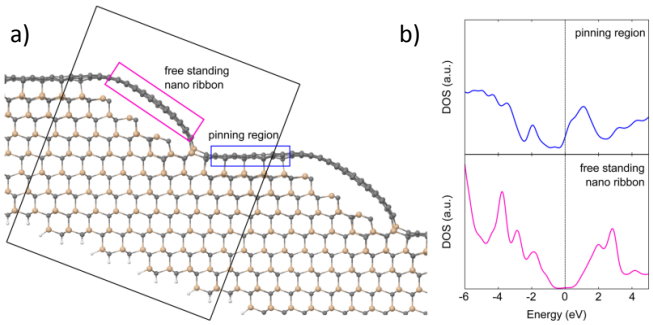

Figure 3.2: a) Schematic of an AC-GNR on a 4H-SiC facet. The pink indicated region is a ribbon that is isolated from the substrate while the blue region is bound to the underlying SiC. b) DoS calculation along both geometries, corresponding the like-colors in a). The pinned region does not demonstrate a bandgap due to DoS, but the freestanding region shows a large bandgap, $\sim$1 eV. Figure from reference [72].

AC facet boundary suggests that $(1\bar{1}05)_{4H}$ sidewall nanofacet is a semiconductor while the (0001) nanoterraces are metallic, as shown in Fig. 3.2. The free-standing ribbon along the $(1\bar{1}05)_{4H}$ facet terminates into the BL on the top flat and into the substrate at the trench bottom. The modeled nanoterraces are entirely bonded to the substrate, then terminate into the adjacent ribbon on the other side. This bonding behavior is shown schematically in Fig. 3.2(a) and the resulting DoS calculation is shown in Fig. 3.2(b). The sidewall ribbon is predicted to have a gap of $\sim$1 eV [72]. However, ARPES suggests that these facets are in fact metallic (see section 3.1.2). This is not surprising, as the model may not correctly represent the way that the 4H-AC GNR terminates into the substrate. Termination geometry has a significant impact on the electronic character of any GNR, as discussed in Sec. 2.4.2.

3.1.2 ARPES on 4H-AC Sidewall Facets

ARPES studies on CCS-grown AC-edge trenches directly measure the average ribbon band structure from epitaxial sidewall GNR. Figure 3.3(a) shows a constant energy surface, E_B = -0.56 eV [8]. Two pairs of metallic facet cones are shown and indicated with green and purple arrows. The Dirac cone from the (0001) surface of the trench tops is marked K_0.

Previous work fitting intensity cross sections of the cones produce values for the π-band locations and broadening in k_y [8]. The cones have an effective Fermi velocity of 0.95 v_F^{ML}

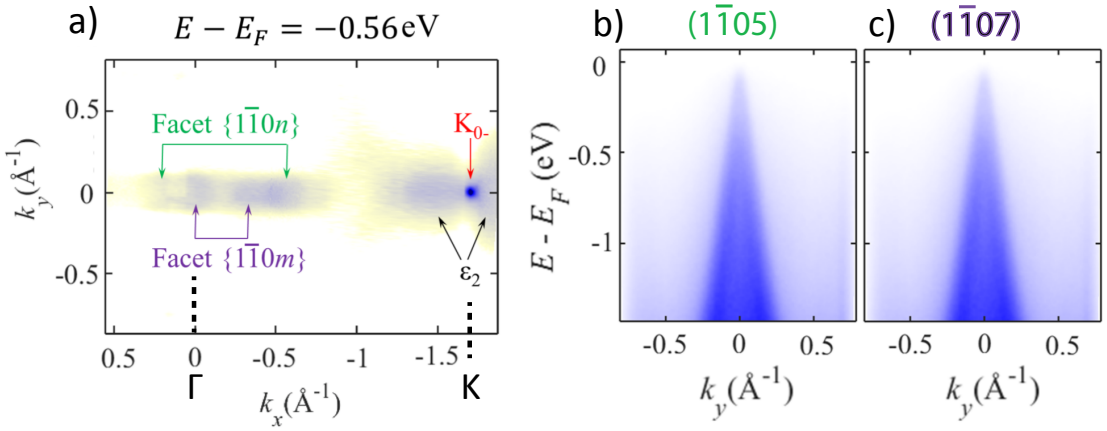

Figure 3.3: a) Constant energy FS of a 4H AC sidewall ribbon sample. Intensity from Γ to K originates from tilted surface with metallic EG. The facet locations are marked with green and purple arrows and indexed with (1$\bar{1}$0n) and (1$\bar{1}$0m) indices, analysis of the ARPES angle show that n and m are 5 and 7, respectively. The graphene K-point from the flat and the graphene BL (described in section 2.3.3) ϵ_2 band are shown. b) Cross section at constant k$_x$ through the (1$\bar{1}$07) facet cone. c) Cross section at constant k$_x$ through the (1$\bar{1}$05) facet cone. From reference [8], $h\nu$=36 eV for all figures.

and are neutrally doped, $E_F \approx E_D$. This would suggest that the sidewall graphene is metallic along these ribbons. The Δk_y broadening, parallel to the trenches, is about 0.059 Å^{-1}, about 6 times larger than the instrument broadening of the detector, $\Delta k_{ins} = 0.01$Å^{-1}. Then an estimate for the coherent long-range order along the trench is $L_y = 2\pi/\Delta k_y \sim$ 106.0 Å. It was shown that these cones are observable for a limited window of growth times and temperatures. The highest quality facet cones (i.e. the smallest Δk_y spreading) are grown using a CCS growth temperature of 1560±5 C for 90 ± 5 seconds [8].

Broadening in original measurements of CCS 4H-AC samples caused mistaken identification of the measured angles and facets [74]. Improved growth processes determine that the facet cones are measured at $\theta_{meas} = \pm(1,7)°$. Given the incident photon energy $h\nu = 36$ eV, the K-point from the flat is measured at θ_K = 36°. Using equation 2.6, the 1° cone indicates a facet angle of either 35° or 37°. There is no possible 35° facet on 4H SiC, so the $[1\bar{1}05]_{4H}$ facet produces the cone measured at $\theta^{meas} = 1°$. Similarly, the 7° cone indicates a facet angle of either 29° or 43°. However, the $[1\bar{1}07]_{4H}$ facet is 28.4°

and the $[1\bar{1}05]_{4H}$ is 43.4°. Both could produce the $\theta_{meas} = 7°$ cone. In this case, TEM measurements determine that the $(1\bar{1}05)_{4H}$ and $(1\bar{1}07)_{4H}$ facet cones are observed [81, 8].

The success in characterizing and optimizing the growth recipe for 4H-AC sidewall samples has not been easily replicated for analogous ZZ-oriented trenches. Work in the AC-edge direction provides a foundation for a CCS process to approach ZZ-edge ribbon development on 4H- and 6H-SiC, the topics of the rest of this chapter and chapter 4, respectively.

3.2 4H-ZZ Epitaxial Sidewall Ribbons

In contrast to 4H-AC GNR, 4H-ZZ GNR do not produce facet cones in ARPES. CCS recipes for a wide range of growth temperatures and growth times fail to produce any measurable Dirac cones from the facet, even to the point where trenches melt. After growth, well ordered graphene is formed on the 4H-SiC (0001) surface of the trench tops with sufficient order for ARPES to measure 2nd-order replica cones in addition to the primary Dirac cone in ARPES. Using higher temperature recipes only produces additional graphene layers on the flat [8]. The lack of Dirac cones from the facet surfaces could indicate that graphene has not grown on the sidewall. It could also be that the graphene has grown but is too disordered to observe in ARPES, or that the graphene has grown on the sidewall but is strongly bound to the surface in a way that severely distorts the facet π-bands. Low-energy electron microscopy (LEEM) studies and hydrogen processing show that the latter case is correct.

3.2.1 Previous LEEM on 4H-ZZ Sidewall Ribbons

LEEM studies first suggested the presence of non-metallic graphene growing along the 4H-ZZ trench sidewalls. When the graphene C1S XPS line is selected for contrast (E_B = 284.6 eV, ΔE = 0.3 eV) the resulting image shows where the graphene has grown [54]. The brightest parts of the image occur along the sidewalls and trench edges, and not on the

SiC (0001) flat (see Fig. 3.4 (b). The XPS spectra taken from different regions (i.e. the main (0001) flat, the trench top and the sidewall) indicate that each has a unique carbon binding structure. The distinct core level spectra from BL and ML graphene are discussed in section 2.6.5. The primary core level peak in the (0001) surface far from the trenches occurs at $E_B \sim 286$ eV, demonstrating that far from the trenches only a strongly bound BL has grown. The (0001) trench tops show evidence of ML growth. For CCS-growth recipes it is common for a small amount of ML graphene to grow onto the trench tops from the sidewall, where the graphene grows the fastest. The $(11\bar{2}n)$ sidewalls show a primary core level peak at $E_B \sim 284.5$ eV, the ML core binding level. Altogether, this is consistent of a trench sample on which graphene has grown fastest on the sidewalls and slightly overgrown onto the trench tops.

XPEEM also demonstrates that the graphene overgrowth onto the (0001) trench tops produce Dirac cones observed in μ-ARPES in Fig. 3.4(d) [54]. Similar to selecting different C1S peaks for contrast, it is possible to select the Dirac point for contrast to indicate the origin of this cone. Unsurprisingly, the brightest potions of the image in fig. 3.4(e) are along the trench tops, where ML overgrowth was already established by core level analysis. In the μ-ARPES image in Fig. 3.4(d), the expected area for ZZ-oriented facet cones is indicated within a red dashed line; no intensity is observed in this area. In fact, even though this sample is grown using a ZZ-trench pattern, the only observed intensity from sidewall facets occurs along the expected AC-facet direction. This may be attributed to small AC-oriented facets occurring naturally from trench sidewall wandering, from natural step growth on the flat or from the AC-oriented trench widths, cut at a 90° angle from the main ZZ trench sides. A composition of the C1S intensity and Dirac cone intensity from the black boxes in (b) and (e) is shown in Fig. 3.4(f). This clearly shows that the graphene is on the sidewalls and trench tops respectively [8]. It does not explain why there is no intensity from the ZZ-oriented graphene ribbons in the μ-ARPES, especially considering that the core spectra more closely resembles that of metallic ML rather than BL. The grap-

hene is either too disordered to be observed in ARPES or strongly bound to the underlying substrate, distorting the graphene π-bands.

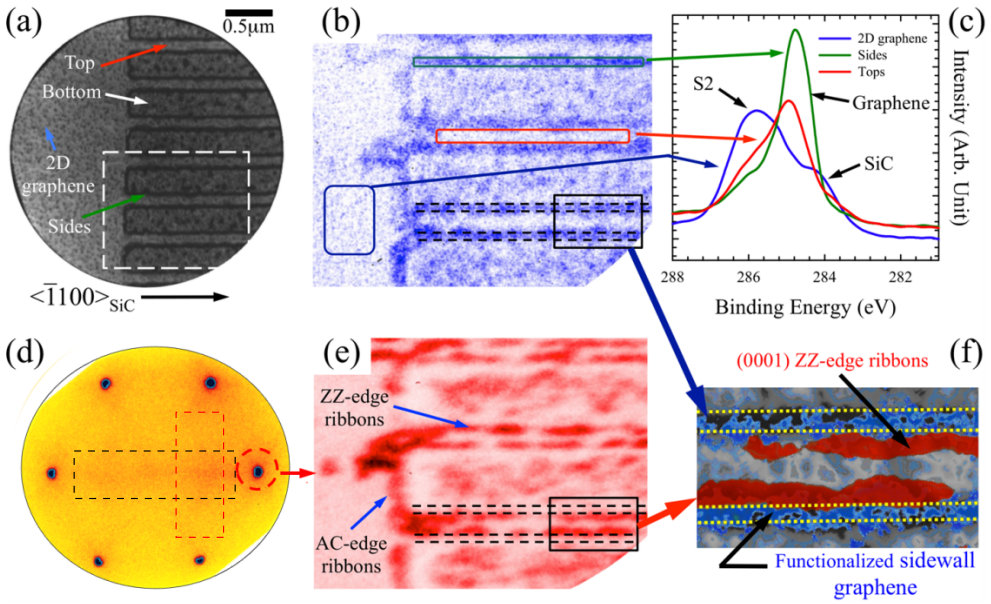

Figure 3.4: a) Bright field-LEEM image of the 4H-ZZ sample, the tops and bottoms of the trenches are indicated. Field of view is 4 microns. b) XPEEM image using the graphene C1s peak for contrast. Image area is the same as the white dashed region in (a). Horizontal dashed lines indicate the top and bottom edges of the sidewall facets. c) XPEEM-derived spectra of the C1s core levels, integrated over the three regions marked in (b). d) μ-ARPES of the zigzag sample (hν = 44 eV). The black box indicates the expected location of AC facet cones, the red box indicates the expected location from ZZ facet cones. e) DF-XPEEM using the Dirac cone (red circle in (d)). The sidewall top and bottom edges are indicated by dashed black lines. f) Composite image of BF-LEEM for topography (gray), XPEEM C1s intensity (blue) and DF-XPEEM intensity (blue). From reference [8].

3.3 H_2 Passivation of 4H-ZZ samples

3.3.1 H_2- intercalation of Semiconductive Graphene

The BL is semiconductive due to the intermittent covalent bonding between the BL and the substrate. If epitaxial graphene samples are put into a heated chamber with molecular hydrogen, the hydrogen has been proven to intercalate in between the graphene BL and the SiC substrate [82]. This creates a quasi-freestanding epitaxial graphene layer above

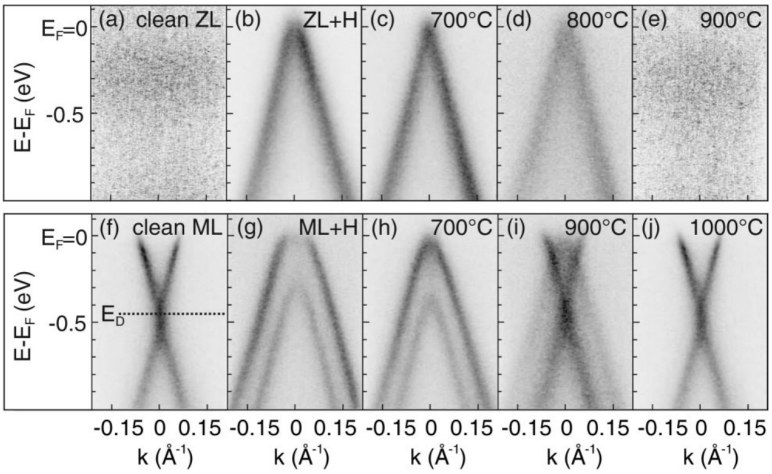

Figure 3.5: Dispersion of the π-bands measured with ARPES perpendicular to the ΓK direction of the graphene BZ. a) A graphene BL on SiC (0001). b) After hydrogen treatment. c) through e) are after subsequent annealing steps. f) A graphene ML on SiC. g) The ML sample after hydrogen treatment, note the split Dirac cone BiL structure. h) - j) subsequent annealing steps. From reference [82].

the substrate. A BL sample is shown in the top row of Fig. 3.5, measured using ARPES before and after hydrogen treatment, (a) and (b) respectively. Afterward, the band structure is similar to that of an undoped ML Dirac cone, shown in Fig. 3.5 (f). The process is also reversible if the sample is annealed at T>900 C in a vacuum. Similarly, the ML sample after H_2-processing showed a BiL band structure, the bottom row of Fig. 3.5 [82]. This is consistent with the hydrogen breaking the covalent bonds between the BL and SiC creating free standing epitaxial graphene layers, electronically decoupled from the underlying substrate.

Similarly, H_2-intercalation on epitaxial sidewall graphene on 4H-SiC breaks the underlying Si-C bonds, releasing the bonded graphene ribbon from the facet surface [8]. This process is performed in a hydrogen furnace at T_H = 900 C for one hour, a simple schematic of the hydrogenation process is shown in Fig. 3.6(a) (further detail can be found in Appendix C). A constant k_y^F cross section of the facet Dirac cone is shown in Fig. 3.6 (b). Characterizing the 4H-ZZ-H_2 sidewall facet cones in ARPES give insight to the structure and order of the sidewall graphene on 4H-ZZ facets.

3.3.2 ARPES on 4H-ZZ-H_2 Sidewall Ribbons

The Dirac cone from the flat is originally slightly *n*-doped due to the Schottky barrier between the conductive ML and semiconductive substrate [48]. The H_2-intercalation is known to electrically passivate the Dirac cone, returning it to a charge neutral state, $E_F \approx E_D$ [82]. This effect is shown with ARPES cross sections in Fig. 3.6(c) and (d), to confirm that the intercalation was completed. This sample originally has a bilayer overgrowth on the SiC (0001) flat and is initially *n*-doped about 0.15 eV. As expected after passivation, the Dirac cone is undoped. This sample has 1st- and 2nd-order replica cones from the graphene-SiC incommensurate modulation. The H_2-intercalant alters the interface interactions, the replica cones are gone and a pair of tilted cones are now observed at $\theta_{meas} = \sim \pm 6.4^{\circ}$. This proves that graphene has grown on the faceted sidewall surface and is ordered well enough to produce the Dirac cones (see Fig. 3.6(e) and (f)) [8]. Hydrogen intercalation isolating the epitaxial sidewall layer is consistent with a strongly bound 4H-ZZ sidewall graphene ribbon, analogous to the strongly-interacting BL on the (0001) flat.

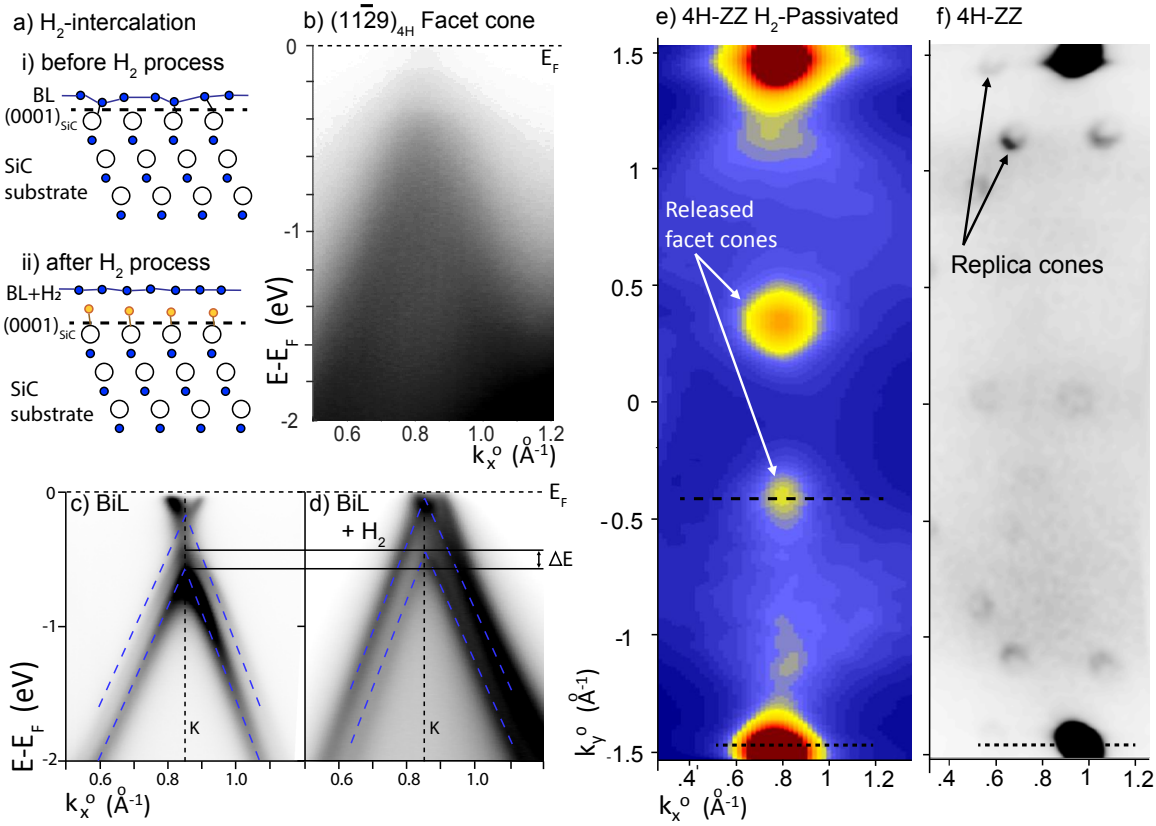

Figure 3.6: a) H_2-intercalation schematic: i) a BL is grown epitaxially on SiC. ii) After intercalation the H_2 molecules bond to the SiC. Si atoms shown in white, C atoms shown in blue, H atoms shown in orange. b) Facet cone along dashed line in (e), k_y^o = -0.45 Å^{-1}. c), d) Dirac cones from flats taken along dotted lines in e) and f) respectively. Blue dashed lines indicate the intensity maxima for the two cones from the BiL, black lines indicate the K point. e) Constant energy FS of standard 4H-ZZ-H_2 trenches after H_2-intercalation, E-E_F = -0.09 eV. The facet cones indicated with white arrows. f) The FS in (e) before hydrogen processing. Replica cones indicated with black arrows. $h\nu$ = 36 eV.

3.3.3 4H-ZZ and 4H-ZZ-H_2 Angle Determination

The facet cones at $\pm 6.4^\circ$ could originate from either side of the annealed trenches, as discussed in section 2.6.4. Early facet Miller-Bravais index assignments were only approx-

imate [8]. θ_K is determined from equation 2.4 to be 30.0^o. It follows from equation 2.6 that the possible facet angles are θ_F=(23.6^o, 36.4^o). These angles closely correspond to either the $(11\bar{2}\ 15)_{4H}$ facet or the $(11\bar{2}\ 9)_{4H}$ facets, at $\theta_F = 23.6^\circ$ or 36.0°, respectively. The facet cones on 4H-ZZ-H_2 samples do not have asymmetrical matrix effects, so ARPES alone cannot determine the origin of these facet cones.

Unfortunately, there are no published TEM measurements taken on 4H-ZZ facets to confirm the precise facet angle. Non-contact AFM measurements taken at Georgia Tech provide a rough estimate for the post-growth facet angle of the 4H-ZZ sample. This sample topography and line scan are shown in Fig. 2.8, in section 2.4.4. The average facet angle over $\sim$10 trench sidewalls in AFM is 24.0 $\pm 1.3^\circ$, determining that the $(11\bar{2}\ 15)_{4H}$ facet is the stable 4H-ZZ surface.

3.3.4 4H-ZZ-H_2 π-band Fitting Procedure, Constraints

To characterize the graphene electronic structure of the 4H-ZZ-H_2 sidewalls, we look in detail at the momentum distribution curves (MDC). MDC are taken for I(E_B, k_x^F,k_y^F) at constant k_x^F and E_B. k_x^F and k_y^F are the components of the momentum vector in the reference frame of the $(11\bar{2}\ 15)_{4H}$ facet, so the coordinates of the facet K-point are (k_x^F, k_y^F) = (0.855, 1.48)Å^{-1}. The MDC is fit using two Lorentzian functions and a linear background. The two Lorentzians represent the two graphene π-bands. These bands have different intensities due to matrix element effects (discussed in section 2.6.1). The facet cone from the sidewall graphene is symmetric about the tilted K-point and slightly n-doped, similar to the (0001) ML cone. First I describe the fitting procedure, then discuss what the facet cone shape tells us about the structure of the 4H-ZZ-H_2 sidewall ribbons.

The locations of the π-bands and the integrated intensity through the curve is shown in

Fig. 3.7 (a-b). The two Lorentzian fit function is given by:

$$\begin{aligned} I(k_x^F) &= Lor_{\pi+} + Lor_{\pi-} + m(k_x^F - k_K^F) \\ Lor(h, k_x^F, w) &= \frac{h}{(\frac{k_x^F - k_K^f}{w})^2 + 1} \end{aligned} \tag{3.2}$$

in which h, k_x^F and w are the height, location and width of the Lorentzian functions and m is the slope of the linear background needed to account for intensity from the (0001) Dirac cone. k_K^F is the location of the facet K-point, centering the linear background about the facet cone.

The π-band fitting results in a symmetric cone shape about the facet K-point, similar to that of ML graphene on the (0001) flat. Intensity from the nearby Dirac cone from the (0001) flat can be seen on the right side of Fig. 3.7 (a). The Lorentzian function close to this intensity will broaden to capture more of the background intensity, shown by the magenta triangles in Fig. 3.7 (c). Initial fits left the widths entirely unconstrained. The widths remain within 15% of each other for the free-width model above excessive background noise, above E_B>1.4 eV. However the deviations in the π-band location increase with fluctuating width below this value. Constraining the widths to be equal ($w_{\pi+}$=$w_{\pi-}$) reduces the deviation in locations, so this limitation is used to determine the location of the valence band maximum. The result equal-width fit values are shown in Fig. 3.7 (c) in black triangles. The symmetric shape of this cone is consistent with wide ZZ-edge ribbons (discussed in section 3.3.5).

The top of the valence band, E_{VB}, is estimated by the energy where the integrated intensity curvature begins to decrease significantly. This occurs at the same energy for which the Lorentzian peak locations meet, $E_{VB} \approx$ -0.2 eV. The minimum width of the constrained fit is $\Delta k_x^F = 0.20$ Å^{-1} (in which both π-bands have the same width), indicating a long range order of approximately L = $2\pi/\Delta k_x^F = 31$ Å. This is three times broader than the cones observed on sidewall graphene on 4H-AC facet walls. This is not surprising

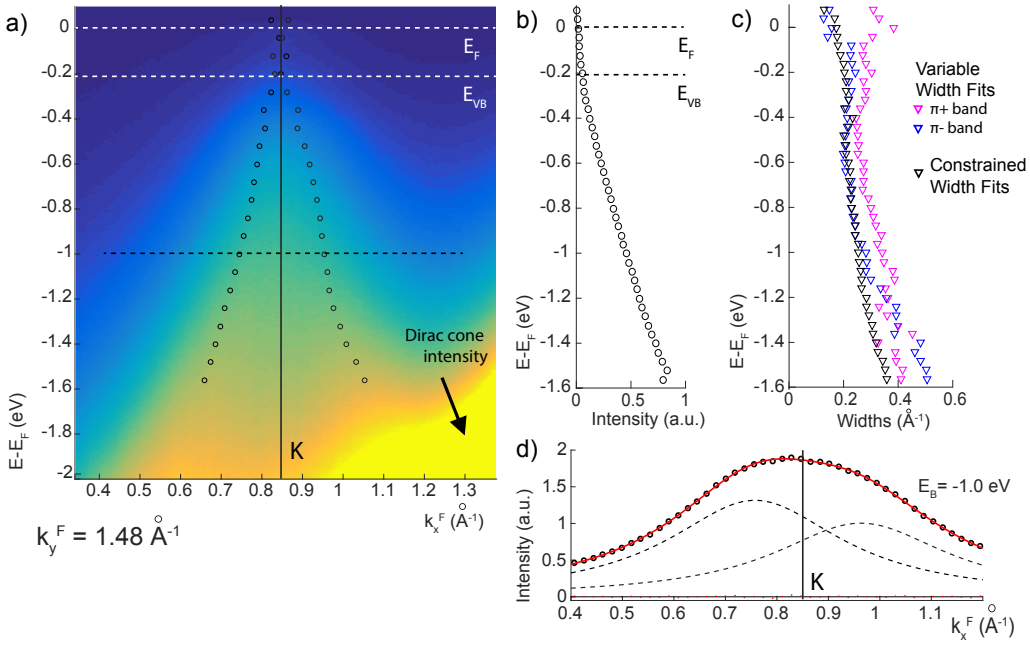

Figure 3.7: a) Intensity cut at constant k_y^F=1.48Å^{-1} at the center of the 4H ZZ intercalated facet cone (in the coordinates of the $(11\bar{2}\ 15)_{4H}$ facet plane). Black circles mark the center of the Lorentzian curves. The facet K-point, Fermi level and top of the valence band are indicated. b) Integrated intensity (a.u.) of MDC fits, E_F and E_{VB} are indicated with dotted lines. c) Comparison of Lorentzian widths when fit using two bands of the same width or two bands of varying widths. d) Characteristic fit along the white dashed line in a), E_B= -1.0 eV. Data is marked in black circles, the fit in a solid red line, the two composite Lorentzians are shown by dashed lines, and the residuals are shown at the bottom. The facet K-point is indicated.

because hydrogen intercalation has been shown to increase the k_x broadening on 4H-AC sidewall samples [8].

3.3.5 E_{VB} of the 4H-ZZ-H_2 Sample from Confinement Effects

The top of the valence bands for the 4H-ZZ-H_2 facet cone is determined from the integrated MDC fits, E_{VB} = -0.2 eV. (see Fig. 3.7(b)). In contrast, after H_2-intercalation the Dirac cone from the (0001) flat is neutrally charged, $E_D = E_F$, as demonstrated in Fig. 3.6(c) and (d). Recall that the (0001) ML Dirac cone is originally *n*-doped as a result of substrate interactions on the (0001) surface. This cannot be the case for intercalated graphene on the

sidewall, instead the top of the valence band of the 4H-ZZ-H_2 ribbons in consistent with the bottom of a band gap that is a result of finite size effects.

An estimate for the size of the ZZ-bandgap due to finite ribbon width is given by the following equation (rewritten from section 1.3):

$$\Delta^0_{GW} = \frac{38}{W_r + 16} \text{ eV} \tag{3.3}$$

where W_r is the size of the ribbon, in angstroms. The first extended state energy band occurs roughly another Δ^0 below the localized edge state (see Fig. 3.8 (a)) [5]. An estimate of the location of the top of the valence band, E_{VB} can be written:

$$E_{VB} \approx -\frac{3}{2}\Delta^0_{GW} \tag{3.4}$$

If the assumption is made that the 4H-ZZ-H_2 sidewall ribbons were actually neutrally doped, then the valence band maximum observed in ARPES is evidence of a small band-gap semiconductor. The measured top of the valence band is located at $E_{VB} \approx$ -0.2 eV. Plugging this value into the above equation yields a ribbon width of 26 nm. This suggests that the graphene decoupled due to the H_2-processing forms a fairly wide ribbon across the facet without intermittently bonding to the substrate.

The symmetric shape of the π-band fitting about the facet K-point is also predicted for wide ribbons with ZZ edges. Using the calculated width, W_r = 26 nm, the number of ZZ chains across the ribbon is N = 260Å/(2.46Å x $\sqrt{3}$/2)$\approx$ 125. TB approximations for ZZ-edge ribbons are shown in Fig. 3.8(b)-(d). All theoretical models show that for wide ribbons (N $>$30), the ZZ-edge band structure approaches that of 2D graphite projected onto the k_x axis with additional localized flat edge states from K to M [4, 17]. While there are no observed edge states in ARPES, it is possible that they exist above the Fermi level or they are destroyed with H_2-intercalation.

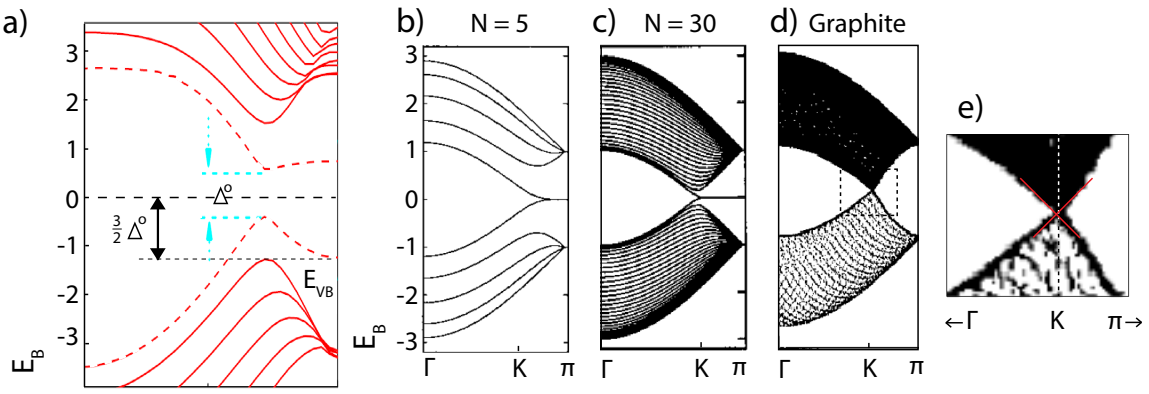

Figure 3.8: a) Band structure from the many-body GW approximation in reference [5]. Localized edge states shown with dotted lines, E_{VB} indicated. b) Tight binding ZZ-edge band structure for narrow ribbons, N=5. c) TB ZZ band structure for wide ribbon, N=30. d) Graphite band structure projected onto k axis. e) inset from (d), at low binding energy the bands are symmetric about K [4].

3.4 4H-ZZ Additional Facets

There is faint intensity shown in the ARPES FS near the (0001) Dirac cones with and without H_2-intercalation. The location of this intensity is shown with dashed circles in Fig. 3.9(a) and (b). They are measured at $\theta_{meas} = \pm 17.8°$. Intensity cross sections of this signal are shown in Fig. 3.9 (c) and (d). This intensity is not from nearby replica cones. Replica cones are too narrow to produce such broad bands. Instead, this diffuse intensity may originate from graphene on a facet sidewall. In that case, the possible facet angles are θ_F = (12.2, 47.8)° using equation 2.6. STM studies did demonstrate a stable ∼50° nano-facet on some samples grown on 6H-SiC after graphene growth, confirming that the facet angle is $\theta_F \sim 47.8°$ [12]. Establishing an exact angle is difficult due to the k_x broadening and distorted shape, Δk_x^o = 0.24 Å^{-1}. The broadening and shape distortion may be the result of disorder along this steep facet preventing the formation of a conic π-band structure.

Hydrogen passivation of a ZZ-GNR sample still shows the intensity of a potential 50° facet (see Fig. 3.9 (g)), but the nearby (0001) Dirac cone and replica cones make it impossible to characterize the band structure of this facet graphene. Further structural work is required to determine the properties of graphene grown on this 50° facet.

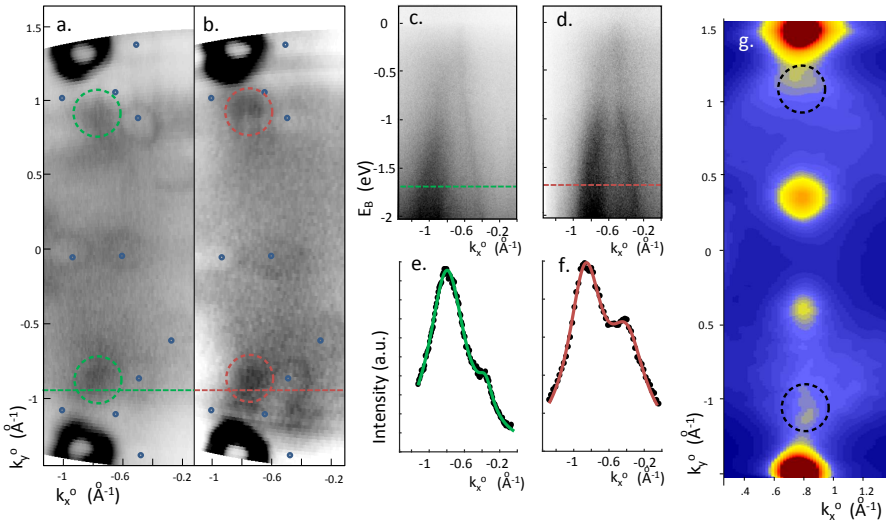

Figure 3.9: Constant energy FS's of two different ZZ samples. a) Sample grown with a buffer recipe preceding the ZZ trench recipe and b) directly grown with a ZZ recipe. c) Constant k_y^o cut taken along the green dashed line in a). d) Constant k_y^o cut taken along the red dashed line. e) and f) show MDC at constant E_B and k_y^o taken along the dashed lines in c) and d), respectively. g) Shows a ZZ sample post H-intercalation. This sample demonstrates some increased intensity about the expected 50° facet location indicated by black dashed circles (E_B = -0.09 eV, from figure 4.3).

3.4.1 Transport on 4H-ZZ and 4H-ZZ-H_2 GNR

2-probe resistance measurements were taken on these samples at Oak Ridge National Laboratory under the guidance of Dr. An-Ping Li. The experimental setup for a 2-probe measurement is shown in Fig. 3.10(a). A voltage is applied across two probes a distance L apart, and resistance R is calculated from the resulting current measurement. The probes are moved farther apart to determine the relationship between channel length and resis-

tance. A linearly increasing L vs. R curve indicates a diffusive conductor. A constant resistance of $\frac{h}{e^2}$, independent of channel length, would indicate a ballistic conductor.

For the 4H-ZZ and 4H-ZZ-H_2 samples, ribbon resistance has a linear dependence on channel length, demonstrating that they are diffusive conductors. The typical ohmic linear regime follows the common formula for resistance, R = $\rho L/wt$, where ρ is the resistivity in units of Ωm, L is the channel length, and wt is the cross sectional area of a rectangle. For a one-dimensional material, such as a nanowire, the resistivity and channel thickness are replaced by a single variable. The sheet resistance, $\rho_s = \rho/t$, is in units of Ω. Then the resistance is calculated R = $\rho_s L/w = R'L$, where R' is the sheet resistance per unit length, $R' = \rho_s/w$ [83]. From the slope of the L vs. R graph in Fig. 3.10(b), R' is calculated for the 4H-ZZ and 4H-ZZ-H_2 samples. $R'_{4H-ZZ} \approx 3.46 \times 10^5\ \Omega/\mu$m for the original sample. After passivation, the sheet resistance per unit length decreases significantly, $R'_{4H-ZZ-H_2} \approx 3.23 \times 10^4\ \Omega/\mu$m.

Scanning tunneling microscopy (STS) measurements rely on the phenomenon of electron tunneling to determine a material bandgap. Measurements are taken by applying a bias-voltage to a probe tip and measuring the tunneling conductance, dI/dV. This is proportional to the local density of states (LDOS). A range of bias-voltages where the dI/dV value is zero indicates a bandgap. Measurements taken on 4H-ZZ and 4H-ZZ-H_2 samples are shown in Fig. 3.10(c). The non-zero LDOS at 0 V tip bias indicates that the 4H-ZZ-H_2 sample is metallic. The same measurement on the 4H-ZZ sample demonstrates that it is a semiconductor with a small bandgap, $\Delta E_{4H-ZZ} \sim 0.15$ V.

To conclude, CCS grown 4H-ZZ ribbons result in sidewall graphene readily observable using PEEM. It can only be seen with ARPES after H_2-intercalation breaks the underlying bonds to the substrate. 2-probe transport measurements prove them to be diffusive conductors, unlike similar ZZ-edge ballistic samples measured by Baringhaus et. al. on 6H-SiC. Given that the different SiC polytypes have different stable facets, it is reasonable to assume that ribbons grown epitaxially on different polytypes will have different electrical proper-

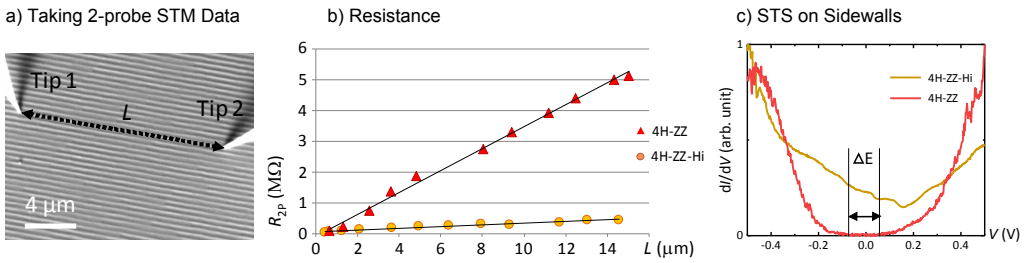

Figure 3.10: a) SEM image of the experimental set up for 2-probe resistance measurements. L is the distance between the probe tips. b) Channel length, L vs. resistance, R. Linear fits provide the R' values in the text. c) STS dI/dV measurements on 4H samples. 4H-ZZ bandgap indicated with black lines. Courtesy of Wonhee Ko at Oakridge National Laboratory.

ties and substrate bonding structures. This suggests that the key to fabricating ballistic-type ribbons depends not only on edge orientation, but on SiC polytype. In chapter 4, I review my results in ZZ-edge ribbons on 6H-SiC. I found that by changing the underlying SiC polytype, both ARPES and transport measurements demonstrate a radically different electrical and structural character for ZZ-edge sidewall graphene.

CHAPTER 4

EDGE STATES AND ELECTRONIC PROPERTIES OF 6H ZZ NANORIBBONS

ZZ-edge sidewall samples grown on 6H-SiC were prepared and brought to the Soleil Synchrotron high-energy photon source for ARPES measurements. In contrast to ZZ-edge ribbons on 4H-SiC, 6H-ZZ ribbons produce Dirac-like cones originating from graphene on the facet sidewalls without hydrogen intercalation. These graphene ribbons give rise to two edge states close to the Fermi level, a feature not observed from any other epitaxially grown sidewall GNR (to be discussed in section 4.4). In addition, STM measurements show that the structure of ribbons grown on 6H-SiC is different from those grown on 4H-SiC. Both STM and ARPES measurements support that graphene on 6H-SiC forms many narrow ribbons. In contrast, graphene on 4H-SiC facets forms wide ribbons spanning most of the facet sidewall. Finally, CCS-grown 6H-ZZ samples reproduce the ballistic transport properties previously measured by Baringhaus et. al., confirming that this phenomenon depends not only on edge type, but the choice of SiC polytype [12].

4.1 Recipes for 6H-ZZ Growth

Several 6H samples were prepared for our ARPES experiments using a range of CCS recipes. Previous work optimizing the 4H-AC recipe demonstrates significant increase in facet order depending on anneal timing and temperature [2, 8]. I explored three different 6H recipes, R^1_{6H}-R^3_{6H}, summarized in table 4.1. Only two of these recipes produce measurable facet cones in ARPES.

Lower growth temperatures and shorter growth times produce better results on 6H-ZZ sidewall ribbons. The best quality samples are determined by the reduced Δk_x^F broadening of the facet Dirac cone widths (fitting procedure discussed in section 4.3.3). The optimal recipe was R^1_{6H}, at a growth temperature T_G=1535 over 70 s. This recipe resulted in the

lowest Δk_x^F broadening of the facet cone and the least Δk_x^o broadening of the Dirac cone on the (0001) flat. A plot of temperature vs. time for this recipe is shown in Fig. 4.1(b), there is a slight delay in achieving the growth temperature as a result of the system's thermal mass. An MDC from E_B= 0.68 eV is shown in Fig. 4.1 (d). For comparison, a recipe with a longer growth time is also shown in Fig. 4.1 (e-f). The Δk_x^F width is larger and the two edge states are not able to be resolved. I grew a single sample with the temperature and time producing the best sample order for 4H-AC samples, T_G = 1560 C, for 70 s. This recipe did not produce any Dirac cones on 6H-ZZ facets as determined by ARPES. This illustrates how recipes cannot be used interchangeably between different substrate polytypes. Table 4.1 compares the Δk_x^F broadening and long-range order for the three growth recipes. The recipe selection was not exhaustive, there is a possibility that even lower growth times and temperatures would produce better ordered Dirac cones from the facet sidewalls.

Table 4.1: 6H-SiC recipe temperatures, growth times, and Δk_x for both the $[11\bar{2}\ 23]_{6H}$ facet cones and $[0001]_{6H}$ Dirac cone. Recipe R^3_{6H}, the ideal growth time and temperature for 4H-AC ribbons, did not result in facet cones.

Recipe	Growth T	Growth t	Δk_x	L ($2\pi/\Delta k_x$)	Δk_K (E_B= .9 eV)
R^1_{6H}	1535 C	70 s	0.075 $Å^{-1}$	83.7Å	0.023 $Å^{-1}$
R^2_{6H}	1550 C	90 s	0.11 $Å^{-1}$	57.1Å	0.028 $Å^{-1}$
R^3_{6H}	1560 C	70 s	na	na	0.030 $Å^{-1}$

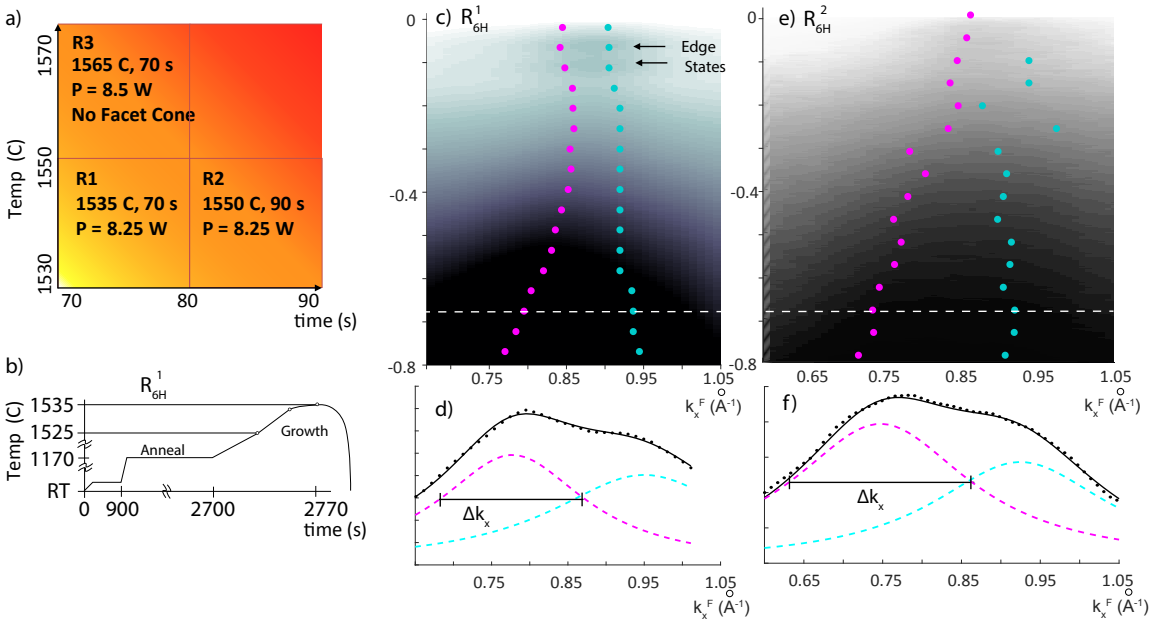

Figure 4.1: a) 6H-ZZ CCS growth recipes. b) Line scan shows a typical growth recipe. c) $(11\bar{2}\ 22)_{6H}$ facet cone observed in ARPES from R^1_{6H}. Edge states are indicated. d) An MDC taken along the dotted line in c), with a characteristic fit. The FWHM of the π^- band is indicated with a black line. R^1_{6H} produces the narrowest facet cone. e) $(11\bar{2}\ 22)_{6H}$ facet cone from R^2_{6H}. f) MDC taken along the dotted line in e), with a characteristic fit. The FWHM of the π^- band is indicated with a black line. R^3_{6H} did not result in any facet cones observable in ARPES. hν=36 eV.

4.2 STM topography on 6H-ZZ

STM measurements were taken to characterize the structure of the $(11\bar{2}n)_{6H}$ facets. 6H-ZZ facets are known to have a complicated structure [84, 85, 12, 86], unlike 4H-SiC AC sidewalls where a single $(1\bar{1}07)_{4H}$ facet covers $\sim$70% of the facet area [72]. A perpendicular linescan across a 6H-ZZ facet is shown in Fig. 4.2 (a). The ZZ-edge steps consist of many $(11\bar{2}\ 22)_{6H}$-(0001) plane pairs (ARPES measurements were used to determine the precise stable SiC+EG facet in section 4.3.1). STM measurements on 6H-ZZ samples find

a large number of very narrow facet widths; 50% of all measured facets were below 3 nm in width. The nano-facet width distribution is shown in Fig. 4.2 (c). Measurements of the facet widths were made on over 300 facets. The ensemble average facet width, $\bar{w_{nf}}$, was found to be 5.7 nm with a deviation of σ = 8.4 nm.

Graphene can bond to the facet in a variety of ways, including distinct edge structures. Theoretical band structure calculations are determined by the nature of the ribbon terminations. Edge structure can determine if a band gap forms and the shape of the dispersion of the ZZ-edge states [87, 17, 20]. Figure 4.2(d) is a STM scan sufficiently resolved to distinguish the (6x6) periodicity on the graphene flat, confirming that the graphene is grown with the ZZ- edge parallel to the trench wall. STM imaging of the facet-flat boundary shows that the bonding structure between the substrate and ribbon is complex. Figure 4.2(f) shows atomic resolution at the facet-(0001) nano-flat edge. There is chiral wandering of the border between the sidewall and nano-flat, further complicating the ribbon edge structure. This is in part due to a 2° misalignment in the trenches patterned on the substrate. These misalignments are byproducts of both the substrate angular error from the producer, Cree Inc., $\pm 2°$, and orientation offsets during the EBL patterning process and wafer dicing process, $<\pm 1°$.

For purposes of structural characterization, we must distinguish whether the graphene forms wide ribbons across the entire facet (as is the case with AC ribbons) or if the graphene is intermittently bonded to the nanoterraces, forming many narrow ribbons. If the graphene flows over the facet-flat boundaries continuously from the trench top to the trench bottom, the ribbon width can be engineered via controlling the initial trench height (similar to 4H-AC trenches). However, if the graphene terminates into the nano-flats, the overall sidewall would be covered in many narrow ribbons. For this case, the distribution of ribbon widths, $N(W_r)$, is comparable to the nano-facet width distribution, $N(w_{nf})$ (where W_r is the ribbon width and w_{nf} is the width of the nano-facets on the 6H trenches). As I will show both ARPES and STM measurements confirm that the ribbon width is equivalent to the nano-facet width, i.e. the facets are comprised of a large number of parallel independent

ribbons.

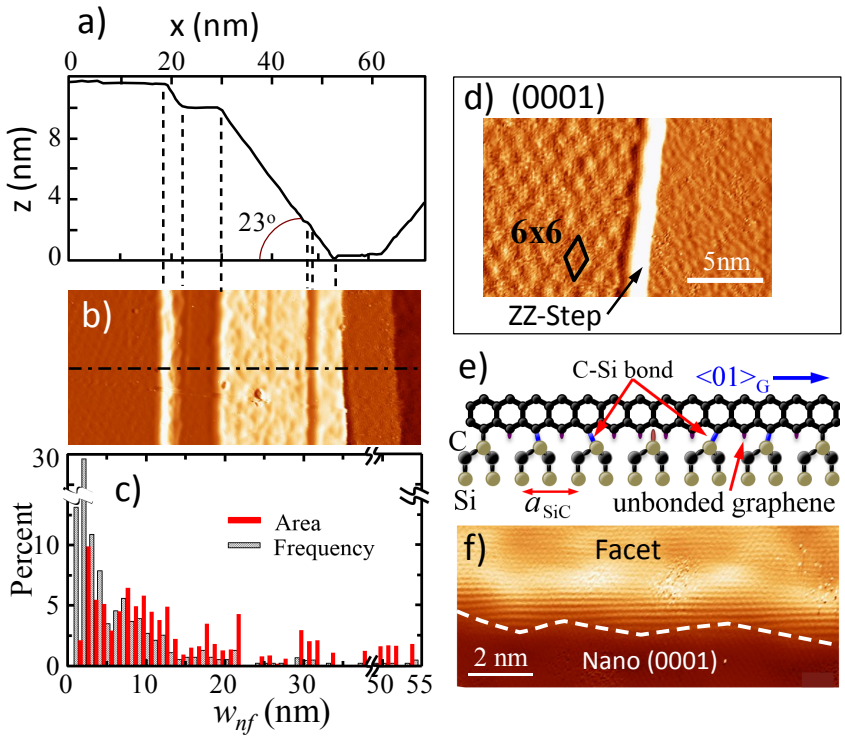

Figure 4.2: a) Profile of a post-growth ZZ trench on 6H-SiC near the bottom of a 25-nm tall step. b) dI/dV image of the profile in a). c) A histogram of the width distribution of facets on the grown step. There are a significant number of 2-3 nm facets. d) STM images on the (0001) flat, showing the 6x6 reconstruction and the orientation of the chosen trenches. e) Bonding schematic of a ZZ edge to a $(6\sqrt{3} \times 6\sqrt{3})R30°$ commensurate SiC substrate. f) Atomic resolution of an angled facet-flat boundary.

4.3 ARPES of Facet Dirac Cones on 6H-ZZ Sidewall Ribbons

Dirac cones from 6H-ZZ facets were measured on 6H-ZZ samples using ARPES. Figure 4.3 compares ARPES intensity cuts at constant energy for the three different ZZ-edge samples (4H-ZZ, 4H-ZZ-H_2, 6H-ZZ). Recalling that the facet Dirac cones were not observed on 4H-SiC before passivation, the bonding of ZZ sidewall ribbons to the 6H-SiC must be significantly different. Figure 4.3(a) shows a 4H-ZZ sample with replica cones as a result

of substrate interactions. After H_2-intercalation, shown in Fig. 4.3(b), the facet graphene lifts from the sidewall and can be observed in ARPES. The substrate interactions are weakened by the H_2-process and the replica cones disappear. In contrast, the 6H-ZZ sample in Fig. 4.3(c) shows both the facet Dirac cones and some first-order replica cones from graphene on the (0001) flat because no intercalation process was necessary to observe the facet cones.

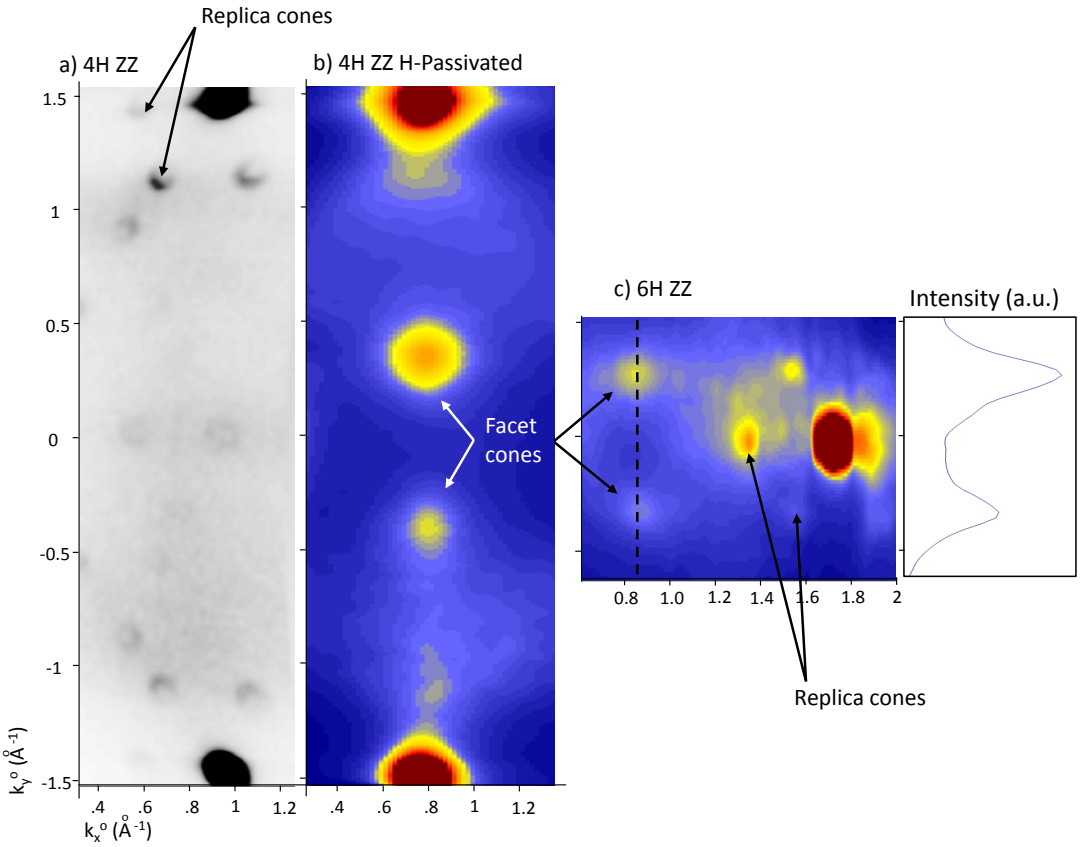

Figure 4.3: FS taken at E-E$_F$ = -.09 eV. a) 4H-ZZ sample b) 4H-ZZ-H_2 sample, facet cones appear after intercalation. c) 6H-ZZ ribbon sample, facet cones and some replica cones indicated. d) Intensity cross section across the dotted black line in c). The maximums occur at $k_y^o = \pm.30$ Å^{-1}. hν = 36 eV for all images

4.3.1 Facet angle determination

The Dirac cones from the (11$\bar{2}$n) facets are measured at θ_{meas} = $\pm 6.1^\circ \pm .5^\circ$ relative to the (0001) normal. Because the trenches are aligned parallel to the k_x^o direction, Dirac cones are observed from both sides of the trenches (discussed in section 2.6.4). Similarly to the case for 4H ribbons samples, the relationship between the measured angle of the facet cone, θ_{meas}, the measured angle of the K-point, θ_K, and the physical angle of the facet, θ_F is:

$$\theta_{meas} = \theta_K \pm \theta_F \tag{4.1}$$

The two corresponding Dirac cones from the (0001) flat occur at $\pm 30.0^\circ$, calculated from the kinetic energy, the known momentum vector and equation 2.4. This indicates that the possible facet angles are θ_F = 30.0$\pm$6.1° = (23.9°, 36.1°)$\pm .5^\circ$.

As previously discussed in section 2.6.2, distinguishing between the two possible θ_F's is possible by comparing the shape of the facet cones to the symmetry of the (0001) Dirac cones. The partial FS in Fig. 4.4 shows the matrix effect induced asymmetry of the Dirac cones originating from the facet and flat. MDC curves are taken parallel and perpendicular to the direction of the trenches and fit with two Lorenztians representing the position of the π-bands. The MDC shown in Fig. 4.4(d) has only one peak, the intensity of the other half of the facet cone has been nearly eliminated due to diffraction effects. The centers of the Lorentzian fits are shown on the FS, indicating the rotation of the distorted facet symmetry. Comparing the shape of the schematically included (0001) Dirac cones and the facet cones illustrate that the facet normal is rotated with respect to the closest (0001) Dirac cone. The correct facet angle is then θ_F = 30.0-6.1=23.9°. This is in agreement with previous TEM measurements taken on 6H-ZZ ribbon samples [12]. The stable SiC+EG facet on 6H-SiC is then determined to be the $(11\overline{2} \sim 22)_{6H}$ facet.

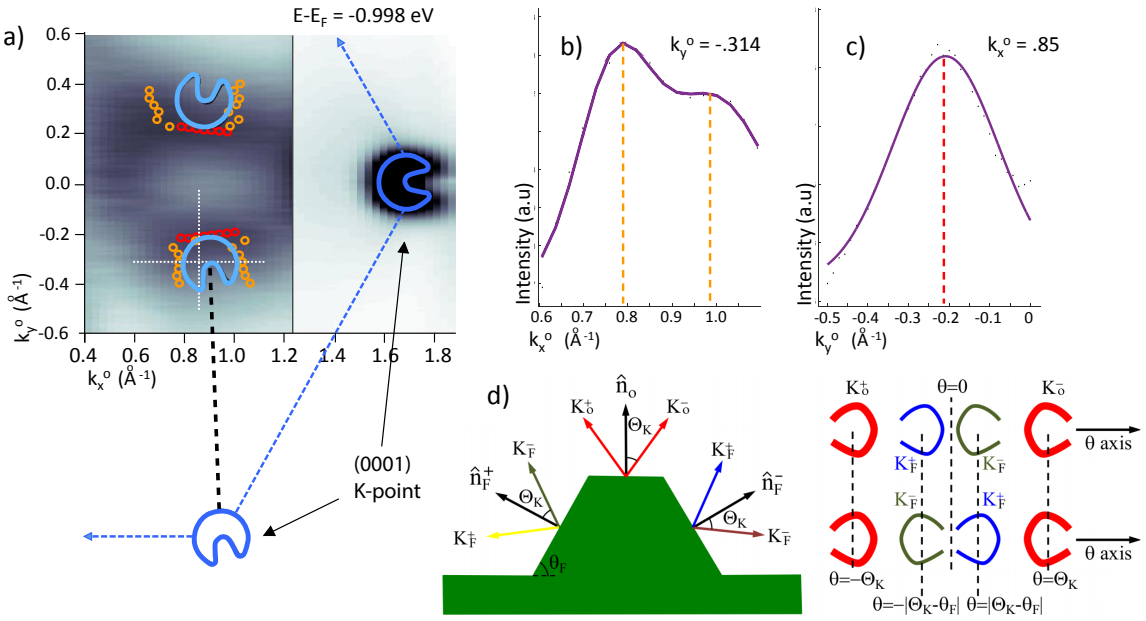

Figure 4.4: a) Constant energy FS showing the facet and flat Dirac cones, E_B = .998 eV. Two different contrasts are used to show both the graphene cone from the flat surface and the weaker facet cone from the tilted facet surface. Orange and yellow circles indicate the location of Lorentzian fits at constant k_y^o or at constant k_x^o. b) Cut across k_x^o shows two intensity maximums through the distorted graphene cone. c) Cut across k_y^o shows only one maximum through the distorted graphene cone. d) Schematic demonstrating how matrix-element effects and BZ symmetry can be used to determine the correct facet angle.

4.3.2 6H-ZZ π-band characterization

The 6H-ZZ facet cones are significantly distorted compared to the symmetric cones from the flat or the 4H-ZZ-H_2 samples. In Fig. 4.5, the first two images are of a $(0001)_{6H}$ ML Dirac cone and a 4H-ZZ-H_2 cone. Circles mark locations determined by Lorentzian fits to the π-bands (fitting described in section 4.3.3). Both of these cones demonstrate the symmetric linear dispersion for E_B $>$ -1 eV about the K point, characteristic of ML graphene or from wide ribbons.

In contrast, it is immediately evident that the cone from graphene on the 6H-ZZ facet is not symmetric. Figure 4.5 (c) shows a cross section of a 6H-ZZ facet Dirac cone. Below E_B <0.4 eV the bands have an asymmetric dispersion with a larger band velocity, v_F, for the π^+ band ($v_F^+/v_F^- \sim 1.7$). Both tight-binding (TB) and ab initio models predict this asymmetry for narrow ZZ-edge ribbons as discussed in section 1.3.1 [4, 23, 5, 17]. In addition to the asymmetry, there is splitting in the 6H-ZZ band structure for BE >-0.4. This will be discussed in section 4.3.4.

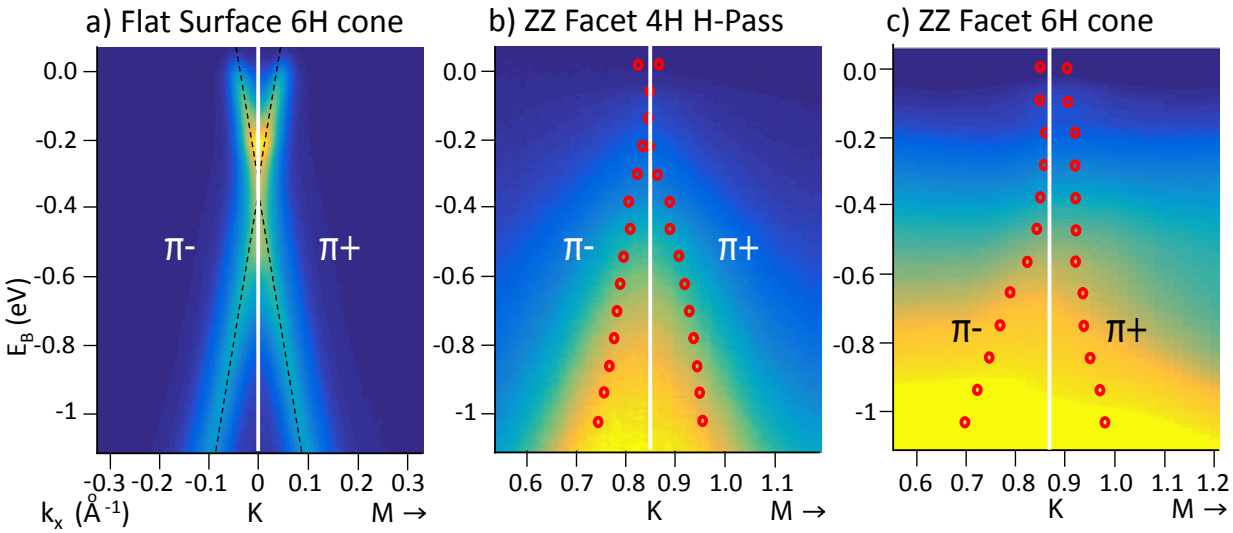

Figure 4.5: a) Dirac cone from the graphene ML on the $[0001]_{6H}$ surface, k_y^o = 1.7 Å^{-1}. Dashed lines approximate the centers of the π^+ and π^- bands. b) Cross section of cone from 4H H-Pass $[11\bar{2}\ 16]_{4H}$ facet, k_y^F = 1.48 Å^{-1}. Circles indicate the locations of Lorentzian functions for each π-band. c) Cross section of cone from 6H $[11\bar{2}\ 23]_{6H}$ facet, k_y^F = 1.48 Å^{-1}. White lines indicate location of K-point for each cross section.

4.3.3 6H-ZZ π-band Fitting Procedure

While in principle the facet π-bands can be fit with just two Lorentzians and a linear background, there is some difficulty as we simultaneously have contributions to background intensity from π-bands originating from the (0001) trench tops. MDCs are taken across

the facet cone through k_x^F, parallel to the trenches at the facet K-point, k_y^F = 1.48 Å^{-1}. To improve counting statistics, each scan is averaged over $\pm$0.2 Å^{-1} in k_y.

A MDC through the facet cone at E_B = 0.16 eV is shown in figure 4.6 (a). There are two distorted graphene π-bands and faint intensity from several nearby replica cones. These wing peaks are the background from the three relatively intense and ordered replica cones marked by green shaded arrows/circles in figure 4.6(a)/(b). Since the replica cone locations and shapes are well known, both the location and width are fixed and modeled using Lorentzians. Replica cone locations in k_x^F are determined by the MDC scan at E_B = 0.16 eV, the two locations of the largest intensity are k_x^F = (.48, 1.3)Å^{-1} $\pm$.02 Å^{-1} (see Fig. 4.6). While there is intensity from a third replica cone (marked by a dashed-arrow in the figure), the intensity is low enough that it is negligible for fitting purposes. The Δk_x broadening of the replica cones is stable and allowed to vary within .01 Å^{-1}, less than 6% of their value. This procedure minimizes the number of free parameters in the fitting algorithm so the replica cones contribution to the background does not significantly effect the π-band fitting routine.

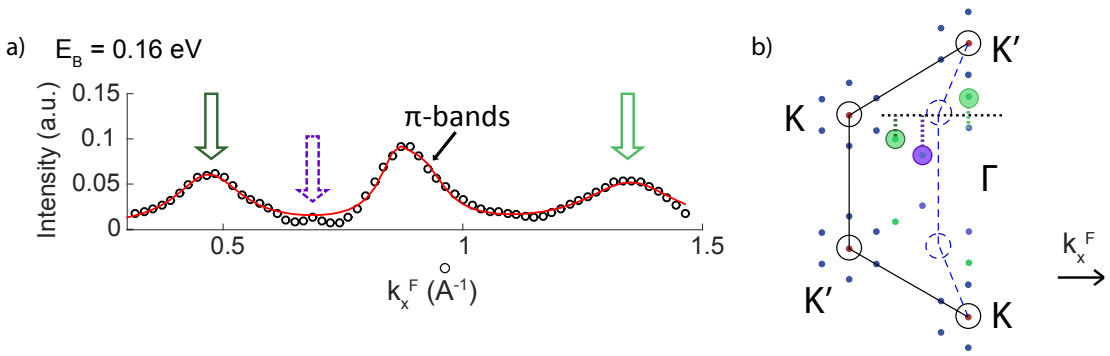

Figure 4.6: a) MDC at E_B = 0.16 eV where there is significant intensity from nearby replica cones. The replica cone locations are indicated with arrows. A sample fit to the data is shown in a red line. b) A partial graphene BZ. Replica cone locations are indicated with blue, green and purple circles. The black dotted line indicates the location of the MDC in a). The three highlighted replica cones are color coded to show where the replica cone intensities observed in a) originate.

I used a linear background to model diffuse intensity in the scan that is attributed to inelastic scattering intensity and the detector background. The equation describing the modeled intensity for a given MDC is:

$$\begin{aligned} I(k_x^F) =& Lor_{\pi-} + Lor_{\pi+} + back \\ back =& Lor_{rep1} + Lor_{rep2} + m(k_x^F - k_K^F) + \Delta_{min} \\ Lor(h, k_L^F, w) =& \frac{h}{(\frac{k_x^F - k_L^f}{w})^2 + 1} \end{aligned} \tag{4.2}$$

where h, k_L^F, w, are the Lorentzian amplitude, position and width, m is the slope of the linear background, k_K^F is the K-point in the reference frame of the facet and Δ_{min} is a direct offset. This function is fit using a least-squares regression algorithm (LSRA).

Some constraints on the facet π-bands were used to eliminate extreme errors in the fitting routine. The locations are constrained to be between the replica cone locations, far

outside the facet cone bounds. I assume this does not significantly affect the fitting routine. There are no constraints on the π-band Lorentzian amplitudes. The resulting locations of the π-band Lorentzian fits are shown with circles in figure 4.7 (a). Some characteristic fits are shown in Fig. 4.7 (b). The conic bands are obviously asymmetrical about the facet K-point indicated with a black line in the figure. For narrow ZZ-edge ribbons, the shape of the band structure should be very asymmetric. The theoretical GW ZZ-edge band structure in figure 4.7(c) shows that for narrow ribbons v_F is different for the π^- and π^+ bands. This asymmetry is the first indication of very narrow ribbons along the 6H-ZZ facet sidewall.

Initially, the π-band Lorentzian widths are unconstrained. I found that the width of the π^+ band is $\sim$1.3 times larger than the π^- band. The GW model shows that the π^+ band side has a higher density of overlapping subbands in energy, as shown with horizontal bars in figure 4.7(c). Because we are measuring a distribution of ribbon widths, the subband asymmetry means that an MDC will sample many more subbands on the π^+-side compared to subbands on the π^+- side. This will make the π^+-bands broader. Constraining the ratio of the π-band widths reduces the deviance in π-band location. The observed splitting of the π-bands at BE$>$0.4 eV occurs regardless of the model constraints applied to the width (discussed in section 4.3.4). I therefore use the experimentally determined factor $\frac{w_{\pi^+}}{w_{pi^-}}$ = 1.3 in my fitting procedure. In addition, the Lorentzian π^+-band width is constrained to be less than .5 Å^{-1} but the π-band widths never approach this value. Fitting variables are given in table 4.2. The fit widths are included in 4.7 (d).

Table 4.2: 6H-ZZ facet π-band widths, locations and boundary constraints determined with the LSRA fitting procedure and equation 4.2. Constraint selection described in text.

Variable	Value	Constraints
w_2	$1.3w_1$	$<.5$Å^{-1}
k_{xK}	.89Å^{-1}	na
k_{x3}^{rep1}	.48Å^{-1}	$\pm.02$Å^{-1}
w_3^{rep1}	.17Å^{-1}	$\pm.01$Å^{-1}
k_{x4}^{rep2}	1.3Å^{-1}	$\pm.02$Å^{-1}
w_4^{rep2}	.24Å^{-1}	$\pm.01$Å^{-1}
Δ_{min}	I_{min}	na

Relative peak intensities are computed by taking the product of width and amplitude, a value that is proportional to a Lorentzian integrated intensity. Then the total intensity (in arbitrary units) from the facet cone is computed as the sum of the pi-band relative intensities. The integrated intensity of the π-bands as a function of energy is shown in figure 4.7 (e). The cone intensity demonstrates a broad decay with an inflection point at $E_B \sim 0.45$ eV indicated in the inset with a black horizontal line. There is intensity in the region $E_B > 0.2$ eV from two ZZ edge states. These states will be discussed in section 4.4.

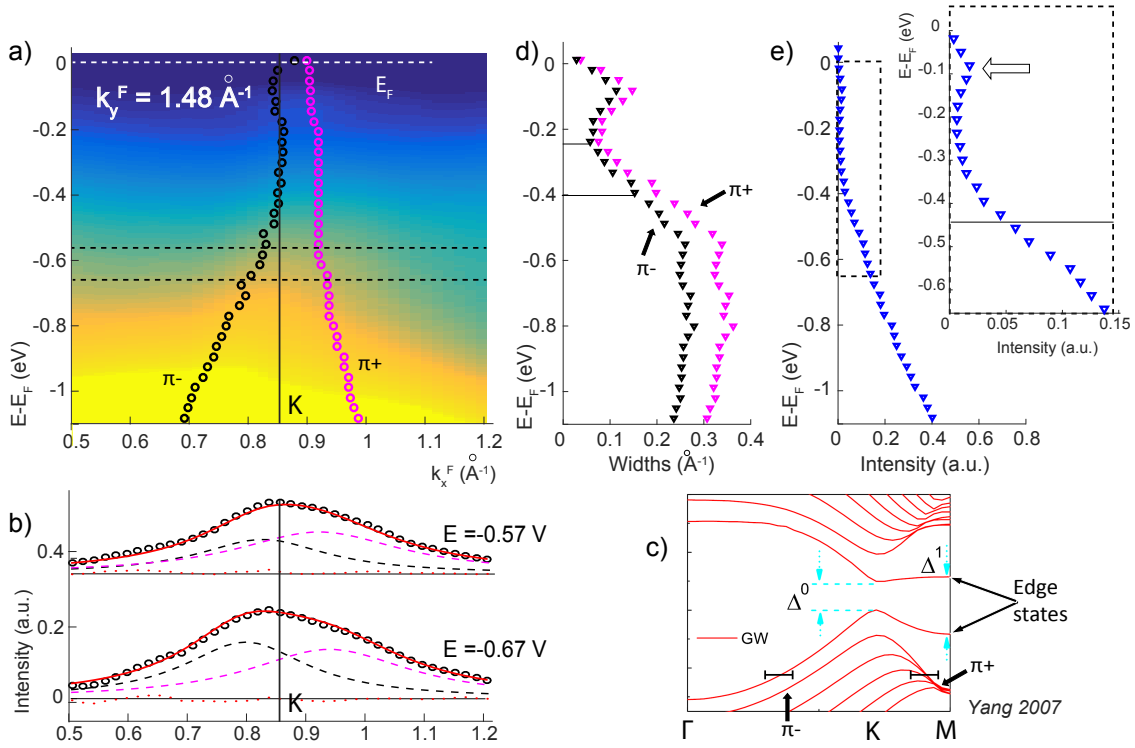

Figure 4.7: a) Cross section through the $(11\bar{2}\ 22)_{6H}$ facet cone. k_y^F = 1.48Å^{-1}, K point and Fermi level are indicated, hν=36 eV, T=300 K. Black and magenta circles mark the locations of the center of the π-band Lorentzian fits (discussed in text). b) Characteristic fits using LSRA at E_B = 0.57 and 0.67 eV, shown with a dashed black lines in a). The data is shown with black circles, fit in red line, the composite π^- and π^+ Lorentzians shown by dashed lines, the facet K-point indicated. Residuals are plotted underneath the fits c) Ab initio calculated band structure of a ZZ-edge ribbon with N = 12. Note that the subbands are much denser in energy on the π^+ side [5]. d) Plot of width versus binding energy through the cone for π^+ and π^- bands in magenta and black, respectively. e) Integrated intensity of π-bands as a function of energy in arbitrary units. Inset: A blow up of the dashed box, arrow shows location of edge states, inflection point indicated with a black line.

4.3.4 Discussion of ARPES Splitting and Ribbon Distribution N(W_r)

The π bands of the $(11\bar{2}\,22)_{6H}$ facet Dirac cone do not appear to cross at any energy. Locations in k_x^F become nearly independent of BE. The values stabilize at k_x^F = [.85, .91]$\pm$.005 Å at E_B >-0.4 eV, shown in Fig. 4.8 (a). While this seems unusual, this phenomenon is consistent with finite size effects from the measured width distribution. To demonstrate this, I use a TB model for the ribbons band structure. In this model for the ZZ-edge structures, the n=0 energy subband corresponds to the ZZ edge states. The k_y wave vector is imaginary for this state, localizing the wave function to the ribbon edge for k_x greater than a critical momentum, k_c [17]. As the ribbon width decreases, the critical momentum k_c is shifted toward the M point from Γ (shown in Fig. 4.8 (b)). This point is defined from the TB model as

$$\begin{aligned} k_c &= \frac{2}{a_g}\arccos\left(\frac{W}{2(W+z)}\right) \\ z &= a_g\sqrt{3}/2 \end{aligned} \tag{4.3}$$

where a_g is the graphene lattice constant and W is the width of the ZZ ribbon [17]. Note that if W >>z, k_c occurs at $\frac{2\pi}{3}$, the K point (in reciprocal lattice units, 1/a_g). As W decreases, k_c moves toward higher k_x toward the 1D M point. The critical momentum is doubly significant because the location of the valence band maximum occurs close to this critical momentum in a TB model, $VB_x \approx k_c$ (see Fig. 1.3(d)) [17].

MDCs and characteristic π-band fits from the split region are shown in Fig. 4.8 (c). They demonstrate persistent splitting through energy up the facet cone. I calculated the TB-predicted k_c distribution based on the frequency of collected facet widths from STM (width distribution shown in Fig. 4.2 (c)). After convoluting the resulting data with a 0.05 $Å^{-}1$ window consistent with half the measured Lorentzian width, the frequency distribution closely reproduces the measured VB_x splitting in ARPES. The distribution is shown beneath the MDCs with a black line and the resulting peaks are indicated with dashed lines,

within 0.25 Å^{-1} of the stable π-band locations. This is consistent with the ribbon width distribution, $N(W_r)$, being equal to the facet width distribution, $N(w_{nf})$. Then the observed splitting in k_x of the 6H-ZZ facet cone at E$_B$ >-0.4 eV is indicative of a high frequency of narrow (W_r<5 nm) graphene ribbons.

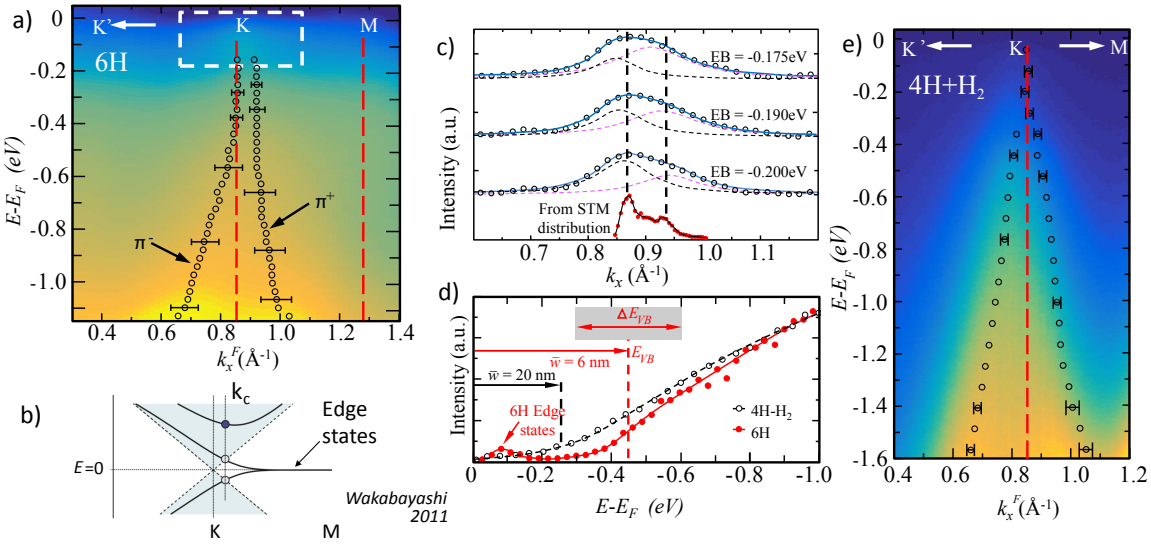

Figure 4.8: a) Cross section of $(11\bar{2}\ 22)_{6H}$ facet cone parallel to direction of trenches. Black circles mark locations of centers of Lorentzian curves used in MDC fits, note that the locations become stable in k_x at BE >-0.4 eV. b) TB approximation of ZZ-edge state from Ref. [17]. A dark blue circle marks the location of the shifted valence band minimum at VB$_x$ $\approx$ k_c. c) MDC curves taken from the splitting region, red data shows expected intensity based on STM ribbon width frequency distribution. d) EDC taken through center of cone on 6H and 4H facet cones shown in red and black, respectively. Expected E$_{VB}$ calculated from GW approximation indicated with arrows for 6 nm and 20 nm ribbons. e) ARPES cross section of 4H-ZZ-H$_2$ facet cone, circles mark location of Lorentzian centers fitting the π^+ and π^- bands.

In a GW approximation, the direct band gap, Δ^o, is a function of ribbon width. As shown in section 1.3.1, the GW approximation predicts that the gap is inversely related to

the ribbon width [5]. Using a many-body approximation, the band gap is found to be:

$$\Delta^{o}_{GW} = \frac{A}{W_r + \xi} \tag{4.4}$$

where A is an arbitrary constant, W_r is the ribbon width and ξ is an additional width accounting for soft boundary conditions present in a many-body calculation. Fitting the theoretically predicted $\Delta^{o}_{GW}(W_r)$ produced by Yang et. al., I find that ξ = 16 Å^{-1} and A$\sim$38 eVÅ.

Using the measured ensemble facet width distribution, $N(\overline{w}_{nf})$, with equation 4.4, the mean GW energy gap and broadening is calculated, $\bar{\Delta}^{o}$ = 0.897$\pm$0.24 eV. If we assume a neutrally charged ribbon, the top of the valence band would be approximately located at E^{max}_{VB} = -$\frac{1}{2}\Delta^{o}$ = -0.45 eV. E^{max}_{VB} closely corresponds to the inflection point at E_B = 0.4 eV in the integrated intensity of the facet cone π-bands, labeled in Fig. 4.8(d). The agreement with the GW approximation implies that the 6H-ZZ GNR is bonded intermittently along the sidewall forming very narrow ribbons. For comparison, I include the EDC taken through the 4H-ZZ-H_2 facet cone, E_{VB} = -0.2 eV, calculated for a wide ribbon in section 3.3.5.

Finally, the area averaging over many widths contributes to the π-band spreading in k_x. The width Δk^{F}_{x} of the bands near the inflection point (E_B = 0.45 eV) is 0.17Å^{-1}, approximately three times the width at lower binding energy. The broadening in the π-bands is partially due to sampling multiple subbands in energy originating from ribbons with many different widths. It is possible to approximate the broadening of the π-bands, Δk^{F}_{x}. I assume linear dispersion for the graphene π-bands. If the energy broadening is $\Delta E = \delta\Delta^{o}(W)$, then an estimate for the broadening in k can be derived using equation 4.4 as follows:

$$
\begin{aligned}
E = \hbar v_F k \implies \Delta k_x^F &= \frac{\Delta E}{\hbar v_F} \\
\Delta E = |\delta \Delta_{GW}^o| &= \frac{A}{(W_r + \xi)} \frac{\Delta \bar{w_F}}{(W_r + \xi)} \\
\Delta k_x^F &= \frac{\Delta_{GW}^o(\bar{w_F}) \Delta \bar{w_F}}{\hbar v_F (\bar{w_F} + \xi)}
\end{aligned}
\tag{4.5}
$$

where Δ_{GW}^o is defined by equation 4.4, v_F is the average band velocity of the two pi-bands, and ξ is 16 Å [18]. Using measured $\bar{w_F}$ and $\Delta\bar{w_F}$ from STM measurements, I find $\Delta k_x^F = 0.14$ Å^{-1}. This value is in good agreement with our experimental value of 0.17 Å (widths indicated in Fig. 4.7(b)), implying that the graphene ribbon width is proportional to the nano-facet width.

4.3.5 Probing the Electronic Structure with STM between the (0001) Nanoflats and Nanofacets

STM dI/dV measurements taken on 6H ZZ ribbons demonstrates that $(11\bar{2}\,22)_{6H}$ facets are electronically distinct from graphene on the $(0001)_{6H}$ flats. In STM, a negative bias voltage probes the filled states of the sample. Figure 4.9 (b) shows dI/dV measurements for several tip bias voltages. The fact that the $(11\bar{2}\,22)_{6H}$ facets are bright compared to the (0001) nanoterraces indicates that there is a discontinuity in the electronic structure of the graphene on the facet and graphene grown on the nanoterraces. From atomically resolved scans on the top edge, we know that the narrow ZZ-edge ribbons terminate into a semiconducting BL on the macroscopic (0001) surface through sp^2 bonds. At the bottom edge, the facet graphene can either terminate into the substrate (Type 1 ribbons shown in Fig. 4.9 (c)) or transition into a semiconductive form of graphene on the (0001) nanoterraces, like the graphene BL (Type 2 ribbons shown in Fig. 4.9 (d)). In either case, the free-standing portion of the ribbon is not continuous over the edge boundary. This is consistent with our results from area-averaged ARPES and topographical measurements that already suggest the ribbon width is proportional to the nano-facet widths.

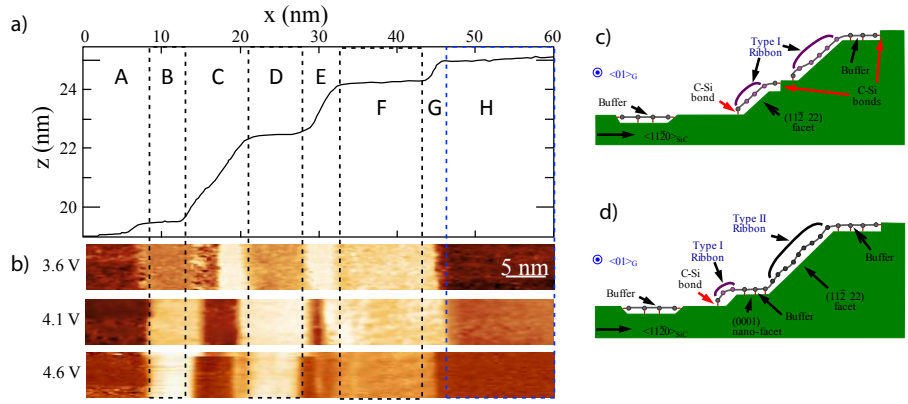

Figure 4.9: a) Line profile of a 6H ZZ ribbon with many flats along the sidewall. b) dI/dV images shown for varying STM bias voltage along scan in a). Black-dashed boxes indicate (0001) nano-flats where the LDOS varies between bias voltages and blue-dashed box indicates the main (0001) flat. c) Schematic of narrow graphene ribbons terminating into the substrate or d) into a BL-like interfacial epitaxial layer.

4.3.6 STM dI/dV between (0001) Nano-Flats and Main Flat

STM measurements also show that the (0001) nano-flats and large (0001) surfaces have distinct electronic structures. Figure 4.9 shows dI/dV measurements taken for various tip-bias voltages over an area represented by the line scan on top. The contrast on the primary (0001) flat, indicated by the letter H, is independent of the bias used. However, the narrow terraces, indicated by B, D, and F, change in relative contrast as the tip-bias changes. Figure 4.2(d) shows a current mapping of the main (0001) flat on the left, and the adjacent nano-flat on the right. The (6x6) periodicity is evident on the main flat, but not on the nano-flat. The voltage-dependent LDOS characteristics and lack of (6x6) periodicity show that the nano-flats have a different bonding structure than the graphene on the main (0001) flat.

This result is similar to that found for 4H-AC ribbons with nano-flats. Graphene grown on 4H-AC sidewall nano-flats has a smaller bonding distance than graphene grown on the main flat measured using TEM [72]. This has not been shown for graphene ribbons on 6H-ZZ samples because the sidewall graphene has not been observed in TEM [12]. However,

future structural work on 6H sidewalls is justified on 6H-ZZ ribbons because this is the first time that ARPES has measured Dirac cones originating from the facets. Unfortunately, it is difficult to measure energy states in ARPES originating from the (0001) nano-flats from either type of sample due to the overwhelming intensity from the graphene (0001) ML at the graphene K point.

4.4 6H-ZZ Sidewall Edge States

What differentiates ZZ-edge ribbons from AC ribbons is the existence of edge states. Because they are localized to the ribbon edges, their spectral weight is low. Nevertheless, we have been able to measure a narrow pair of flat energy bands close to the Fermi energy, named κ_1 and κ_2, that we verify as ZZ-edge states. They are shown in Fig. 4.10 (a). These measurements were taken at 100 K because at room temperature, thermal broadening (k_bT = 75 meV) is larger than the band separation, making it impossible to resolve these two states. At 100 K, the thermal broadening is approximately k_bT = 25 meV. We can clearly resolve the upper and lower non-dispersing states, located at E_B = 56 meV and 103 meV, with broadening of $\sim$58 meV.

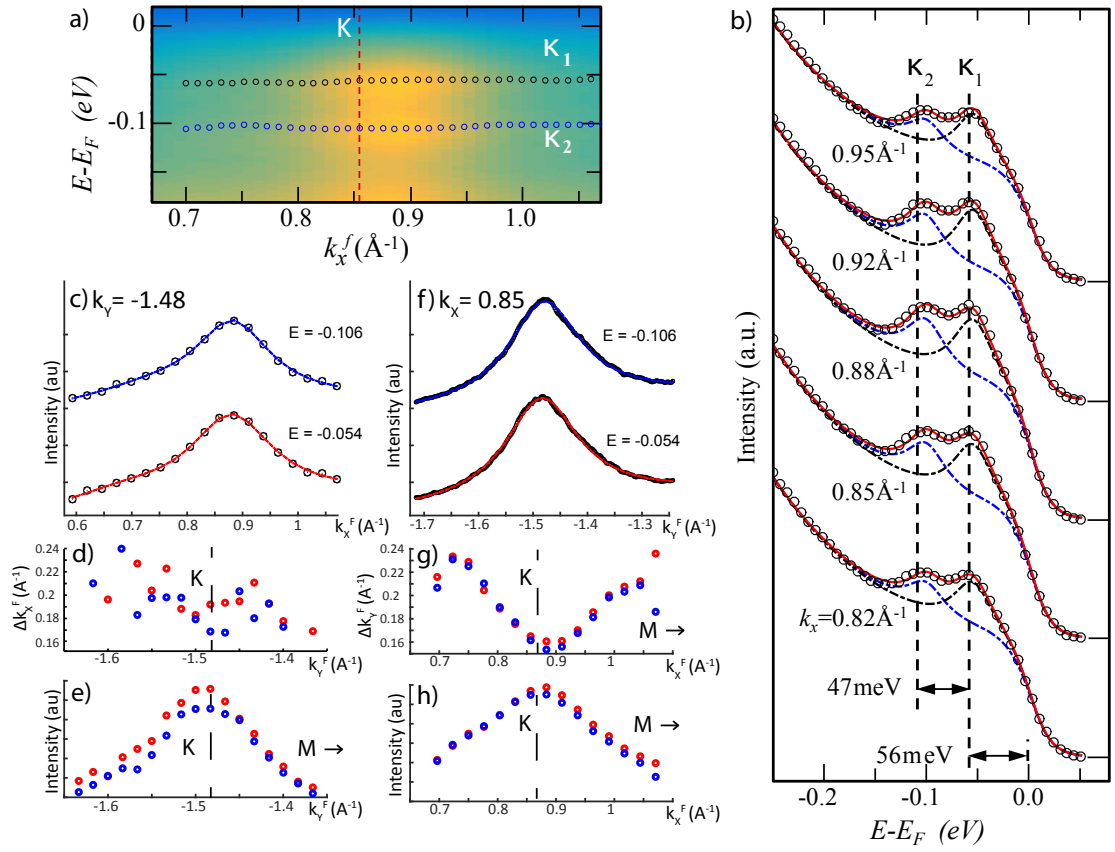

Figure 4.10: a) Log plot of ARPES intensity showing the two surface states at the facet K-point. k_y^F=1.48Å^{-1}, hν = 36 eV. Blue and black circles show the locations of κ_1 and κ_2 from EDC fitting. Average location: E-E$_F$ = (-0.056, -0.103) eV. b) Characteristic EDC fits for selected k_x^F, at k_y^F=1.48Å^{-1}. c) Lorentzian fit for an MDC cut parallel to the trenches, k_y^F= -1.48 Å^{-1}. d,e) Width (Δk_y) and integrated intensity of Lorentzian at each point in k_x. f) Lorentzian fit for a MDC cut perpendicular to the trenches, k_x^F= 0.85 Å^{-1}. g,h) Width (Δk_x) and integrated intensity of Lorentzian at each point in k_y^F.

4.4.1 6H-ZZ Edge State EDC Fitting Procedure

Multiple energy distribution curves (EDC) were fit (I(E$_B$) at fixed k_x^F and k_y^F), to analyze the edge states near the facet K-point. The GW approximation indicates that the location

of top of the valence band is inversely proportional to the ribbon width. Because many ribbons are sampled simultaneously in ARPES, the background is too complex to model. A general polynomial background represents the entire broadened diffuse intensity. Over the k_x^F span of the edge state, ± 0.1 Å^{-1} (shown in Fig. 4.10 (a-b)), this background changes in intensity but not in shape. The edge state EDCs were fit using Lorentzian curves that are free to move in E_B and change in width. The EDCs are averaged over 0.14 Å^{-1} in k_y for better counting statistics. They are narrow in energy, $\Delta E \approx 58$ meV, and have little to no dispersion in k_x^F or k_y^F. Figure 4.10 (a) shows the flat shape of the edge states on an ARPES cut through a constant k_y^F. Some characteristic EDC fits through the edge states at k_y^F = 1.48Å^{-1} for different values of k_x^F are shown in fig. 4.10 (b).

MDC curves are taken through the facet cone both perpendicular to and parallel to the ZZ-edge direction. MDC's are averaged over $\pm$ 0.15 eV to increase counting statistics. The states are each fit to a single Lorentzian curve with a linear background to account for diffuse background intensity. Characteristic fits and resulting Lorentzian data from fitting the parallel and perpendicular MDC's are shown in Fig. 4.10(c-e) and (f-h), respectively. The LSRA fitting parameters do not use any constraints because the edge state is the only feature in the vicinity of the facet K-point. The edge state width parallel to the direction of the trenches, Δk_x, appears independent of the position in k_y (see Fig. 4.10 (d)). MDC fitting at the center in E_B (56 and 103 meV) of each edge state provides an value for the k_x broadening, Δk_x^F = 0.19 $\pm$ 0.03Å^{-1}. This results in an estimate for the long-range order along the ribbon edges, L = $2\pi/\Delta k_x^F$ = 33.1 Å^{-1}. In contrast, Δk_y has a clear trend with k_x, increasing from K to M (see Fig. 4.10 (g)). The behavior of the edge state perpendicular to the directions of the trenches in discussed in section 4.4.2.

4.4.2 6H-ZZ Edge States Corroboration with TB Theory

The fact that these edge states do not disperse in k are predicted by ZZ-edge ribbon models with asymmetric terminations, as shown in Fig. 1.4 (d) [20]. While the symmetric

TB model is not expected to give an accurate description of the charge density for these asymmetric ribbons, we can expect a similar I(k_x^F) dependence as the wavefunction becomes more localized to the edge. TB models based on symmetric ZZ-edge terminations show that the density of states for each ZZ chain across a ribbon will have an intensity dependence of $D_k^{2(m-1)}$, where m is the index of the ZZ-pair from the ribbon edge and $D_k = -2\cos(ka_g/2)$ [17]. Then the intensity has the following relationship with k_x^F:

$$\begin{aligned} I \propto D_k^{2(m-1)} &= \left(2\cos(\frac{k_x^F a_g}{2})\right)^B \\ m &= \frac{2y_{eff}}{\sqrt{3}a_g} \\ B &:= \frac{4y_{eff}}{a_g\sqrt{3}} - 2 \end{aligned} \tag{4.6}$$

where k_x^F is the value of k in the direction parallel to the ribbons, a_g is the graphene lattice constant and y_{eff} is related to the perpendicular penetration length of the localized edge state. The value of D_k must be $<$1, or the density of states would diverge for a graphene sheet. The intensity of the flat edge state is maximized where D_k is maximized, at the graphene K-point. Then as k_x^F increases from K to X, the intensity decreases to zero. This is indeed the trend observed in the integrated intensity data shown in Fig. 4.11(b) with red circles.

Although the exact edge structure is unknown, I compare the measured 6H-ZZ edge state ARPES data to the TB analytical model. When fit to the functions in equation 4.6 using a LSRA fit procedure, the κ_1 and κ_2 bands correspond to B+2 = (3.97, 4.15), respectively. Within error bars, the edge states have the same decay from K to M. The average fit is shown with a black line in Fig. 4.11 (b). Because the wavefunction decays perpendicularly into the ribbon, the ARPES edge state is localized in y. We define a characteristic decay length, y_{eff}, to describe the broadening in k_y^F. Then the relationship between the

broadening, $\Delta k_y^F = 2\pi/y_{eff}$, as a function of k_x can be approximated from equation 4.6:

$$\begin{aligned} \ln(I/I_o) &= (\frac{2\frac{2\pi}{\Delta k_y^F}}{a_g\sqrt{3}})\ln(2\cos(\frac{k_x^F a_g}{2})) \\ \Delta k_y^F &= \frac{8\pi}{\sqrt{3}a_g(\frac{\ln(I/I_o)}{\ln(2\cos(\frac{k_x^F a_g}{2}))})} \end{aligned} \tag{4.7}$$

where I_o is D_k^2 and the other parameters are defined as above. This function shows that the broadening perpendicular to the ZZ-edge direction should increase from K<k_x^F<M. The experimental edge state width (Δk_y^F) perpendicular to the trenches is shown in Fig. 4.11 (c). The trend is in agreement with the expected behavior. A LSRA fitting is shown with the black line mirrored across the K-point, I/I_o = 2E-8. Since the broadening is increased by edge disorder and instrument effects, Δk_y^F has been convoluted with a .16 Å^{-1} window consistent with the experimental minimum.

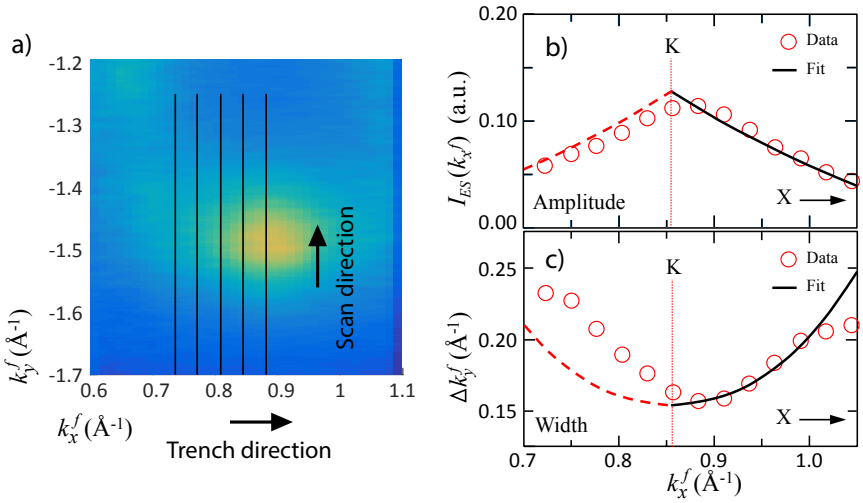

Figure 4.11: Data from the MDC edge state fitting procedure described in text. a) FS taken at E_B= -0.01 eV, corresponding to the lower edge state, κ_2. hν=36 eV. Black lines indicate the scan direction across the edge state. b) Integrated intensity of MDC fits taken parallel to the lines in a), theoretical prediction from a ZZ-edge TB-model shown in black. c) Width of Lorentzian MDC fits taken parallel to the lines in a), the black line is a theoretical result from a TB-model. Theoretical prediction is mirrored across the facet K-point in red dotted line.

4.4.3 Contradictions between 6H-ZZ Band Structure and Theory

I have corroborated my experimental data with the expected k_x^F locations of the π-bands and the perpendicular intensity dependence for a symmetric TB model [5, 17]. However, there are significant differences between the stated model and the measured data. First, the edge states κ_1 and κ_2 are narrow in energy, a feature that is not predicted using the TB model. The area averaging of ARPES simultaneously measures subbands from all ribbons in the relatively large spot size, so it is granted that a variety of ribbon widths are encapsulated in the measurement. This suggests that the edge states width in energy should be proportional to the distribution of ribbon widths, $N(W_r)$. From the width distribution, this corresponds to $\Delta E \approx$ .49 eV, 9 times the experimental broadening.

Secondly, symmetric tight binding models also predict strong band dispersion in k, regardless of whether the edges are aligned ferromagnetically or antiferromagnetically (discussed in section 1.3.1) [18, 5, 88, 89, 90]. A symmetrically terminated ZZ-edge band structure with strong dispersion in k_x is shown in figure 4.12 (a). The chosen model has H-bonding to terminate the dangling bonds along both ZZ edges [20]. On the other hand, ab initio calculations from asymmetrical edge geometries (one H-terminated edge and one H_2 terminated edge) produce nearly flat edge states, shown in Fig. 4.12 (b). The 6H-ZZ facets demonstrate very flat edge states in ARPES, reprinted in Fig. 4.12 (c). The observed flat bands are consistent with the ab initio calculations from asymmetrical edge geometries. While we cannot determine whether these ribbons are bonded into the substrate or into an (0001) BL, the edge state shape supports that the top and bottom boundaries are asymmetric. Then the wavefunctions are localized to the edge and produce the flat ZZ-edge states through the BZ [20].

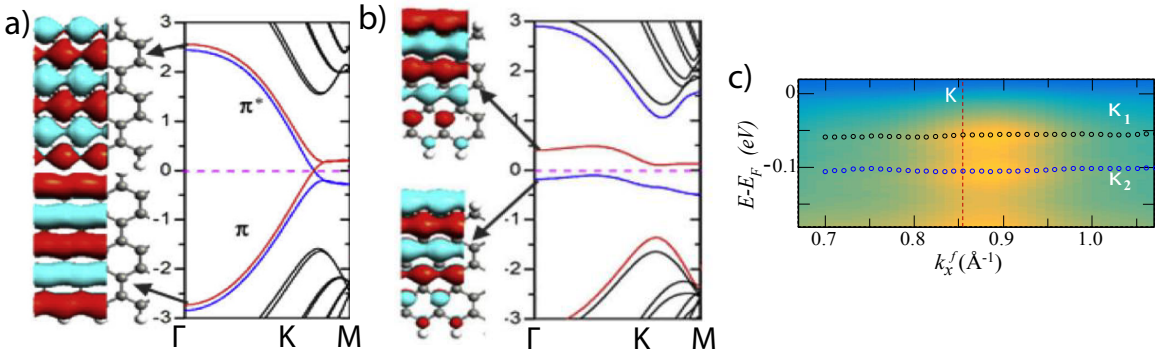

Figure 4.12: a) Left: Symmetrically terminated ribbon structure, wavefunction propagates through entire ribbon, N=5. Right: Band structure is similar to that for TB model with a degenerate edge state from K to M. b) Left: Localized wavefunction as a result of asymmetric terminations, N = 5. Right: Band structure reveals flat edge states spanning the entire BZ. From ref. [20]. c) Measured flat edge states in ARPES. hν = 36 eV.

4.4.4 Transport on 6H-ZZ Sidewall Ribbons

2-probe transport measurements were taken at Oak Ridge National Laboratory. Two different cryogenic four-probe scanning tunneling microscope (4P-STM) systems were utilized, one operated at 82 K and the other at 4.6 K. All measurements were conducted under UHV conditions (<10E-10 Torr). Because the graphene sidewall samples were exposed to the air after growth, they were cleaned prior to measurement by annealing in the UHV chamber at 300-500 C for a several hours before STM measurements. To measure two-probe resistance, R_{2P}, two STM tips were brought into contact with the same sidewall graphene ribbon and the resistance between the two probes was measured with a source-meter unit. STS was measured with a single probe in a tunneling configuration using a conventional lock-in technique to measure dI/dV spectra.

The 6H-ZZ samples demonstrate transport independent of length, characteristic of ballistic transport. This is shown on a log plot in Fig. 4.13(a), where the value of the resistance is approximately equal to the quantum resistance, $R_0 = h/e^2$. This is fundamentally different from the linearly dependent transport properties measured on the 4H-ZZ and 4H-ZZ-H_2 samples, shown for comparison in Fig. 4.13(a). Linear plots of these two samples with extracted sheet resistances are stated in chapter 3. STS measurements are shown in Fig. 4.13(b). The non-zero value at zero bias voltage indicate that the 6H-ZZ sample is metallic, like the 4H-ZZ-H_2 sample. While the peak locations in the dI/dV spectra change with position along the facet wall, 6H and 4H H-passivated ribbons are always metallic. STS shows that this 4H-ZZ sample has a bandgap of ∼0.15 eV. 4H-ZZ ribbons are not metallic, at least for wide trench sides. It is known that metallic ribbons form on shallow natural steps and it is impossible to isolate the sidewall ribbon transport from the potential contact made on the natural steps. Also, it is possible that graphene grown on shallow trenches interact with the substrate differently. When the trench depth is on the order of the ribbon radius of curvature (∼5 nm) the bonding pattern to the epitaxial graphene may be interrupted, allowing the ribbons to remain metallic.

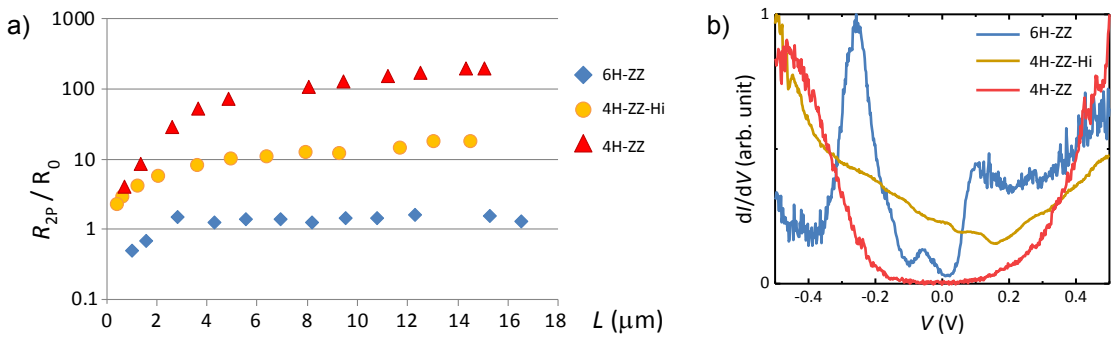

Figure 4.13: a) Log plot of resistance values verses length from 6H-ZZ sidewall nanoribbons, 4H-ZZ and 4H-ZZ-H_2 measurements included for comparison. Units of h/e^2. b) STS dI/dV measurements on all samples. Courtesy of Wonhee Ko at Oakridge National Laboratory.

4.4.5 Conclusion: Polytype Contrast and Selection

To summarize, while it has been the general assumption that selectively oriented GNR grow similarly on different polytypes of SiC, I have demonstrated definitively that this is not the case. The observation of 6H-ZZ edge states, the distorted π-bands and length independent resistance measurements show that ZZ ribbons grown on 6H-SiC are fundamentally distinct from similar ribbons on the 4H polytype. 4H-ZZ ribbons form graphene bound to the underlying substrate, only released via hydrogen intercalation. From an energetics point of view, the 6H-ZZ sidewall facet has a lower free energy than that for 4H-ZZ ribbons because it forms a stable structure without bonding to the released epitaxial layer. This is consistent with the lower polar free energy minimum for 6H-ZZ trenches shown in Fig. 2.9, though the demonstrated energy minimums are only reliable for annealed SiC without epitaxial graphene grown on top.

ARPES, STM and STS measurements show that 6H-ZZ sidewalls are composed of $(11\bar{2}\ \sim 22)_{6H}$-(0001) facet-flat pairs that are electonically isolated from each other. The resulting width distribution has 80% ribbon widths that are $<$12 nm long, 50% that are $<$3

nm. ARPES measurements show two observed edge states at E_B= 56 and 103 meV at the facet K-point. These edge state dispersion, width and intensity dependencies on in-plane momentum suggest they originate from asymmetrically terminated ZZ edges. Transport measurements show these ribbons behave as ballistic conductors up to at least 16 μm.

There may be edge states present on 4H-ZZ ribbons, but it is known that hydrogen intercalation p-dopes the graphene band structure [91, 8]. It is possible that the edge states are still there, but far enough above the Fermi level that even Cs *n*-doping cannot fill them for observation with ARPES. Thus far, the only band-measurements on GNR in ARPES producing these flat, narrow edge states are the ones described in this chapter, measured on 6H-ZZ sidewall ribbons.

CHAPTER 5
ALUMINUM OXIDE ON EPITAXIAL GRAPHENE

The epitaxially grown graphene BL on the SiC (0001) face has a natural bandgap from the complicated bonding structure to the underlying substrate (see section 2.3.3) [64, 47]. If a FET device was to be produced from this material, it would require a voltage gate on the gapped BL. Voltage gating via a deposited oxide insulator is a common method of gating graphene [92, 93]. However, there has not been any research done on the interaction of the BL with deposited films.

I have taken core level measurements at the Soleil synchrotron to show that ALD oxide interrupts the bonding structure of the semiconductive BL on the (0001) flat. There are also differences in the vibrational modes observed with Raman spectroscopy and the BL valence bands decrease in intensity in ARPES. All measurements support that the ALD AL_2O_3 partially decouples the BL from the substrate, changing its structural and electrical properties.

5.1 Motivating Studies of Oxide on the Epitaxial Buffer Layer

Gating the BL is of particular interest because it might be used to make a semiconductor-metal interface with the ML. ML channels provide conductive paths for current to take and the SiC substrate provides an ideal insulating packaging for a device architecture. The gapped BL valence band structure measured by ARPES is shown in Fig. 5.1 (a-b), and the conductive ML band structure is shown in (c). It is theoretically possible to create a defect-free ML-BL boundary via a growth cap, a fabrication method that selectively prevents graphene growth. Some capping materials are AlN or SiN [94, 95]. A continuous semiconductive BL is grown and selectively capped for preservation (see Fig. 5.1(d)). Then another growth process produces a metallic ML wherever there is no cap, creating a per-

fectly continuous metal-semiconductor interface (see Fig. 5.1 (e)). Figure 5.1(f) shows the energy level diagram for the resulting *p-n-p* junction. However, metal-based capping layers may have doping effects on the underlying graphene so they are not ideal gating materials.

Instead, organic compounds are considered less reactive with the graphene [96]. Aluminum oxide is one of the most commonly used gating materials on graphene [3, 97, 96]. While plasma-enhanced ALD is known to destroy thin epitaxial layers [98], it is generally assumed that the surface interaction from standard ALD processes is negligible. However, annealing the BL at a temperature of 500 C in a water vapor partial pressure has been shown to decouple the graphene BL from the underlying substrate [99]. While ALD occurs at a much lower temperature, T=250 C, it is still worth exploring whether the surface is altered from either the H_2O or TMA reactants.

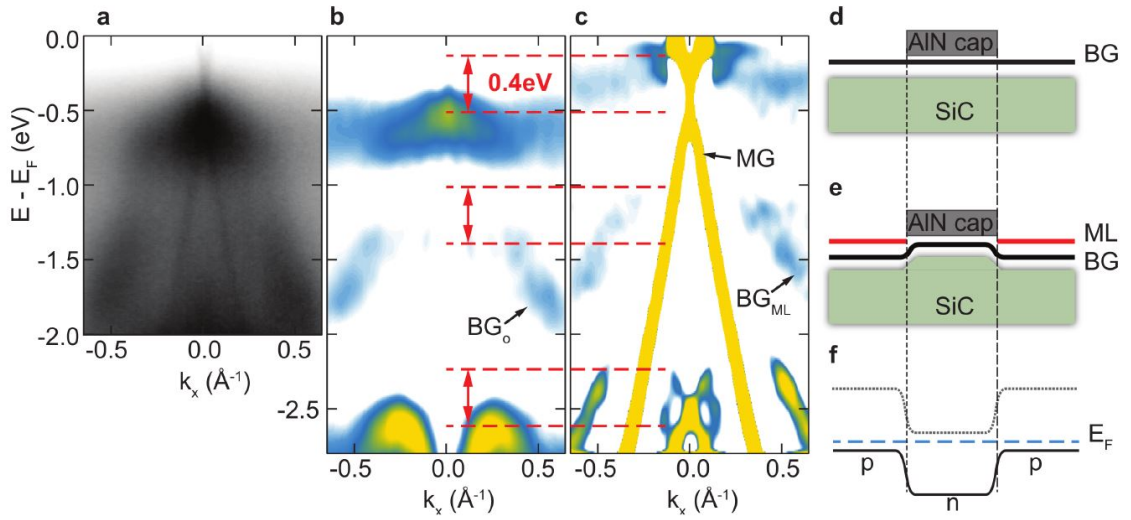

Figure 5.1: a) Valence level scan of the graphene BL. b) Negative second derivative of image in a), ML signal subtracted. c) Negative second derivate of the ML. d-f) Device fabrication and Fermi level diagram. AlN cap prevents further graphene growth, developed ML is bonded to semiconductive BL beneath cap.

5.2 Atomic Layer Deposition

5.2.1 ALD Process

Thin film oxides can be deposited using several different methods, including chemical vapor deposition, physical vapor deposition, thermal evaporation or atomic layer deposition (ALD). Allowing thin films of thermally evaporated aluminum to oxidize naturally in ambient room atmosphere is a common way of producing an oxide layer. However, this produces disordered or amorphous aluminum oxide with unpredictable crystalline and electronic characteristics. In addition, thermal evaporation requires high temperature target sources and does not produce uniform coverage on textured samples because the deposition is directional. In contrast, the characteristics of ALD Al_2O_3 should produce a structure comparable to Al_2O_3 bulk because it is grown layer-by-layer [100]. The comparative order and thickness control is why I chose to focus on ALD Al_2O_3.

Al_2O_3 is grown by alternating gas reactants in a chamber. There are oxygen-plasma assisted ALD methods, but it is known that oxygen processing degrades the epitaxial graphene layers [46, 101]. Using alternating water vapor (H_2O) and trimethylaluminum (TMA) is assumed not to interact with the graphene sheets. Initially, the first water vapor cycle oxidizes the surface of the substrate, then the growth is activated by the gases in the chamber meeting surface reactants. As a result, the growth is self-moderating. After the reactants have saturated the surface, the chamber is purged and flushed with an inert gas, such as nitrogen. This process is shown in Fig. 5.2. Approximately one bi-layer of Al_2O_3 grows per cycle [3]. The oxide thickness is then controlled by the number of cycles performed. Deposition order is generally improved with higher process temperature and shorter pulse times. The samples in this thesis were grown using a temperature of 250 C, processing details are included in Appendix B.

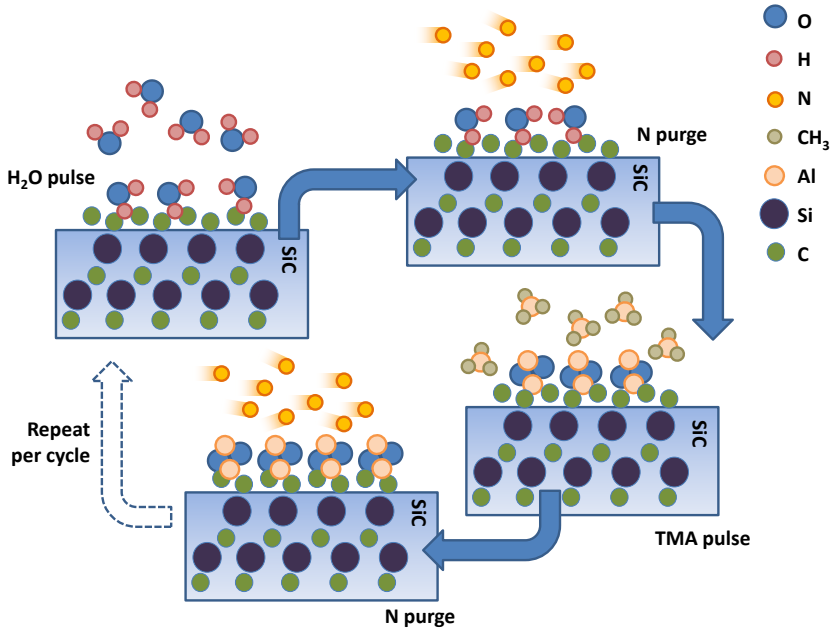

Figure 5.2: ALD schematic of Al_2O_3 by alternating H_2O and TMA, with intermittent N_2 purges. One full cycle is shown.

5.2.2 Characterization of ALD Al_2O_3 on BL, ML

ALD depositions on sp^2-bonded graphene have grown oxide layers. However lack of appropriate seeding sites makes oxide uniformity difficult to achieve [102, 103]. Conductive graphene sheets, ie. ML or cleaved HOPG, are generally nonreactive. Oxide depositions will only nucleate at step edges or near defects [104]. Common solutions to this structural problem involve seeding metals or polymers on the sample prior to the oxide deposition. Depending on the seed layer, different Al_2O_3 crystalline or amorphous structures are formed with varying dielectric constants [105, 106]. These seed layers are necessary in order to produce new nucleation sites in the interfacial bonding patterns between the graphene and seed layer. However, this can reduce the graphene mobility and conductance [92, 103, 93].

On the other hand, ALD depositions show much greater uniformity on the BL. It is known that the BL is more reactive than the ML due to more numerous nucleation sites

from the complicated hybridized bonding structure [3]. The BL also has less hydrophobic qualities than ML, allowing the H_2O molecules from the first ALD cycle to form bonds with the surface [100]. This could explain why the ALD process is so much more uniform on a BL sample, as ALD is initially activated by water vapor absorption.

NC-AFM imaging of ALD Al_2O_3 depositions on BL and ML graphene confirm that the oxide is more uniform on the BL. This is shown in Fig. 5.3. These AFM images were taken using non-contact AFM with an NCHR tip. The scan rate was 0.5 Hz at a set point of 1500 nm. X-ray reflectivity (XRR) measurements determine that the oxide thickness is t $\sim$9.5 nm. Despite that the depositions were made simultaneously on the two samples in the Cambridge Nanotech ALD system, the oxide on the BL sample is far more ordered. The deposition is very uniform across the buffer layer, the natural step edges on the (0001) flat are still discernible (see fig. 5.3 (a)). The surface roughness is determined using the RMS value over large terraces where distance between natural steps or defects is $\sim$.5 μm. For the BL, the RMS roughness value is 0.246 nm.

In contrast, the deposition on the ML sample is demonstrably nonuniform and oxide islands pool across the sample (see Fig. 5.3(c)). The ML oxide has a vertical RMS roughness value of 0.987 nm, four times that of the BL oxide. Considering that ALD deposits roughly 1.2 Å per cycle, reducing roughness is imperative for the improved quality of thin films [107]. This suggests that the BL is interacting with the surface reactants during the deposition, motivating an in-depth characterization of the electrical properties of the BL beneath the oxide gating layer.

The deposition on the BL has consistent RMS roughness values with those taken from evaporated Al_2O_3 coatings from reference [108]. Those samples showed a significant pinhole density, hundreds per square micron, even visible in the AFM scans. While we do not observe pinholes, it is likely that this oxide sample still has pinholes smaller than the resolution capability of the NC-AFM tip (radius $<$12 nm). These pinholes allow us to use ARPES to observe the band structure of the epitaxial graphene layer underneath the

deposition (see section 5.3).

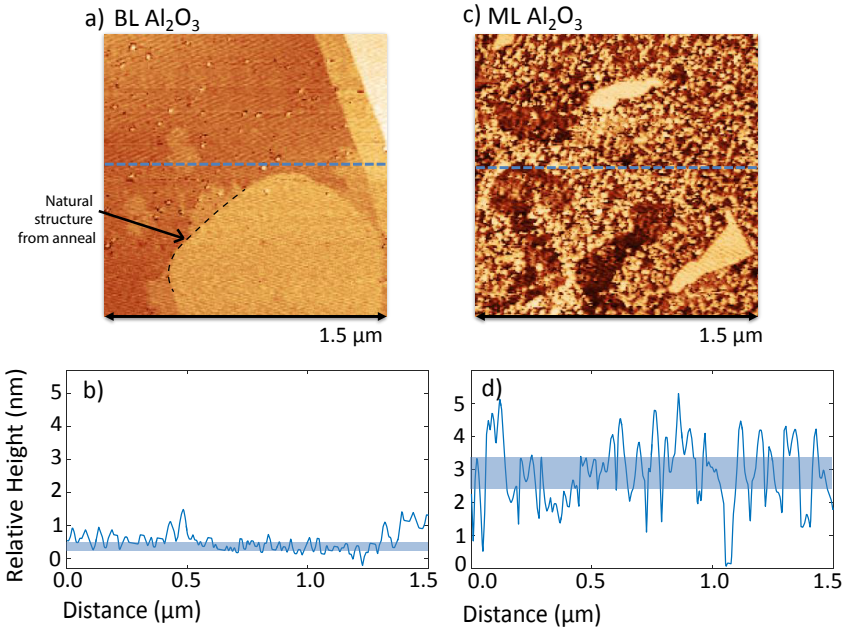

Figure 5.3: a) AFM image of ALD Al_2O_3 deposition on a BL sample. Some natural step edges are shown and a hexagonal feature that is a natural result of step flow during the annealing process. b) Line profile taken along the dotted line in a). The overall RMS roughness value is indicated using the light blue box. c) AFM image of ALD Al_2O_3 deposition on a ML sample. Some possible regions of undergrowth indicated. d) Line profile along dotted line in c). The RMS value is indicated in the blue shaded box.

Both the ML and BL samples demonstrate changes in the observed scattering modes in Raman spectroscopy after the Al_2O_3 deposition. Samples are measured using an incident wavelength of 532 nm in several spots across the sample to determine layer growth (described in section 2.6.6). The Raman spectra before and after Al_2O_3 ALD are shown in Fig. 5.4 (a) and (b). On the BL sample, a broad 2D peak associated with the ML appears after the oxide deposition. In addition, there is an increase in the intensity of the G peak relative to the buffer D+D' peak, also consistent with ML graphene. These characteristics indicate that oxide deposition on the BL produces more in-plane phonon excitations asso-

ciated with sp^2-bonded graphene. This may be attributed to the delamination of the BL into a psuedo-ML. It is not likely the result of intercalation by an ALD reactants because previous studies establish that higher temperatures ($\sim$500 C) are required for H_2O intercalation processes [99]. Further characterization of this sample requires measuring the surface properties with a high energy photon source to investigate its core levels before and after the oxide deposition.

The ML sample is also altered after the oxide deposition. The G peak increases in width by 10% (from 8.9 cm^{-1} to 9.8 cm^{-1}). Because the G peak is associated with in-plane optical phonons [80], this indicates a reduction in the long-distance order due to the oxide, even on typically non-reactive sp^2-bonded graphene materials. The Raman signal from 1400 to 1700 cm^{-1} is characterized by 2 Lorentzian line-shapes, one broad Lorentzian for the D-peak and a narrow Lorentzian for the G-peak. The peaks appear at the expected location for epitaxially grown graphene, the G-peak is at 1590 cm^{-1}. Changes in the ML graphene spectrum have been reported previously, but only for ozone-based ALD methods which actively functionalize the substrate during deposition [109, 110]. Further research is required to determine the impact gating materials have on the conductive properties of the ML, my extended analysis has only been performed on the graphene BL.

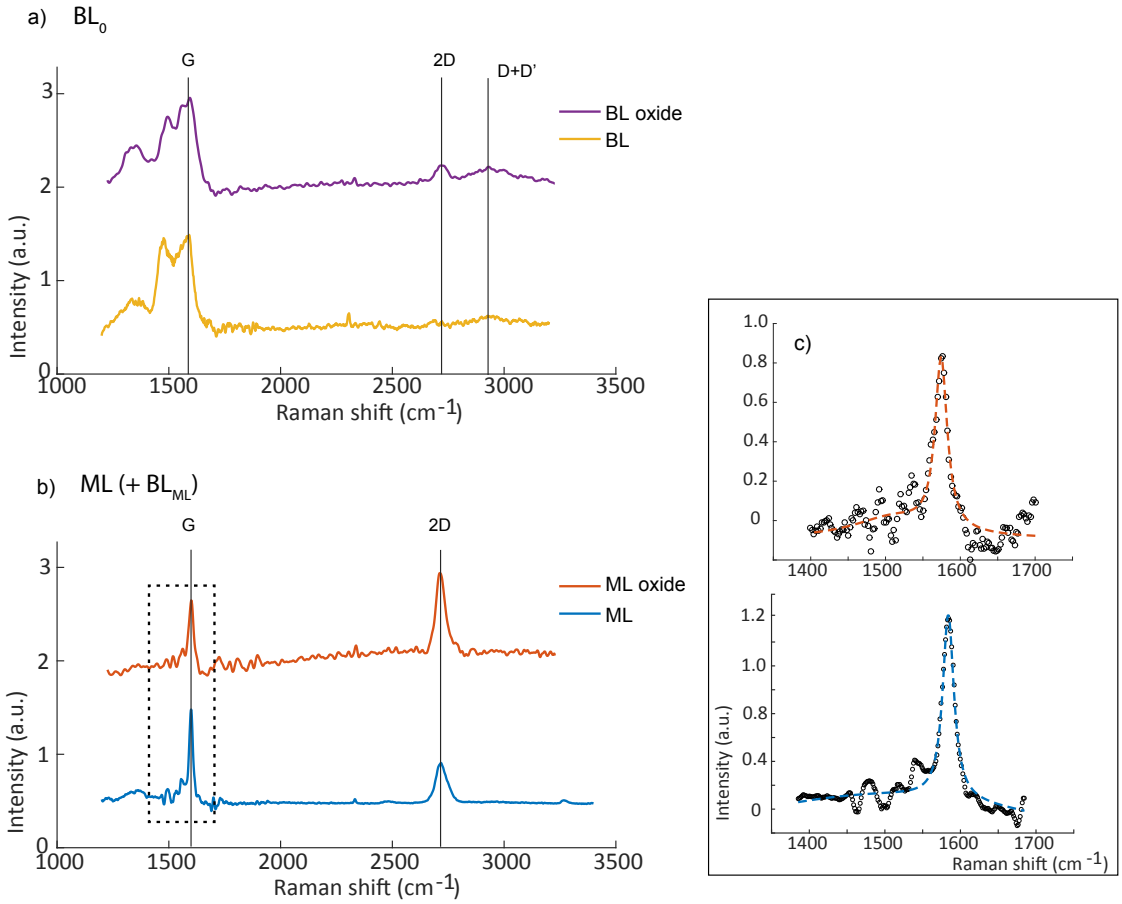

Figure 5.4: a) Raman spectra on the BL, pre- and post-oxide deposition. The characteristic graphene Raman peaks are indicated. b) Raman spectra on ML, pre- and post-oxide deposition. c) Inset from b) shows the Lorentzian fit to the G peak before and after the oxide.

To be entirely comprehensive, we must consider that these post-oxide Raman signals could be related to carbon oxide contaminants that are known to stick to the surface of insulating deposits, also called adventitious carbon [111]. It is unlikely that disordered surface contaminants would produce Raman signatures at the expected peak locations for graphene. In addition, the BL and ML Raman spectra are affected differently by the deposition, meaning that they would produce distinct contaminants during the same ALD process.

Overall, these Raman results in combination with AFM imaging are stronger evidence that a fundamental structural change occurs to the underlying BL sample.

5.3 Core Level Characterization of ALD Al_2O_3 on BL

Further characterization of these samples was performed with ARPES at the Soleil synchrotron. The loading chamber at the Casiopee beamline allows for annealing to remove any confounding surface contaminants, such as adventitious carbon. Before being measured in the ARPES beamline, the samples were heated to 500 C in UHV. There is little research on the topic of annealing the gating materials on epitaxial graphene, but it is commonly done for device fabrication to increase interface order and is considered fundamental to the development of stacked structures [112]. Previous work has shown that annealing to this temperature does not change the structure of the oxide deposition [113]. The observed changes in the core level scans are therefore independent of the low-temperature annealing performed to remove surface carbon contaminants.

5.3.1 Oxide Coverage Determination

The integrated intensities of the core levels produce an estimate for the percent coverage on the BL sample. The mean free path of the incident photons is on the order of centimeters [114], much greater than the height of the oxide. The number of excited photoelectrons from the substrate is therefore independent of the deposition. However, the emitted photoelectrons are heavily attenuated by the overlying oxide, greatly reducing the electron flux. Photoelectrons also leave the surface through pinholes in the oxide layer. If Θ_{ox} is the areal coverage of the ALD oxide layer, the area of pinhole coverage is given by (1-Θ_{ox}). Figure 5.5 shows the origin of each component of the C1s core level for a ML sample. The SiC core level intensity should be independent of surface interactions with the deposited oxide. Therefore, the comparison of the intensity of the SiC C1s core levels before and after the

deposition provides an accurate estimate of surface coverage as follows:

$$
\begin{aligned}
I_{SiC,total} &= (1-\Theta_{ox})I_{SiC,bare} + \Theta_{ox}I_{SiC,ox} \\
I_{SiC,ox} &= I_{SiC,bare}e^{-\frac{t_{ox}}{\mathrm{MFP}_{ox}}} \\
I_{SiC,ox} &= (1-\Theta_{ox})I_{SiC,bare} + \Theta_{ox}I_{SiC,bare}e^{-\frac{t_{ox}}{\mathrm{MFP}_{ox}}} \\
\Theta_{ox} &= \frac{\frac{I_{ox}}{I_{bare}} - 1}{e^{-\frac{t_{ox}}{\mathrm{MFP}_{ox}}} - 1}
\end{aligned}
\tag{5.1}
$$

where Θ_{ox} is the areal percent oxide coverage, I is the integrated intensity in counts of the SiC core levels, t_{ox} is the oxide thickness (95 Å) and MFP_{ox} is the mean free path of Al_2O_3. The inelastic MFP_{ox} depends on the electron energy after it is scattered. For a kinetic energy of 320 eV, the MFP is calculated to be 11.4 Å [115]. It is worth noting that for any oxide thickness more than twice the mean free path of Al_2O_3, the exponential term rapidly approaches zero. From this equation, the total oxide coverage on the BL sample was calculated to be 96.6%.

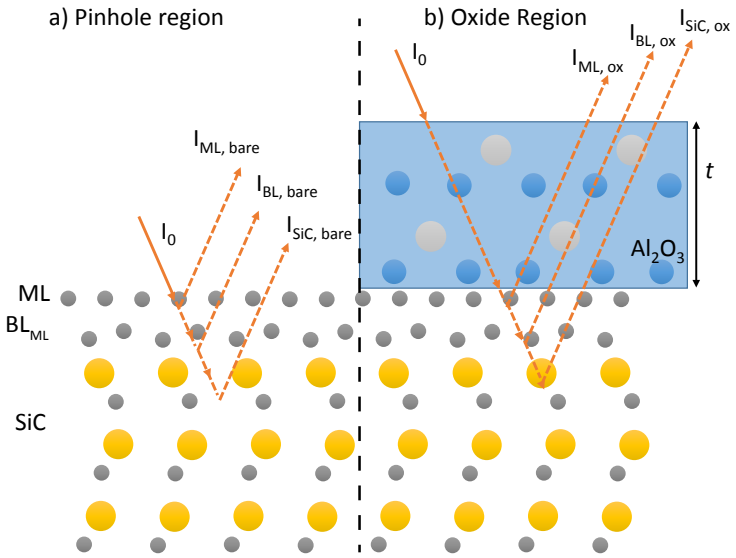

Figure 5.5: Schematic of the origin of the electron flux and attenuation layers from a ML sample with an Al_2O_3 oxide layer on top. a) Pinhole region, bare surface. b) Oxide region, each component of the C1s core level is attenuated by the oxide.

Because our deposition is ∼9 times the mean free path length of the photoelectrons, it is unlikely that we observe any photoelectrons from underneath the oxide layer ($e^{-\frac{t_{ox}}{\mathrm{MFP}_{ox}}} \approx 1.2$ E-4). It is reasonable to assume that all the observed signal originated from pinholes in the Al_2O_3 deposition, as discussed in section 5.2.2. Previous studies have found that typical pinholes are nanometers wide and occur with densities of a ∼100 per μm^2 [116, 117]. It might be argued that the pinholes preferentially form on the ML, changing the observed shape of the core levels and the intensity of the ML valence bands. However, XPS characterization of the core levels show that the pinholes do not form over ML overgrowth on the BL sample, as I will discuss in section 5.3.2.

5.3.2 Core Level Shapes and Fitting

Previous research has been completed in the characterization of the BL and ML core level components. The core-level scans on the bare sample are fit to the 5 characteristic peaks, 2 for the SiC core carbon levels, C_B and C'_B, and three buffer features, S_1, S_2 and S_g (as shown in section 2.6.5, Fig. 2.14 (a)). These peaks have established locations, widths and line shapes characterized by a parameter sweep of electron energies close to the Bragg angle [47, 53]. The Bragg angle is a function of both the incident photon energy and angle. The BL and ML core level yields change rapidly through this location in reciprocal space. The function describing a BL core spectrum is given by:

$$\begin{aligned} I(E_B) =& I_{Voigt,S1} + I_{Voigt,S2} + I_{Voigt,Sg} + I_{Voigt,Cb} + I_{Voigt,Cb'} \\ I_{voigt} =& p_L I_{Lor} + (1 - p_L) I_{Gauss} \\ I_{Lor}(E_B, \Delta L, h) =& \frac{h}{(\frac{E-E_B}{\Delta L})^2 + 1} \\ I_{Gauss}(E_B, \Delta G, h) =& h e^{-\frac{(E-E_B)^2}{2(\Delta G)^2}} \end{aligned} \tag{5.2}$$

where p_L is the percent Lorentz, ΔG and ΔL are the Gaussian and Lorentzian widths, respectively, and E_B is the center of each core level psuedo-Voigt peak. The locations, widths and percent Lorentzian values of the psuedo-Voigt functions are shown in Table 5.1. The peak location, ΔE_{C_B}, is given with respect to that of the bulk SiC C_B peak, E_{C_B} = -283.83 eV [53]. These parameters are constant with respect to electron energy, but the intensities depend on the penetration depth. Increased incident photon energy produces photoelectrons with higher kinetic energies that can propagate further through the substrate. Increased emission of photoelectrons from the bulk results in an increase in SiC C1s core level yields (C_B and $C_{B'}$) as opposed to the BL/ML epilayer core levels, but does not vary the shape of the C1s components.

Table 5.1: Parameters used for core level fitting from XRD fittings, determined by previous work in ref. [47].

	ΔE_{C_B}	ΔG	ΔL	p_L
S_2	-2.020	0.656	1.093	0.342
S_1	-1.519	0.899	0.022	0.002
S_g	-0.979	1.202	0.300	0.000
C_B'	-0.210	0.701	0.351	0.307
C_B	0	0.488	0.248	0.145

After the oxide deposition, the most notable difference is a large increase in the S_g core level and decreased yield from the S_1 and S_2 BL core levels. The BL core level intensities were determined with an LSRA fitting routine and eqn. 5.2. The area of each component is normalized with respect to the integrated intensity of C_B+$C_{B'}$ because surface interactions between the BL and the oxide should have no effect on the SiC bulk C1s levels. The normalized integrated areas of each component before and after the Al_2O_3 deposition are summarized in table 5.2. After oxide deposition, the normalized core level scans demonstrate a 288% increase in the BL S_g core level. The increase in the S_g peak is accompanied

with a decrease in the intensity of the BL S_1 and S_2 peaks by 10% and 26%, respectively. The resulting fits and component peaks are shown in Fig. 5.6 (a-b).

Table 5.2: Integrated intensity of each core level determined from LSRA core level fitting, before and after oxide deposition. Areas are given in normalized arbitrary units (normalized area by C_B+C'_B integrated area for direct comparison, raw data given in App. B).

	Bare	Al_2O_3	$\frac{S_{Al2O3}-S_{bare}}{S_{bare}}$
S_2	0.73	0.65	-0.10
S_1	1.22	0.91	-0.26
S_g	0.25	0.97	2.88
C_B'	0.56	0.56	0.00
C_B	0.43	0.44	0.00

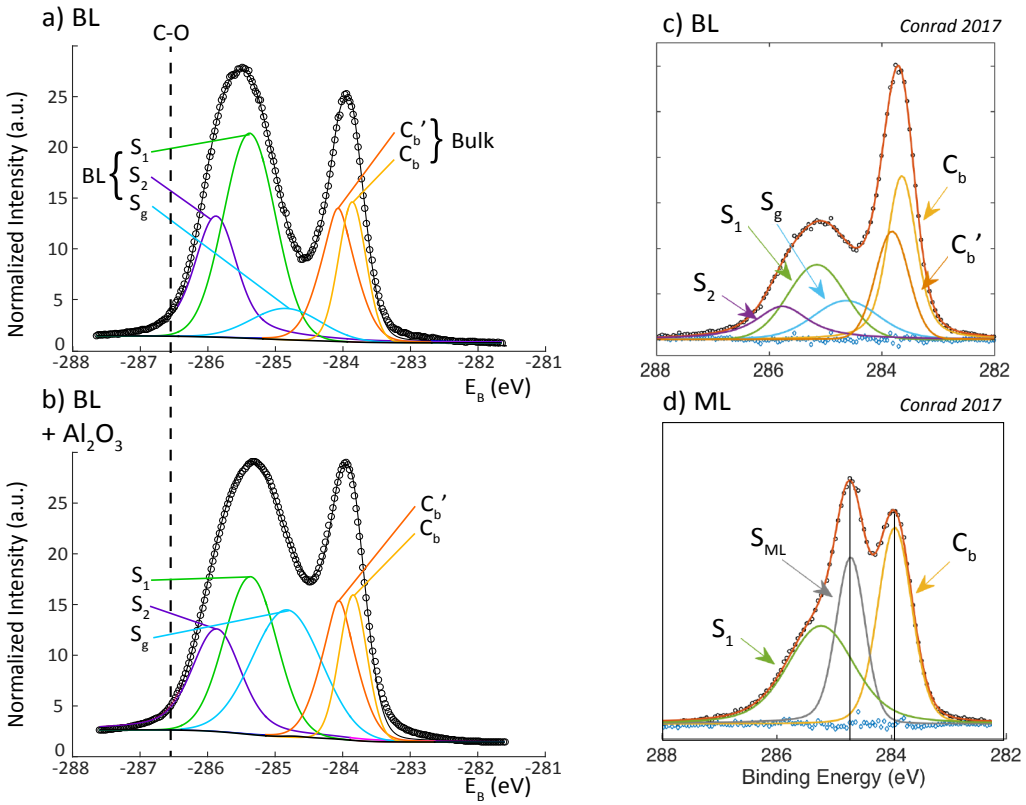

Figure 5.6: a) Bare buffer core level scan fit to 5 components. The blue components are from Si-C bonds in the substrate and the S components are associated with the BL. b) The same sample after an aluminum oxide deposition. The count rates have been normalized to oxide coverage. The expected location of a carbon-oxygen core level is indicated with a dashed line. hν = 600 eV c) A characteristic BL C1s spectrum from ref. [53]. d) A typical ML C1s spectrum for comparison from ref. [53], location of ML peak and SiC C1s peaks indicated. hν = 2513 eV

Examining the locations of the initial core level components confirms that the sample is primarily BL graphene. It would be incorrect to state that the increase in S_g is due to the BL becoming a quasi-freestanding ML or that the pinholes preferentially nucleate at ML overgrowth on the surface. While the S_g core level and the S_{ML} core level occur at very similar bonding energies (E_{Sg} - E_{ML} = .22 eV, E_{ML} = 284.58 eV), their respective widths and yields are very different. Characteristic BL and ML C1s spectra are shown in Fig. 5.6

(c-d). These spectra have a much greater bulk core level (C_B+C'_B) yield because they have been taken at a greater incident photon energy, hν=2513, but the core level shapes should be consistent with our lower energy measurements. The S_g peak is approximately two-times the width of the S_{ML} core level, 1.20:0.57 eV respectively. Since S_g only accounts for 35% of the buffer core structure, the ML core level yield is necessarily much greater for a full ML sample [47]. Even partial ML overgrowth can be detected using XPS integrated intensities. This sample does not have a significant amount of ML on the surface before or after the ALD oxide deposition ($<$3%, according to Raman measurements). In addition, ML graphene has a large S_1 core level component. If pinholes in the Al_2O_3 layer preferentially formed over ML overgrowth on the sample, the ML peak in the C1s spectrum would be much more pronounced after the deposition and you would expect to see a proportional increase in the intensity of the S_1 peak with the ML peak. Instead, there is no evidence of the ML peak in the C1s scan either before or after the oxide deposition and S_1 *decreases*.

Understanding the origins of the BL C1s components helps illustrate how the substrate-BL bonding structure changed with the addition of the ALD oxide layer. Figure 5.7 (a) shows the different theoretical C-C bonding structures for each core level associated with the BL. S_g is from sp^2-bonding between adjacent carbon atoms, similar to the ML bonding structure. The S_1 core level is associated with sp^3-bonding to the substrate and the S_2 bonding level is a hybrid mixture of sp^3- and sp^2- bond types. Ab initio calculations by Conrad et. al. suggest that the modulated BL lattice forms sp^2-bonded graphene 'islands', bordered by strong covalent bonds into the substrate [64]. Figure 5.7 (b) shows a graphene island and its bound borders. This geometry predicts the semiconductive BL band structure observed in ARPES (shown in Fig. 5.1 (a-b)). The change in the core level intensities suggests that the oxide destroys some of the substrate-BL bonding and results in a higher frequency of in-plane sp^2-bonding between adjacent carbon atoms. This would result in more ML-like metallic graphene islands across the sample, potentially destroying the semiconductive character. It should be mentioned that there is no evidence of C-O peak

in the C1s spectrum (location indicated in Fig. 5.6), so the BL is not forming new covalent bonds to the oxide.

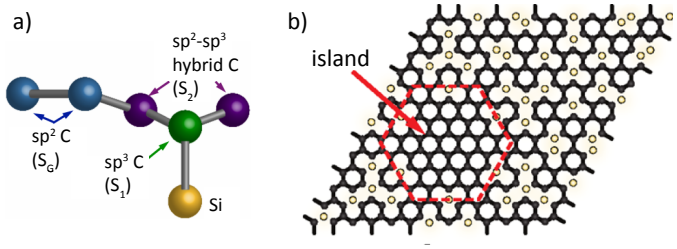

Figure 5.7: a) Schematic model of the origins of each BL core level component from sp^3- and sp^2-bonds. From reference [47]. b) Island structure for ab initio calculations in reference [64].

5.4 Valence Level Characterization of ALD Al_2O_3 on BL

While the core levels demonstrate that the oxide causes a structural change in the BL, analysis of the valence level scans demonstrate that the electrical character of the BL becomes more ML-like due to the Al_2O_3 deposition. The energy bands of the BL significantly decrease after the oxide deposition and the normalized intensity for the ML π-bands increases by a factor of 260%, similar to the 288% increase observed in S_g core level. These results confirm that along with significant changes to the BL C1s core levels, the electrical character of the BL is destroyed after an ALD oxide deposition. EDCs and MDCs were taken at the graphene K-point to characterize the electrical properties of the BL sample before and after the oxide deposition.

5.4.1 Buffer Bands Destruction post-deposition

ARPES scans at the graphene K-point before and after the AL_2O_3 deposition are shown in Fig. 5.8 (a-b). It is clear that the intensity from the BL ϵ_2 band is nearly destroyed after the oxide deposition. EDCs were taken near the graphene K-point in order to quantify the reduction in the BL valence bands. There are inherent difficulties in characterizing the

valence level energy bands because of the oxide. The Al_2O_3 serves its functional purpose as a wide-bandgap insulator. There is very high intensity from an oxide subband at $E_B \sim$ -3.5 V, completely obfuscating the ARPES intensity below that value. This energy corresponds to the experimental aluminum oxide bandgap from reference [118]. The valence level features above the AL_2O_3 cutoff are still visible in the EDCs.

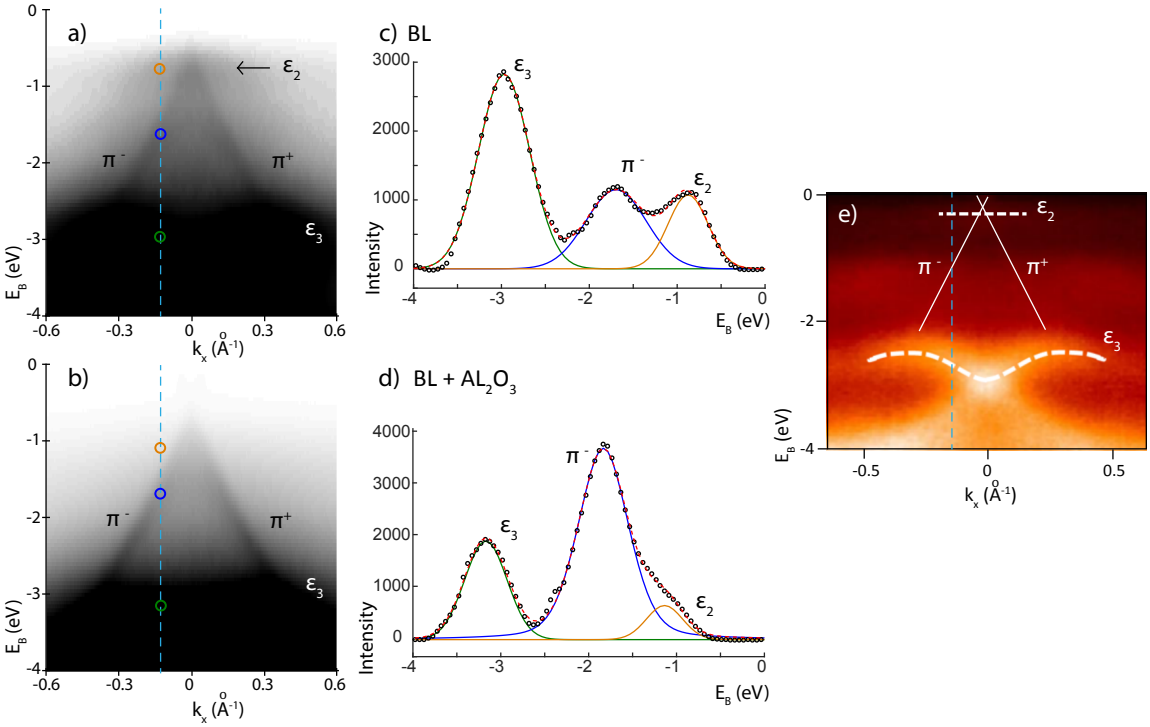

Figure 5.8: a) A log-intensity ARPES cross section through the bare sample K point. b) A log-intensity ARPES cross section of the same sample's K-point post oxide deposition. Lower energy bands (E_B ¡ 3.5 eV) cannot be seen because of the AL_2O_3 deposition. c,d) EDCs at k_x^o=-.155 Å^{-1} taken from the blue dashed lines in a),b) respectively. The location of the BL ϵ_2- and ϵ_3-bands and the π^--band indicated. Background subtracted. e) An ARPES image of a bare BL, the bands associated with the BL are shown in white dashed lines, the ML π-bands are indicated. Figure from reference [34].

There are three features in the EDC scans. Two bands associated with the buffer layer,

the ϵ_2- and ϵ_3-bands, and the ML π-bands. The expected locations of these features in shown in Fig. 5.8 (e) [34]. Each band is described in the LSRA fitting using an unconstrained Gaussian curve. The shape of the intensity from the superposed oxide valence band and underlying SiC and graphene subbands is not well-defined. I used a constant polynomial function to describe the complex background. It was allowed to change in amplitude. Figure 5.8 (c) and (d) show the LSRA fitting for EDCs at k_x^o = -0.155 Å^{-1}, where the bands are well separated. The polynomial background has been subtracted from the data set to emphasize the locations and relative intensity of the bands. The ARPES intensity of the post-oxide deposition is increased in proportion to the pinhole coverage (based on the 96.6% oxide estimate), then the normalized integrated intensities can be directly compared (shown in Tab. 5.3).

Table 5.3: Integrated intensity of each valence level band determined from LSRA core level fitting, before and after oxide deposition. Areas are given in ARPES count rates normalized to account for 96.6% oxide coverage.

	Bare	Al_2O_3	$\frac{I_{Al2O3}-I_{bare}}{I_{bare}}$
ϵ_3	1601	1163	-0.27
ϵ_2	710	341	-0.52
π^-	819	2960	2.61

After the oxide deposition, the π-band intensity increases by 260%, comparable to the change measured in S_g in the core level bands. It is unsurprising that S_g-bonding is associated with more ML-like electrical properties because the S_g-bonds correspond to the sp^2 bonding in the BL. The semiconductive ϵ_2- band decreases in intensity by 52%. This demonstrates that when the ALD Al_2O_3 deposition interferes with the BL bonding structure as shown in the C1s core levels, the semiconductive qualities of the epilayer is partially destroyed. This is consistent with the oxide converting the carbon to some kind of conductive layer, electronically similar to ML graphene.

Finally, the π bands are *n*-doped due to substrate interactions even after the oxide deposition, $E_D \sim 0.5$ eV. This is unlike previous studies demonstrating that oxygen processing electronically passivates the BL [46]. In that study, the sample was annealed in an oxygen rich environment causing the O_2 to intercalate between the BL and substrate. The process produced a charge-neutral Dirac cone ($E_D = E_F$), similarly to H_2-intercalation. If the gating oxide delaminated the BL carbon into a quasi-freestanding ML, we would expect to see both an increase in the π-band intensity and a reduction in the interaction-based *n*-doping. Instead, the persistent *n*-doping of the π-bands supports that BL only partially delaminates due to the overlying oxide and interacts with the substrate underneath, rather than the oxide intercalating through the interface.

5.4.2 π-band Intensity Increase Post-Deposition

Comparing the π-band count rates in the MDC scans is more reliable for E_B above 1 eV. At lower binding energy, there is no changing background in the ARPES signal to complicate analysis. The broad, flat ϵ_2 band is parallel to the MDC and is subtracted away as a flat offset in the background. I fit the MDC data using a broad Lorentz shape for a diffuse instrument background and two pseudo-Voigt functions to capture the ML band signal, as defined below.

$$I(k_x) = I_{Voigt,\pi+} + I_{Voigt,\pi-} + I_{Lor,back} + \Delta_{off} \tag{5.3}$$

where the psuedo-Voigt and Lorentzian functions were defined in equation 5.2 and Δ_{off} is a direct numerical offset.

The valence bands are fit above the Dirac point to directly compare count rates from the bare sample to the oxide sample. Two such fits are shown in Fig. 5.9 (a) for $E_B = 0.2$ eV. If there was no effect on the monolayer from the ALD process, it is expected that count rates would reduce proportionally to oxide coverage since virtually all photoelectrons produced

beneath the oxide are attenuated. When the data is plotted and the oxide scale corrected for the 96.6% oxide coverage, the normalized integrated intensity of the π-bands are shown to be 3.6 times larger than that of the bare sample. This is consistent with the monolayer coverage increasing by 260% after oxide deposition in agreement with the measurements produced from the EDC fitting, indicating that the BL interactions with the oxide produce a ML-like graphene electronic structure. This is consistent with a partial delamination of the BL during the ALD Al_2O_3 deposition.

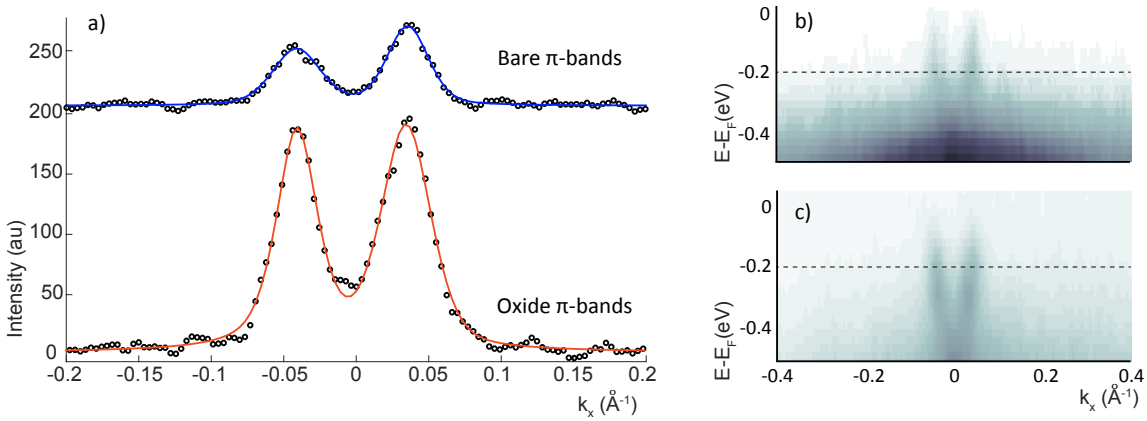

Figure 5.9: a) Line scans pass through the K-point on the bare sample (blue fit) and the oxide sample (orange fit), the relative intensity has been normalized by both scan number and oxide coverage. Black circles show the raw data. b) and c) Valence scans through k_x of the sample before and after the oxide deposition, respectively. Dashed lines indicate origin of line scans in a).

5.5 Conclusion

It has been assumed that an ALD Al_2O_3 deposition is a passive process on graphene, but the BL is an extremely reactive epilayer. XPS measurements of the C1s core level and ARPES scans of the valence level show that the oxide interferes with both the physical and electronic structure of the BL. The BL C1s core levels show a 288% increase in the intensity

of the S_g core level, associated with the sp^2-bonded component of the BL structure. In combination with the 260% increase in ML π-band count rates, it supports the theory that the oxide interacts with the BL in such a way that some of the carbon layer is delaminated. The semiconductive valence band intensity decreases by 40%, so using the oxide as a gating layer for graphitic devices is not a reasonable application.

Further research should still be completed on oxides on top of the graphene BL and ML. The existing literature would greatly benefit from transport studies across the interface which could further confirm our structural conclusions. Previous work has been done on exfoliated graphene flakes demonstrating that optical phonon modes may be excited in the deposited oxide, reducing the mobility of the metallic flake [119]. If such limits are also effective on epitaxial layers, this work would be fundamental to the understanding of mobility limits in graphene-FET devices.

CHAPTER 6
CONCLUSION AND FUTURE OUTLOOK

In this dissertation, I explore the electronic characteristics of graphene grown epitaxially on SiC for future applications in graphene-based electronics. There are many benefits to this growth method, including lack of the need for physical transfer, simple edge-selection for ribbons, and the slow growth rate of confinement controlled sublimation. If graphene is to be the new frontier in applied nanoelectronics, we require a complete understanding of how growth geometry and post processing impact the electrical character of graphene. For my thesis, I have focused on two areas of interest for electronic applications: analyzing the properties of ZZ-oriented ribbons on different SiC polytypes associated with ballistic transport and the effect of voltage gating with ALD AL_2O_3 on the semiconductive BL.

There have been many studies on the differences between AC- and ZZ- edge graphene nanoribbon behavior. The two orientations are known to have different band structures. Localized edge states are predicted along ZZ-edge ribbons and ballistic transport characteristics observed by Baringhaus et. al. are attributed to the ZZ edge state. While AC-edge ribbons with defects are predicted to have edge states as well [86], no edge states have been observed with ARPES and no ballistic transport has been measured on an AC-oriented ribbon. The choice of substrate has been largely overlooked in the graphene community, but I have shown that both edge orientation and polytype selection determine the presence of edge states as observed by ARPES.

In Chapter 3, I review work done in the AC-orientation on 4H-SiC and compare it to similar studies performed on 4H-ZZ-edge ribbons. ARPES studies demonstrate tilted and broadened Dirac cones originating from the AC facet sidewalls. The production of these cones proves that well ordered graphene forms on the 4H-AC sidewall. On the other hand, ZZ-edge ribbons on the same polytype are strongly bound to the surface, preventing the

formation of a Dirac cone. When lifted from the substrate via H_2-intercalation, the ZZ-facet cones can be observed in ARPES. I have analyzed the ARPES signal from these facets to determine that the 4H-ZZ-H_2 facet cones are broadened compared to the ML cone from the (0001) flat and symmetric about the tilted K-point, consistent with wide ribbons. The facet cone also exhibits a small bandgap (E_g = 0.2 eV). If we assume a neutrally doped ribbon, this gap is also evidence of a wide ribbon, W_r = 26 nm. The symmetric shape and band gap are consistent with the H_2-process delaminating nearly the entire sidewall, forming one wide ribbon across the facet.

Furthermore, transport measurements taken on ZZ-edge samples and H_2-passivated samples show that the ZZ edges are initially semiconducting with a small bandgap ($E_g \sim$ .17 eV). This would be the expected result as the ribbon is bound to the substrate in a similar manner as the semiconductive graphene BL on the (0001) surface. Hydrogen processing makes the 4H-ZZ ribbons conductive and the sheet resistance decreases by a factor of 10. Neither demonstrate ballistic character like some of the fixed geometry results on 4H-ZZ ribbons reported by Baringhaus et. al. One possible reason for the discrepancy is that the previously measured ballistic channels on 4H-SiC were taken from ribbons grown on the natural step, not patterned steps [120]. It is possible that graphene grown on the shallow natural 4H-steps is not attached to the SiC substrate and is thus conducting. Alternatively, the gating material used in fixed geometry measurements may delaminate the ribbon from the substrate and make it conductive. Natural step growth does not allow as much control over placement or ribbon width as the trench growth technique, so it is not ideal for highly scalable device architectures. Further research exploring CCS growth recipes of shallow 4H-ZZ trenches would confirm whether the production of edge states or ballistic transport is possible with trench growth on 4H-SiC.

In chapter 4, I demonstrate that ZZ-edge ribbons grown on 6H-SiC are very different electrically and structurally from similar ribbons grown on 4H-SiC. Facet cones are readily produced in ARPES without the need of an intercalation process. This proves that the si-

dewall graphene on 6H-SiC is well-ordered and less strongly bound to the substrate than 4H-ZZ ribbons. The cones have an asymmetric shape ($|\pi^+/\pi^-|$ = 1.7) as predicted for narrow ribbons [4]. The cone demonstrates a sizable bandgap (E_g = 0.4 eV) which I attribute to finite size effects. Finally, STS measurements on the 6H sidewalls demonstrate a varying LDOS with the applied voltage on the sidewall facets, but not on the (0001) flats. This implies that the ribbons terminate at the facet edges. STM topography, ARPES and STS all support that the ZZ-edge ribbons on the 6H-SiC substrate form many narrow ribbons on the sidewall as opposed to the wide ribbon formed on the 4H substrate after hydrogen processing.

The most notable difference in ZZ-edge ribbons on a 6H-SiC substrate is the observation of localized edge states in ARPES. There are two edge states near the fermi level at E_B= (56, 103) meV. They are flat and exist across the entire Brillioun zone. The nature of the ribbon edge terminations significantly affects the shape of the graphene edge states. At the trench top, the ribbon terminates into a buffer-like layer on the main (0001) flat. STM images show that the edge is ordered and commensurate. At the bottom, they may terminate with C-Si sp^3 bonds into the substrate or with C-C sp^2 bonds into a buffer-like layer on the (0001) nanoflats. In either case, the resulting ribbon has asymmetric edges. It is known that asymmetric edge terminations lead to flatter edge states across the entire BZ [20]. Furthermore, transport studies on 6H-ZZ ribbons show that they have constant resistance of $R_0 = e^2/h$ up to 15 μm, characteristic of ballistic transport. This is consistent with the idea presented by Baringhaus et. al. that ballistic transport measured on epitaxial GNR is activated by ZZ-edge states in the electronic band structure. There are no studies on the electronic character or transport properties of AC-edge ribbons on 6H-SiC. If there is ballistic transport along the AC-edge due to defects as predicted by Ref. [86], it would be an essential aspect to using these ribbons for applications in advanced nanoelectronics.

In Chapter 5, I demonstrate that the electronic and physical structure of the graphene buffer layer are altered by the growth of ALD aluminum oxide. Non-plasma assisted ALD

is generally assumed to be a passive process. However, it is activated by the water vapor oxidation of the surface. AFM imaging of ALD depositions on the BL and ML shows that the deposition is much more uniform on the BL, implying that there may be a surface interaction. Pinholes in the deposition allow me to use photoemission spectroscopy to observe the changes in the BL structure (both XPS and ARPES). Analysis of the XPS core levels shows that the intensity of the ML-like S_g peak increases by 280%. However, the intensity of the S_1 peak decreases, also associated with ML graphene. If pinholes preferentially formed on the ML, I would expect both of these peaks to increase in intensity. Because they do not, it implies that the oxide on the BL produces a higher density of in-plane sp^2 bonding, but it is not structurally identical to ML graphene. In addition, the graphene π-band intensity observed in ARPES increases by 260%. This is consistent with the BL sp^3-bonds partially delaminating from the substrate, forming in-plane sp^2-bonds. In this case, ALD AL_2O_3 is not an ideal gating material for the BL because it alters the electronic and physical character. Transport studies across the BL are still an ongoing area of research. Comparative transport measurements on bare and gated BL samples would determine how a gating layer alters the transport properties of the underlying graphene. Furthermore, Raman results suggest that the conductive ML is also altered by ALD depositions. Understanding the structural changes in the ML may also have implications about the use of an oxide gating layer in device architectures.

My results demonstrate that graphene holds a great deal of potential for nanoscale devices due to its unique finite size effects and engineered electrical properties. Closer attention to substrate selection and post-processing effects on the graphene epilayers will be required if there is to be a new graphene electronic platform. There is still a broad range of future research required to invent such a revolutionary platform, but the versatility and 2-dimensional nature of graphene provides an interesting potential solution to the current issue of miniaturization faced in the semiconductor market today.

APPENDIX A

ARPES GEOMETRY

Interpretation of the ARPES measurements depends on the detector and sample geometry used. The Cassiopee beamline at Soleil uses a hemispherical detector with a ϕ-acceptance range of $\pm 15^o$. This decomposes $k_{||}$ into its components k_x^o and k_y^o as follows:

$$\begin{aligned} E_K &= E_S - E_{BE} - \Phi \\ |k| &= \frac{\sqrt{2mE_K}}{\hbar} \approx .512 \mathring{A}^{-1} \\ k_x^o &= |k| \sin(\theta) \cos(\phi) \\ k_y^o &= |k| \sin(\phi) \\ k_z^o &= |k| cos(\theta) cos(\phi) \end{aligned} \tag{A.1}$$

where .512 is the approximate value of $\frac{\sqrt{2m_e}}{\hbar}$ in units of $\text{Å}^{-1}\text{eV}^{-.5}$, E_K is the kinetic energy of the electron at the detector, and ϕ and θ are the polar and azimuthal entrance angles in a hemispherical detector. The coordinate geometry is shown in figure A.1. The experimental correction for entrance aperture optics, ξ, is omitted for simplicity but included in the thesis equations 2.4.

Previous samples (the ZZ H-Passivated samples) were mounted on a stage that only had the flexibility to move in θ, so in order to image across the K-points and expected facet cone locations, the sample must be tilted by $\delta \sim 15^\circ$ (see Fig. A.2(a)). This was done by mounting the sample on a wedge, where the incline rotated the sample about the k_x^o axis. The coordinate transformation into the frame of the wedge (0001) surface, k_x^W and k_y^W, is

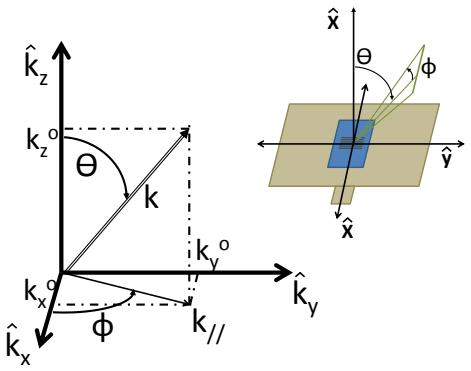

Figure A.1: The flat sample geometry on the stage. k_x^o and k_y^o are the parallel components of momentum, shown on the x-y plane as $k_{||}$. ϕ and θ indicated.

then derived as follows:

$$\begin{bmatrix} k_y^W \\ k_z^W \end{bmatrix} = \begin{bmatrix} \cos(\delta) & \sin(\delta) \\ -\sin(\delta) & \cos(\delta) \end{bmatrix} \begin{bmatrix} k_y^o \\ k_z^o \end{bmatrix} \tag{A.2}$$

$$\begin{aligned} k_x^W =& k_x^o = |k| \sin\theta \cos\phi \\ k_y^W =& k_y^o \cos(\delta) + k_z^o \sin(\delta) = |k| \Big(\sin\phi \cos\delta + \cos\phi \cos\theta \sin\delta \Big) \\ k_z^W =& -k_y^o \sin(\delta) + k_z^o \cos(\delta) = |k| \Big(-\sin\phi \sin\delta + \cos\phi \cos\theta \cos\delta \Big) \end{aligned} \tag{A.3}$$

In order to characterize the ARPES signal from the sidewalls, the data must be rotated into the frame of the facets on the wedge. The angle of the facet normal relative to the (0001) SiC normal is defined as θ_F. If wedge mounted the rotation is about the k_y^W axis, as shown in Fig. A.2(b). This can be expressed as another Cartesian rotation as follows:

$$\begin{bmatrix} k_z^{WF} \\ k_x^{WF} \end{bmatrix} = \begin{bmatrix} \cos(\theta_F) & \sin(\theta_F) \\ -\sin(\theta_F) & \cos(\theta_F) \end{bmatrix} \begin{bmatrix} k_z^W \\ k_x^W \end{bmatrix} \tag{A.4}$$

$$
\begin{aligned}
k_y^{WF} =& k_y^W = |k|\Big(\sin\phi\cos\delta + \cos\phi\cos\theta\sin\delta \Big) \\
k_z^{WF} =& k_z^W \cos(\theta_F) + k_x^W \sin(\theta_F) \\
=& |k|\Big(\big(-\sin\phi\sin\delta + \cos\phi\cos\theta\cos\delta \big)\cos\theta_F + \sin\theta\cos\phi\sin\theta_F \Big) \qquad \text{(A.5)} \\
k_x^{WF} =& -k_z^W \sin(\theta_F) + k_x^W \cos(\theta_F) \\
=& |k|\Big(\big(-\sin\phi\sin\delta + \cos\phi\cos\theta\cos\delta \big)\sin\theta_F + \sin\theta\cos\phi\cos\theta_F \Big)
\end{aligned}
$$

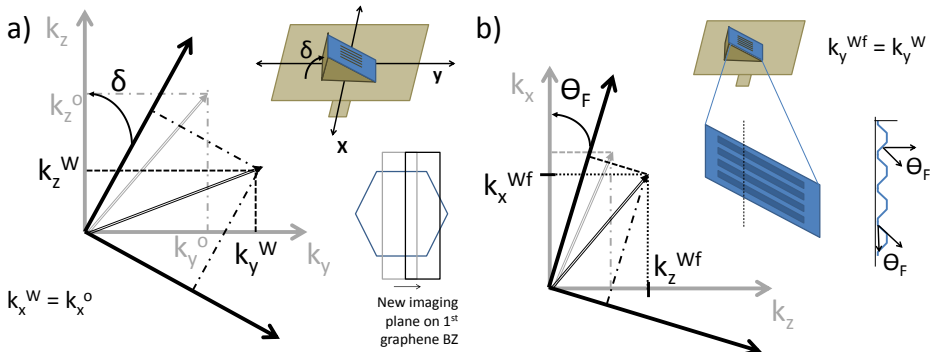

Figure A.2: a) Schematic of a wedge-mounted sample. A rotation about k_x^o puts the data in the frame of the wedge normal, $k_{x,y,z}^W$. Derivation of coordinates with matrix rotation described in eqn. A.2. b) The trench rotation for a wedge-mounted sample. The trench facets rotate the ARPES signal about the k_y^W, derivation of coordinates relative to the facet normal ($k_{x,y,z}^W F$) described by eqn. A.4.

A.1 Flat Sample Geometry

Note that the coordinate transformation in eqn. A.5 are specifically derived for wedge mounted samples as shown in A.2(c). The 4H-AC or the 6H-ZZ ribbon samples were not wedge mounted (APPES discussed in sections 3.1.2 and 4.3.1). For the 4H-AC case, the trenches are aligned with the y-axis, shown in figureA.3(a). To rotate this data into the

frame of the AC sidewalls, δ = 0 and the facet angle is θ_F.

For the 6H-ZZ case the trenches were aligned with the x-axis, shown in figureA.3(b). Then, the coordinate transformations are obtained by setting θ_F=0 in eqn. A.5, and inputting the facet angle into δ instead of a wedge angle. This is the formulation discussed in section 2.6.1, shown in eqn. 2.4.

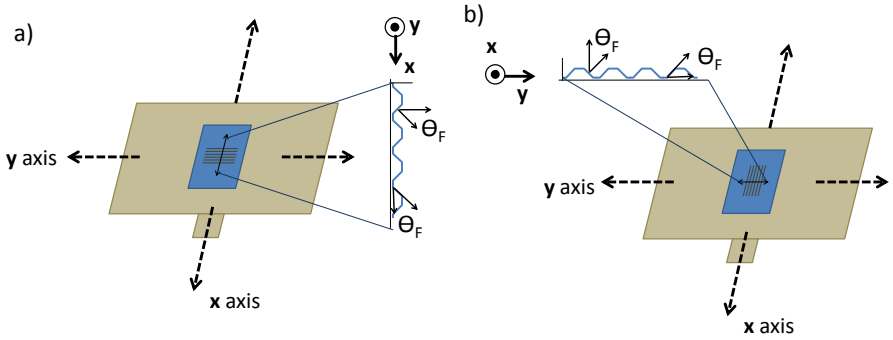

Figure A.3: a) Mounting geometry for 4H-AC samples, the facet angle rotated about k_y^o. b) Mounting geometry for 6H-ZZ samples, the facet angle rotated about k_x^o.

The only case not discussed in this thesis is that where the sample is rotated by a wedge angle about the k_y^o axis.

APPENDIX B

ALD PROCESSING

ALD processes were carried out in an in-house built ALD chamber at the GT IEN Marcus Cleanroom. This ALD chamber is dedicated to aluminum oxide alone in order to avoid cross-contamination with other metals. The chamber temperature was 250 C is pumped down to its base pressure at 5 mT. The chamber temperature serves two purposes: first, after the chamber is pumped down, the samples are left to outgas at 250 C for 15 minutes, allowing deposited carbon-oxide contaminants to desorb. Secondly, higher deposition temperatures with shorter pulse times produce better-ordered ALD deposits.

Image from sums.gatech.edu

ALD deposition

Material	Time (s)
H_2O	.5
N_2	15
TMA	.5
N_2	15

B.0.1 Complete Fitting Parameters

Here I include the integrated intensities of the C1s core level components determined by the LSRA algorithm in section 5.3.2. The bulk C1s core level yield will be independent of surface changes, so it is used to normalize the count data from the surface C1s components. Normalized areas for each component are calculated as follows:

$$S_{x,Norm} = \frac{S_x}{C_B + C'_B} \tag{B.1}$$

where $S_{x,Norm}$ is the normalized intensity of the core level, S_x is the absolute intensity in counts of that core level, and $C_B + C'_B$ are the bulk C1s core levels.

Table B.1: Parameters determined from LSRA core level fitting, before and after oxide deposition. Heights and areas are given in counts, Norm A is the normalized area by the C_B+$C_{B'}$ integrated area for direct comparison.

	Bare	ΔE = .25eV	1 scan	Oxide	ΔE = .1eV	10 scans	
	H	Area	Norm A	H	Area	Norm A	$\frac{A_{ox}-A_{bare}}{A_{bare}}$
S_2	358	344	0.73	4200	4313	0.65	-0.10
S_1	607	580	1.22	6455	6021	0.91	-0.26
S_g	92	118	0.25	5018	6421	0.97	2.88
C_B'	394	268	0.56	5465	3722	0.56	0.00
C_B	414	205	0.43	5741	2886	0.44	0.00

APPENDIX C
GROWTH PARAMETERS

C.1 Crucible

My crucible has a leak hole with 1 mm diameter on the lid. Every 10 samples, the crucible must be reconditioned by growing the ML recipe with an empty chamber. This will remove a substantial amount of the silicon coating on the inner wall. Then a ML sample is grown to reestablish a new Si coating inside the crucible. This 'dummy' sample should not be used as a ML sample. It will likely have been overgrown due to a lower Si partial pressure at the sample surface. The dummy samples are only used to season the graphite crucible with new silicon.

Recipes for my crucible are given below.

Sample	Growth Temp (C)	Growth Time (s)
4H-AC	1560±5	90±5
4H-ZZ	1560±5	90±5
BL	1420 ± 10	1800
ML	1550 ± 10	1800

C.2 MEMS

Before processing, all samples are sonicated in acetone for 20 minutes, then immediately in IPA for an additional 15 minutes to remove any particles stuck on the surface. After the IPA bath, the sample is dried with N_2.

C.2.1 ZEP Processing

1) Spin on 1:1 ZEP520a:anisole at 4000 rpm with 2000 rpm/s ramp rate, for 60 sec (ramp time included).

2) Bake for 2 min at 180 C (check localized hot plate temperature is accurate).

3) A typical e-beam base dose exposure for Zeonrex ZEP520a is 170 μC/cm^2. For all ribbon features patterned in this work, base dose used was 170-210 μC/cm^2 [8].

4) Develop for 2 min in Amyl acetate and immediately rinse gently with IPA for 20 sec to cease developing. Dry off sample gently with N_2.

5) To remove cured resist, submerge in 1165 for 15 min. Submerge briefly in acetone, then in IPA to remove residues and dry with N_2.

C.2.2 RIE Etching

Reactive ion etching of SiC was performed in the Vision 2 Plasma Etching furnace in the GaTech Pettit Cleanroom with SF_6.

Pressure	80 mTorr
Platen RF1	200 W
Ar	10 sccm
O_2	7 sccm
SF_6	13 sccm

H_2-passivation of 4H-ZZ samples was carried out in the GT IEN Cleanroom CVD FirstNano Graphene furnace at 900 C for one hour. Subsequent analysis with XPS shows that intercalation is completed.

REFERENCES

[1] J. Baringhaus, M. Ruan, F. Edler, A. Tejeda, M. Sicot, A. Taleb-Ibrahimi, A.-P. Li, Z. Jiang, E. H. Conrad, C. Berger, and et al., *Exceptional ballistic transport in epitaxial graphene nanoribbons*, 7488. 2014, vol. 506, 349354.

[2] N. Nordell, S. Karlsson, and A. Konstantinov, "Equilibrium crystal shapes for 6h and 4h sic grown on non-planar substrates," *Materials Science and Engineering: B*, vol. 61-62, 130134, 1999.

[3] F. Speck, M. Ostler, J. Rhrl, K. V. Emtsev, M. Hundhausen, L. Ley, and T. Seyller, "Atomic layer deposited aluminum oxide films on graphite and graphene studied by xps and afm," *physica status solidi (c)*, vol. 7, no. 2, 398401, 2010.

[4] K. Nakada, M. Fujita, G. Dresselhaus, and M. S. Dresselhaus, "Edge state in graphene ribbons: Nanometer size effect and edge shape dependence," *Physical Review B*, vol. 54, no. 24, 1795417961, 1996.

[5] L. Yang, C.-H. Park, Y.-W. Son, M. L. Cohen, and S. G. Louie, "Quasiparticle energies and band gaps in graphene nanoribbons," *Physical Review Letters*, vol. 99, no. 18, 2007.

[6] A. K. Geim and K. S. Novoselov, "The rise of graphene," *Nanoscience and Technology*, 1119, 2009.

[7] K. Wakabayashi, "Electronic and transport properties of graphene nanoribbons," *Graphene and Its Fascinating Attributes*, 167178, 2011.

[8] M. S. Nevius, "Improved growth, ordering and characterization of sidewall epitaxial graphene nanoribbons, phd diss.," *Georgia Institute of Technology*, 2016.

[9] P. R. Wallace, "The band theory of graphite," *Physical Review*, vol. 71, no. 9, 622634, 1947.

[10] K. S. Novoselov, "Electric field effect in atomically thin carbon films," *Science*, vol. 306, no. 5696, 666669, 2004.

[11] K. Bolotin, K. Sikes, Z. Jiang, M. Klima, G. Fudenberg, J. Hone, P. Kim, and H. Stormer, "Ultrahigh electron mobility in suspended graphene," *Solid State Communications*, vol. 146, no. 9-10, 351355, 2008.

[12] J. Baringhaus, J. Aprojanz, J. Wiegand, D. Laube, M. Halbauer, J. Hbner, M. Oestreich, and C. Tegenkamp, "Growth and characterization of sidewall graphene nanoribbons," *Applied Physics Letters*, vol. 106, no. 4, p. 043 109, 2015.

[13] Y. Zhang, Y.-W. Tan, H. Stormer, and P. Kim, "Experimental observation of the quantum hall effect and berry's phase in graphene," *Nature Letters*, vol. 438, 2005.

[14] K. S. Novoselov, S. V. Morozov, T. M. G. Mohinddin, L. A. Ponomarenko, D. C. Elias, R. Yang, I. I. Barbolina, P. Blake, T. J. Booth, D. Jiang, J. Giesbers, E. W. Hill, and A. K. Geim, "Electronic properties of graphene," *Physics Statics Solidi b*, vol. 244, no. 11, 41064111, 2007.

[15] J. Jobst, D. Waldmann, F. Speck, R. Hirner, D. K. Maude, T. Seyller, and H. B. Weber, "Quantum oscillations and quantum hall effect in epitaxial graphene," *Physical Review B*, vol. 81, no. 19, 2010.

[16] V. P. Gusynin and S. G. Sharapov, "Unconventional integer quantum hall effect in graphene," *Physical Review Letters*, vol. 95, no. 14, 2005.

[17] K. Wakabayashi, K.-I. Sasaki, T. Nakanishi, and T. Enoki, "Electronic states of graphene nanoribbons and analytical solutions," *Science and Technology of Advanced Materials*, vol. 11, no. 5, p. 054 504, 2010.

[18] Y.-W. Son, M. L. Cohen, and S. G. Louie, "Half-metallic graphene nanoribbons," *Nature*, vol. 444, no. 7117, 347349, 2006.

[19] A. Zhang, Y. Wu, S.-H. Ke, Y. P. Feng, and C. Zhang, "Bandgap engineering of zigzag graphene nanoribbons by manipulating edge states via defective boundaries," *Nanotechnology*, vol. 22, no. 43, p. 435 702, 2011.

[20] X. Deng, Z. Zhang, G. Tang, Z. Fan, and C. Yang, "Spin filter effects in zigzag-edge graphene nanoribbons with symmetric and asymmetric edge hydrogenations," *Carbon*, vol. 66, 646653, 2014.

[21] M. Fujita, K. Wakabayashi, K. Nakada, and K. Kusakabe, "Peculiar localized state at zigzag graphite edge," *Journal of the Physical Society of Japan*, vol. 65, no. 7, 19201923, 1996.

[22] H. Lee, Y.-W. Son, N. Park, S. Han, and J. Yu, "Magnetic ordering at the edges of graphitic fragments: Magnetic tail interactions between the edge-localized states," *Physical Review B*, vol. 72, no. 17, 2005.

[23] Y.-W. Son, M. L. Cohen, and S. G. Louie, "Energy gaps in graphene nanoribbons," *Physical Review Letters*, vol. 97, no. 21, 2006.

[24] A. L. Miettinen, M. S. Nevius, W. Ko, M. Kolmer, A.-P. Li, M. N. Nair, B. Kierren, L. Moreau, E. H. Conrad, A. Tejeda, and et al., "Edge states and ballistic transport in zigzag graphene ribbons: The role of sic polytypes," *Physical Review B*, vol. 100, no. 4, 2019.

[25] H. Zheng, Z. F. Wang, T. Luo, Q. W. Shi, and J. Chen, "Analytical study of electronic structure in armchair graphene nanoribbons," *Physical Review B*, vol. 75, no. 16, 2007.

[26] A. R. Akhmerov and C. W. J. Beenakker, "Boundary conditions for dirac fermions on a terminated honeycomb lattice," *Physical Review B*, vol. 77, no. 8, 2008.

[27] S. Datta, *Electronic transport in mesoscopic systems*. Cambridge, 1995.

[28] C. Lee, X. Wei, J. W. Kysar, and J. Hone, "Measurement of the elastic properties and intrinsic strength of monolayer graphene," *Science*, vol. 321, no. 5887, 385388, 2008.

[29] L. Tapaszt, G. Dobrik, P. Lambin, and L. P. Bir, "Tailoring the atomic structure of graphene nanoribbons by scanning tunnelling microscope lithography," *Nature Nanotechnology*, vol. 3, no. 7, 397401, 2008.

[30] M. Y. Han, B. zyilmaz, Y. Zhang, and P. Kim, "Energy band-gap engineering of graphene nanoribbons," *Physical Review Letters*, vol. 98, no. 20, 2007.

[31] B. C. Brodie, "Researches on the atomic weight of graphite," *Q. J. Chem. Soc.*, vol. 12, no. 1, 261268, 1860.

[32] S. Stankovich, D. A. Dikin, R. D. Piner, K. A. Kohlhaas, A. Kleinhammes, Y. Jia, Y. Wu, S. T. Nguyen, and R. S. Ruoff, "Synthesis of graphene-based nanosheets via chemical reduction of exfoliated graphite oxide," *Carbon*, vol. 45, no. 7, 15581565, 2007.

[33] J. Song, X. Wang, and C.-T. Chang, "Preparation and characterization of graphene oxide," *Journal of Nanomaterials*, 276143 2014.

[34] R. R. Nair, W. Ren, R. Jalil, I. Riaz, V. G. Kravets, L. Britnell, P. Blake, F. Schedin, A. S. Mayorov, S. Yuan, and et al., "Fluorinated graphene: Fluorographene: A two-dimensional counterpart of teflon (small 24/2010)," *Small*, vol. 6, no. 24, 27732773, 2010.

[35] X. Li, W. Cai, J. An, S. Kim, J. Nah, D. Yang, R. Piner, A. Velamakanni, I. Jung, E. Tutuc, and et al., "Large-area synthesis of high-quality and uniform graphene films on copper foils," *Science*, vol. 324, no. 5932, 13121314, 2009.

[36] X. Li, C. W. Magnuson, A. Venugopal, J. An, J. W. Suk, B. Han, M. Borysiak, W. Cai, A. Velamakanni, Y. Zhu, and et al., "Graphene films with large domain size by a two-step chemical vapor deposition process," *Nano Letters*, vol. 10, no. 11, 43284334, 2010.

[37] P. W. Sutter, J.-I. Flege, and E. A. Sutter, "Epitaxial graphene on ruthenium," *Nature Materials*, vol. 7, no. 5, 406411, 2008.

[38] K. S. Kim, Y. Zhao, H. Jang, S. Y. Lee, J. M. Kim, K. S. Kim, J.-H. Ahn, P. Kim, J.-Y. Choi, B. H. Hong, and et al., "Large-scale pattern growth of graphene films for stretchable transparent electrodes," *Nature*, vol. 457, no. 7230, 706710, 2009.

[39] Y. Wang, Y. Zheng, X. Xu, E. Dubuisson, Q. Bao, J. Lu, and K. P. Loh, "Electrochemical delamination of cvd-grown graphene film: Toward the recyclable use of copper catalyst," *ACS Nano*, vol. 5, no. 12, 99279933, 2011.

[40] A. V. Bommel, J. Crombeen, and A. V. Tooren, "Leed and auger electron observations of the sic(0001) surface," *Surface Science*, vol. 48, no. 2, 463472, 1975.

[41] W. A. D. Heer, C. Berger, M. Ruan, M. Sprinkle, X. Li, Y. Hu, B. Zhang, J. Hankinson, and E. Conrad, "Large area and structured epitaxial graphene produced by confinement controlled sublimation of silicon carbide," *Proceedings of the National Academy of Sciences*, vol. 108, no. 41, 1690016905, 2011.

[42] I. Forbeaux, J.-M. Themlin, and J.-M. Debever, "Heteroepitaxial graphite on 6h-sic(0001): Interface formation through conduction-band electronic structure," *Physical Review B*, vol. 58, no. 24, 1639616406, 1998.

[43] A. Charrier, A. Coati, T. Argunova, F. Thibaudau, Y. Garreau, R. Pinchaux, I. Forbeaux, J.-M. Debever, M. Sauvage-Simkin, J.-M. Themlin, and et al., "Solid-state decomposition of silicon carbide for growing ultra-thin heteroepitaxial graphite films," *Journal of Applied Physics*, vol. 92, no. 5, 24792484, 2002.

[44] C. Virojanadara, A. Zakharov, R. Yakimova, and L. Johansson, "Buffer layer free large area bi-layer graphene on sic(0001)," *Surface Science*, vol. 604, no. 2, 2010.

[45] S. Y. Zhou, G.-H. Gweon, A. V. Fedorov, P. N. First, W. A. D. Heer, D.-H. Lee, F. Guinea, A. H. C. Neto, and A. Lanzara, "Substrate-induced bandgap opening in epitaxial graphene," *Nature Materials*, vol. 6, no. 11, 916916, 2007.

[46] M. Ostler, R. J. Koch, F. Speck, F. Fromm, H. Vita, M. Hundhausen, K. Horn, and T. Seyller, "Decoupling the graphene buffer layer from sic(0001) via interface oxidation," *Materials Science Forum*, vol. 717-720, 649652, 2012.

[47] M. Conrad, J. Rault, Y. Utsumi, Y. Garreau, A. Vlad, A. Coati, J.-P. Rueff, P. F. Miceli, and E. H. Conrad, "Structure and evolution of semiconducting buffer graphene grown on sic(0001)," *Physical Review B*, vol. 96, no. 19, 2017.

[48] J. Hass, F. Varchon, J. E. Milln-Otoya, M. Sprinkle, N. Sharma, W. A. D. Heer, C. Berger, P. N. First, L. Magaud, E. H. Conrad, and et al., "Why multilayer graphene on 4h-sic(000-1)behaves like a single sheet of graphene," *Physical Review Letters*, vol. 100, no. 12, 2008.

[49] J. Hass, R. Feng, T. Li, X. Li, Z. Zong, W. A. D. Heer, P. N. First, E. H. Conrad, C. A. Jeffrey, C. Berger, and et al., "Highly ordered graphene for two dimensional electronics," *Applied Physics Letters*, vol. 89, no. 14, p. 143 106, 2006.

[50] W. A. D. Heer, C. Berger, X. Wu, P. N. First, E. H. Conrad, X. Li, T. Li, M. Sprinkle, J. Hass, M. L. Sadowski, and et al., "Epitaxial graphene," *Solid State Communications*, vol. 143, no. 1-2, 92100, 2007.

[51] C. Berger, Z. Song, T. Li, X. Li, A. Y. Ogbazghi, R. Feng, Z. Dai, A. N. Marchenkov, E. H. Conrad, P. N. First, and et al., *Ultrathin epitaxial graphite: 2d electron gas properties and a route toward graphene-based nanoelectronics*, 52. 2004, vol. 108, 1991219916.

[52] K. V. Emtsev, A. Bostwick, K. Horn, J. Jobst, G. L. Kellogg, L. Ley, J. L. Mcchesney, T. Ohta, S. A. Reshanov, J. Rhrl, and et al., "Towards wafer-size graphene layers by atmospheric pressure graphitization of silicon carbide," *Nature Materials*, vol. 8, no. 3, 203207, 2009.

[53] M. Conrad, "Structure and properties of incommensurate and commensurate phases of graphene on sic," *Georgia Institute of Technology Thesis Defense*, 2017.

[54] M. S. Nevius, F. Wang, C. Mathieu, N. Barrett, A. Sala, T. O. Mente, A. Locatelli, and E. H. Conrad, "The bottom-up growth of edge specific graphene nanoribbons," *Nano Letters*, vol. 14, no. 11, 60806086, 2014.

[55] M. S. Nevius, M. Conrad, F. Wang, A. Celis, M. N. Nair, A. Taleb-Ibrahimi, A. Tejeda, and E. H. Conrad, "Semiconducting graphene from highly ordered substrate interactions," *Physical Review Letters*, vol. 115, no. 13, 2015.

[56] M. Sprinkle, D. Siegel, Y. Hu, J. Hicks, A. Tejeda, A. Taleb-Ibrahimi, P. L. Fvre, F. Bertran, S. Vizzini, H. Enriquez, and et al., "First direct observation of a nearly ideal graphene band structure," *Physical Review Letters*, vol. 103, no. 22, 2009.

[57] F. Varchon, R. Feng, J. Hass, X. Li, B. N. Nguyen, C. Naud, P. Mallet, J.-Y. Veuillen, C. Berger, E. H. Conrad, and et al., "Electronic structure of epitaxial graphene

layers on sic: Effect of the substrate," *Physical Review Letters*, vol. 99, no. 12, 2007.

[58] A. A. Ahmadieh and H. A. Rafizadeh, "Dispersion curves and elastic constants of graphite," *Physical Review B*, vol. 9, no. 6, 27852785, 1974.

[59] J. B. Nelson and D. P. Riley, "The thermal expansion of graphite from 15 c. to 800 c.: Part i. experimental," *Proceedings of the Physical Society*, vol. 57, no. 6, 477486, 1945.

[60] Y. Baskin and L. Meyer, "Lattice constants of graphite at low temperatures," *Physical Review*, vol. 100, no. 2, 544544, 1955.

[61] M. Weinert, E. Wimmer, and A. J. Freeman, "Total-energy all-electron density functional method for bulk solids and surfaces," *Physical Review B*, vol. 26, no. 8, 45714578, 1982.

[62] H. ahin, S. Cahangirov, M. Topsakal, E. Bekaroglu, E. Akturk, R. T. Senger, and S. Ciraci, "Monolayer honeycomb structures of group-iv elements and iii-v binary compounds: First-principles calculations," *Physical Review B*, vol. 80, no. 15, 2009.

[63] S. Wang, "Studies of physical and chemical properties of two-dimensional hexagonal crystals by first-principles calculation," *Journal of the Physical Society of Japan*, vol. 79, no. 6, p. 064 602, 2010.

[64] M. Conrad, F. Wang, M. Nevius, K. Jinkins, A. Celis, M. N. Nair, A. Taleb-Ibrahimi, A. Tejeda, Y. Garreau, A. Vlad, and et al., "Wide band gap semiconductor from a hidden 2d incommensurate graphene phase," *Nano Letters*, vol. 17, no. 1, 341347, 2017.

[65] T. Schumann, M. Dubslaff, M. H. Oliveira, M. Hanke, J. M. J. Lopes, and H. Riechert, "Effect of buffer layer coupling on the lattice parameter of epitaxial graphene on sic(0001)," *Physical Review B*, vol. 90, no. 4, 2014.

[66] J. Turmaud, "Variable range hopping conduction in the epitaxial graphene buffer layer, phd diss.," *Georgia Institute of Technology*, 2018.

[67] T. Ohta, A. Bostwick, J. L. Mcchesney, T. Seyller, K. Horn, and E. Rotenberg, "Interlayer interaction and electronic screening in multilayer graphene investigated with angle-resolved photoemission spectroscopy," *Physical Review Letters*, vol. 98, no. 20, 2007.

[68] D. V. Kosynkin, A. L. Higginbotham, A. Sinitskii, J. R. Lomeda, A. Dimiev, B. K. Price, and J. M. Tour, "Longitudinal unzipping of carbon nanotubes to form graphene nanoribbons," *Nature*, vol. 458, no. 7240, 872876, 2009.

[69] L. Ci, Z. Xu, L. Wang, W. Gao, F. Ding, K. F. Kelly, B. I. Yakobson, and P. M. Ajayan, "Controlled nanocutting of graphene," *Nano Research*, vol. 1, no. 2, 116122, 2008.

[70] P. Ruffieux, S. Wang, B. Yang, C. Snchez-Snchez, J. Liu, T. Dienel, L. Talirz, P. Shinde, C. A. Pignedoli, D. Passerone, and et al., "On-surface synthesis of graphene nanoribbons with zigzag edge topology," *Nature*, vol. 531, no. 7595, 489492, 2016.

[71] W. Norimatsu and M. Kusunoki, "Formation process of graphene on sic (0001)," *Physica E: Low-dimensional Systems and Nanostructures*, vol. 42, no. 4, 691694, 2010.

[72] I. Palacio, A. Celis, M. N. Nair, A. Gloter, A. Zobelli, M. Sicot, D. Malterre, M. S. Nevius, W. A. D. Heer, C. Berger, and et al., "Atomic structure of epitaxial graphene sidewall nanoribbons: Flat graphene, miniribbons, and the confinement gap," *Nano Letters*, vol. 15, no. 1, 182189, 2015.

[73] K. Koshelev, M. A. Mohammad, T. Fito, K. L. Westra, S. K. Dew, and M. Stepanova, "Comparison between zep and pmma resists for nanoscale electron beam lithography experimentally and by numerical modeling," *Journal of Vacuum Science and Technology B, Nanotechnology and Microelectronics: Materials, Processing, Measurement, and Phenomena*, vol. 29, no. 6, 2011.

[74] J. Hicks, A. Tejeda, A. Taleb-Ibrahimi, M. S. Nevius, F. Wang, K. Shepperd, J. Palmer, F. Bertran, P. L. Fvre, J. Kunc, and et al., "A wide-bandgap metalsemiconductormetal nanostructure made entirely from graphene," *Nature Physics*, vol. 9, no. 1, 4954, 2012.

[75] A. Damascelli, "Probing the electronic structure of complex systems by arpes," *Physica Scripta*, vol. T109, p. 61, 2004.

[76] E. L. Shirley, L. J. Terminello, A. Santoni, and F. J. Himpsel, "Brillouin-zone-selection effects in graphite photoelectron angular distributions," *Physical Review B*, vol. 51, no. 19, 1361413622, 1995.

[77] A. C. Ferrari and D. M. Basko, "Raman spectroscopy as a versatile tool for studying the properties of graphene," *Nature Nanotechnology*, vol. 8, no. 4, 235246, 2013.

[78] J. Rhrl, M. Hundhausen, K. V. Emtsev, T. Seyller, R. Graupner, and L. Ley, "Raman spectra of epitaxial graphene on sic(0001)," *Applied Physics Letters*, vol. 92, no. 20, p. 201 918, 2008.

[79] A. C. Ferrari and D. M. Basko, "Raman spectroscopy as a versatile tool for studying the properties of graphene," *Nature nanotechnology*, vol. 8, no. 4, p. 235, 2013.

[80] A. C. Ferrari, J. C. Meyer, V. Scardaci, C. Casiraghi, M. Lazzeri, F. Mauri, S. Piscanec, D. Jiang, K. S. Novoselov, S. Roth, and et al., "Raman spectrum of graphene and graphene layers," *Physical Review Letters*, vol. 97, no. 18, 2006.

[81] M. Sprinkle, M. Ruan., Y. Hu, J. Hankinson, B. Rubio-Roy M.and Zhang, X. Wu, C. Berger, and W. A. de Heer, "Scalable templated growth of graphene nanoribbons on sic," *Nature Nanotechnology*, 2009.

[82] C. Riedl, C. Coletti, T. Iwasaki, A. A. Zakharov, and U. Starke, "Quasi-free-standing epitaxial graphene on sic obtained by hydrogen intercalation," *Physical Review Letters*, vol. 103, no. 24, 2009.

[83] R. C. Jaeger, *Introduction to microelectronic fabrication*. Pearson Education South Asia, 2014.

[84] A. Nakajima, H. Yokoya, Y. Furukawa, and H. Yonezu, "Step control of vicinal 6hsic(0001) surface by h2 etching," *Journal of Applied Physics*, vol. 97, no. 10, p. 104 919, 2005.

[85] V. Borovikov and A. Zangwill, "Step bunching of vicinal 6h-sic(0001) surfaces," *Physical Review B*, vol. 79, 2009.

[86] J. Aprojanz, S. R. Power, P. Bampoulis, S. Roche, A.-P. Jauho, H. J. W. Zandvliet, A. A. Zakharov, and C. Tegenkamp, "Ballistic tracks in graphene nanoribbons," *Nature Communications*, vol. 9, no. 1, 2018.

[87] J. Guo, D. Gunlycke, and C. T. White, "Field effect on spin-polarized transport in graphene nanoribbons," *Applied Physics Letters*, vol. 92, no. 16, p. 163 109, 2008.

[88] L. Pisani, J. A. Chan, B. Montanari, and N. M. Harrison, "Electronic structure and magnetic properties of graphitic ribbons," *Physical Review B*, vol. 75, no. 6, 2007.

[89] J. Jung and A. H. Macdonald, "Carrier density and magnetism in graphene zigzag nanoribbons," *Physical Review B*, vol. 79, no. 23, 2009.

[90] O. V. Yazyev, "Emergence of magnetism in graphene materials and nanostructures," *Reports on Progress in Physics*, vol. 73, no. 5, p. 056 501, 2010.

[91] C. Riedl and U. Starke, "Structural and electronic properties of epitaxial graphene on sic (0001)," *Materials Science Forum*, vol. 615-617, 219222, 2009.

[92] S. Kim, J. Nah, I. Jo, D. Shahrjerdi, L. Colombo, Z. Yao, E. Tutuc, and S. K. Banerjee, "Realization of a high mobility dual-gated graphene field-effect transistor with al2o3 dielectric," *Applied Physics Letters*, vol. 94, no. 6, p. 062 107, 2009.

[93] B. Lee, G. Mordi, M. J. Kim, Y. J. Chabal, E. M. Vogel, R. M. Wallace, K. J. Cho, L. Colombo, and J. Kim, "Characteristics of high-k al2o3 dielectric using ozone-based atomic layer deposition for dual-gated graphene devices," *Applied Physics Letters*, vol. 97, no. 4, p. 043 107, 2010.

[94] M. Rubio-Roy, F. Zaman, Y. Hu, C. Berger, M. W. Moseley, J. D. Meindl, and W. A. D. Heer, "Structured epitaxial graphene growth on sic by selective graphitization using a patterned aln cap," *Applied Physics Letters*, vol. 96, no. 8, p. 082 112, 2010.

[95] R. Puybaret, J. Hankinson, J. Palmer, C. Bouvier, A. Ougazzaden, P. L. Voss, C. Berger, and W. A. D. Heer, "Scalable control of graphene growth on 4h-sic c-face using decomposing silicon nitride masks," *Journal of Physics D: Applied Physics*, vol. 48, no. 15, p. 152 001, 2015.

[96] T. Lim, D. Kim, and S. Ju, "Direct deposition of aluminum oxide gate dielectric on graphene channel using nitrogen plasma treatment," *Applied Physics Letters*, vol. 103, no. 1, p. 013 107, 2013.

[97] L. Wang, J. J. Travis, A. S. Cavanagh, X. Liu, S. P. Koenig, P. Y. Huang, S. M. George, and J. S. Bunch, "Ultrathin oxide films by atomic layer deposition on graphene," *Nano Letters*, vol. 12, no. 7, 37063710, 2012.

[98] X. Tang, N. Reckinger, O. Poncelet, P. Louette, F. Urea, H. Idrissi, S. Turner, D. Cabosart, J.-F. Colomer, J.-P. Raskin, and et al., "Damage evaluation in graphene underlying atomic layer deposition dielectrics," *Scientific Reports*, vol. 5, no. 1, 2015.

[99] M. Ostler, F. Fromm, R. J. Koch, P. Wehrfritz, F. Speck, H. Vita, S. Bttcher, K. Horn, and T. Seyller, "Buffer layer free graphene on sic(0001) via interface oxidation in water vapor," *Carbon*, vol. 70, 258265, 2014.

[100] R. W. Johnson, A. Hultqvist, and S. F. Bent, "A brief review of atomic layer deposition: From fundamentals to applications," *Materials Today*, vol. 17, no. 5, 236246, 2014.

[101] R. Rammula, L. Aarik, A. Kasikov, J. Kozlova, T. Kahro, L. Matisen, A. Niilisk, H. Alles, and J. Aarik, "Atomic layer deposition of aluminum oxide films on graphene," in *IOP Conference Series: Materials Science and Engineering*, IOP Publishing, vol. 49, 2013, p. 012 014.

[102] Y.-M. Lin, K. A. Jenkins, A. Valdes-Garcia, J. P. Small, D. B. Farmer, and P. Avouris, "Operation of graphene transistors at gigahertz frequencies," *Nano Letters*, vol. 9, no. 1, 422426, 2009.

[103] J. A. Robinson, M. Labella, K. A. Trumbull, X. Weng, R. Cavelero, T. Daniels, Z. Hughes, M. Hollander, M. Fanton, D. Snyder, and et al., "Epitaxial graphene materials integration: Effects of dielectric overlayers on structural and electronic properties," *ACS Nano*, vol. 4, no. 5, 26672672, 2010.

[104] X. Wang, S. M. Tabakman, and H. Dai, "Atomic layer deposition of metal oxides on pristine and functionalized graphene," *Journal of the American Chemical Society*, vol. 130, no. 26, 81528153, 2008.

[105] B. Fallahazad, S. Kim, L. Colombo, and E. Tutuc, "Dielectric thickness dependence of carrier mobility in graphene with hfo2 top dielectric," *Applied Physics Letters*, vol. 97, no. 12, p. 123 105, 2010.

[106] M. J. Young, C. B. Musgrave, and S. M. George, "Growth and characterization of al2o3 atomic layer deposition films on sp2-graphitic carbon substrates using no2/trimethylaluminum pretreatment," *ACS Applied Materials and Interfaces*, vol. 7, no. 22, 1203012037, 2015.

[107] S. M. Prokes, M. B. Katz, and M. E. Twigg, "Growth of crystalline al2o3 via thermal atomic layer deposition: Nanomaterial phase stabilization," *APL Materials*, vol. 2, no. 3, p. 032 105, 2014.

[108] B. Dlubak, M.-B. Martin, C. Deranlot, K. Bouzehouane, S. Fusil, R. Mattana, F. Petroff, A. Anane, P. Seneor, A. Fert, and et al., "Homogeneous pinhole free 1 nm al2o3 tunnel barriers on graphene," *Applied Physics Letters*, vol. 101, no. 20, p. 203 104, 2012.

[109] B. Lee, S.-Y. Park, H.-C. Kim, K. Cho, E. M. Vogel, M. J. Kim, R. M. Wallace, and J. Kim, "Conformal al2o3 dielectric layer deposited by atomic layer deposition for graphene-based nanoelectronics," *Applied Physics Letters*, vol. 92, no. 20, p. 203 102, 2008.

[110] N. Leconte, J. Moser, P. Ordejn, H. Tao, A. Lherbier, A. Bachtold, F. Alsina, C. M. S. Torres, J.-C. Charlier, S. Roche, and et al., "Damaging graphene with ozone treatment: A chemically tunable metal-insulator transition," *ACS Nano*, vol. 4, no. 7, 40334038, 2010.

[111] T. L. Barr and S. Seal, "Nature of the use of adventitious carbon as a binding energy standard," *Journal of Vacuum Science & Technology A: Vacuum, Surfaces, and Films*, vol. 13, no. 3, pp. 1239–1246, 1995.

[112] R. F. Klie, N. D. Browning, A. R. Chowdhuri, and C. G. Takoudis, "Analysis of ultrathin sio2 interface layers in chemical vapor deposition of al2o3 on si by in situ scanning transmission electron microscopy," *Applied Physics Letters*, vol. 83, no. 6, 11871189, 2003.

[113] R. Katamreddy, R. Inman, G. Jursich, A. Soulet, A. Nicholls, and C. Takoudis, "Post deposition annealing of aluminum oxide deposited by atomic layer deposition using tris(diethylamino)aluminum and water vapor on si(100)," *Thin Solid Films*, vol. 515, no. 17, 69316937, 2007.

[114] V. K. Bityukov and V. A. Petrov, "Absorption coefficient of molten aluminum oxide in semitransparent spectral range," *Applied Physics Research*, vol. 5, no. 1, 2013.

[115] H. Shinotsuka, S. Tanuma, C. J. Powell, and D. R. Penn, "Calculations of electron inelastic mean free paths.," *Surface and Interface Analysis*, vol. 47, no. 12, 11321132, 1991.

[116] L. Fumagalli, D Natali, M. Sampietro, E Peron, F Perissinotti, G Tallarida, and S Ferrari, "Al2o3 as gate dielectric for organic transistors: Charge transport phenomena in poly-(3-hexylthiophene) based devices," *Organic Electronics*, vol. 9, no. 2, pp. 198–208, 2008.

[117] B. Dlubak, P. R. Kidambi, R. S. Weatherup, S. Hofmann, and J. Robertson, "Substrate-assisted nucleation of ultra-thin dielectric layers on graphene by atomic layer deposition," *Applied Physics Letters*, vol. 100, no. 17, p. 173 113, 2012.

[118] E. O. Filatova and A. S. Konashuk, "Interpretation of the changing the band gap of al2o3 depending on its crystalline form: Connection with different local symmetries," *The Journal of Physical Chemistry C*, vol. 119, no. 35, 2075520761, 2015.

[119] K. Zou, X. Hong, D. Keefer, and J. Zhu, "Deposition of high-qualityhfo2on graphene and the effect of remote oxide phonon scattering," *Physical Review Letters*, vol. 105, no. 12, 2010.

[120] M. Ruan, Y. Hu, Z. Guo, R. Dong, J. Palmer, J. Hankinson, C. Berger, and W. A. D. Heer, "Epitaxial graphene on silicon carbide: Introduction to structured graphene," *MRS Bulletin*, vol. 37, no. 12, 11381147, 2012.

VITA

Anna Miettinen was born in Philadelphia, PA, and raised in Rochester, NY. She has always been interested in the ability of science to bring people to a common understanding. She secured a Bachelor's degree in Physics from Colgate University (Hamilton, NY) where she studied computational neurophysics. Afterward, she continued directly to graduate school at the Georgia Institute of Technology to pursue research in experimental condensed matter physics. She plans to use her education to develop advancements in consumer and defense technologies.